The Pennsylvania State University

The Graduate School

Department of Electrical Engineering

THERMAL AND THERMOELECTRIC TRANSPORT STUDIES IN NANOMATERIALS USING MICROFABRICATED TESTBENCH

A Dissertation in

Electrical Engineering

by

DukSoo Kim

Submitted in Partial Fulfillment
of the Requirements
for the Degree of

Doctor of Philosophy

May 2015

The dissertation of DukSoo Kim was reviewed and approved* by the following:

Srinivas Tadigadapa
Professor of Electrical Engineering and Material Research Institute Affiliate
Dissertation Advisor
Chair of Committee

Jerzy Ruzyllo
Distinguished Professor of Electrical Engineering and Material Science and Engineering

Suman Datta
Professor of Electrical Engineering and Material Research Institute Affiliate

Gerald D. Mahan
Distinguished Professor of Physics

Kultegin Aydin
Professor of Electrical Engineering
Head of the Department of Electrical Engineering

*Signatures are on file in the Graduate School

ABSTRACT

This dissertation presents development of a microfabricated device (testbench) for measuring thermal conductivity and Seebeck coefficient of low-dimensional materials in addition to electrical conductivity and discusses the thermal and thermoelectric transport in nanoscale systems based on measurements performed using testbench. Despite the potential and obvious advantages of thermoelectric transduction, widespread use of such systems for energy harvesting and refrigeration remains limited to niche and specialized applications due to low efficiency. The thermoelectric efficiency is represented by a dimensionless figure of merit $ZT = \sigma S^2 T/\kappa$, where σ is electrical conductivity, S is Seebeck coefficient, κ is thermal conductivity, and T is absolute temperature. Low-dimensional structures are expected to have improved power factor (σS^2) and suppressed lattice thermal conductivity, and can therefore exhibit higher ZT than their bulk counterparts. Thus, there is a critical need for understanding thermal and thermoelectric transport in low-dimensional materials. However, in the case of low-dimensional materials, the accurate measurement of the thermal and thermoelectric properties is extremely challenging because of their small size. In order to address this need, we have developed a microfabricated testbench that can be used to measure two-probe electrical conductivity, thermal conductivity, and Seebeck coefficient of a variety of low-dimensional materials.

Using the testbench, the thermoelectric efficiency of bismuth telluride nanotubes has been investigated. The bismuth telluride is one of the most efficient thermoelectric materials. Although the efficiency of bismuth telluride nanowires and nanoplates was already reported by other groups, no enhancement in the ZT in these materials was observed. This has been primarily attributed to the unexpectedly small Seebeck coefficient caused by unintentional doping or surface band bending. Owing to small wall thickness (≤ 15nm) and nanocrystalline nature,

bismuth telluride nanotubes synthesized by solution-phase method showed ZT of 0.75 at T = 300 K which is 88 % larger than bulk bismuth telluride.

As a further application of the microfabricated testbench, studies on the effects of magnetic field on the thermoelectric transport in GaAs/MnAs core/shell nanowires and Co nanowires have been carried out in this work. The thermoelectric transport in magnetic nanoscale systems has been the subject of intense investigation since the recent observation of spin-Seebeck effect in ferromagnetic thin films. By measuring Seebeck coefficient and the electrical conductivity of ferromagnetic nanowires under the influence of magnetic field, it has been shown that the absolute value of Seebeck coefficient is increased by electron-magnon scattering whereas it is decreased by s-d scattering (scattering of spin-up 4s electrons into spin-down 3d states)

TABLE OF CONTENTS

LIST OF FIGURES

LIST OF TABLES

ACKNOWLEDGEMENTS

I would first like to thank my advisor, Dr. Srinivas Tadigadapa, for his constant support. This work would never be done without his help. I am also grateful to my dissertation committee members, Dr. Jerzy Ruzyllo, Dr. Suman Datta, and Dr. Gerald D. Mahan for their guidance.

I would like to acknowledge the help of the members of Dr. Tadigadapa's group. A partial list includes: Prasoon Joshi, Kiron Mateti, Matt Chang, Son Lai, Hwall Min, Pulkit Saksena, Sharat Parimi, Gokhan Hatipoglu, David Gaddes, ChenChen Zhang, Nishit Goel, Eugene Freeman.

I am thankful to Renzhong Du and Dr. Qi Li for their contribution to bismuth telluride project. I also want to mention the contribution of Jame Kally, Dr. Nitin Samarth, and Dr. Moses Chan to the project of the magnetic field related thermoelectric transport. Thanks go to Shih-Ying Yu and Dr. Suzanne E. Mohney for microscopic analysis of nanomaterials.

Chapter 1

Introduction

1.1 Thermoelectric Transport in Low-dimensional Materials

Approximately 50% of energy used in everyday life and industrial processes is lost as a waste heat. Though high temperature waste heat in large quantities is often reused by steam cycle, in case of low temperature waste heat, recovery is still challenging. Due to the capability to operate over a large range of temperature, thermoelectric transducers are an attractive solution for waste heat recovery application. A thermoelectric transducer is a solid-state-device that converts a temperature gradient into an electric potential and vice versa. Thermoelectric devices can also be used as an active cooling device. Because thermoelectric coolers can be constructed in small size and flexible shape, they are appropriate for small-scale cooling where mechanical refrigeration solutions are cumbersome and/or unsuitable. However, in spite of such potential advantages, application of thermoelectric devices has been limited to niche and specialized applications, such as converting car exhaust heat to electricity, radioisotope thermoelectric generator of satellite, and CPU cooling primarily due to the low efficiency of such systems. The thermoelectric efficiency is represented by a dimensionless figure of merit $ZT = \sigma S^2 T/\kappa$, where σ is the electrical conductivity, S is the Seebeck coefficient, κ is the thermal conductivity, and the T is the absolute temperature. The ZT needs to be greater than 3 in order for thermoelectric coolers to be competitive with commercial refrigerators. However, bismuth telluride and its alloys, which are the most efficient thermoelectric bulk materials known so far, still have ZT of ~1 near room temperature. This limit of bulk materials has driven recent researchers to focus on nanostructures, such as nanostructured bulk materials and low-dimensional materials (LDMs). The LDMs are

expected to have enhanced thermoelectric efficiency due to improved power factor (σS^2) and suppressed lattice thermal conductivity.

Although the power factor can be enhanced by altering the carrier concentration even in bulk materials, due to the opposing dependence of S and σ on carrier concentration, an optimal value for the carrier concentration exists beyond which no further improvement in the power factor can be typically achieved (Figure 1-1).

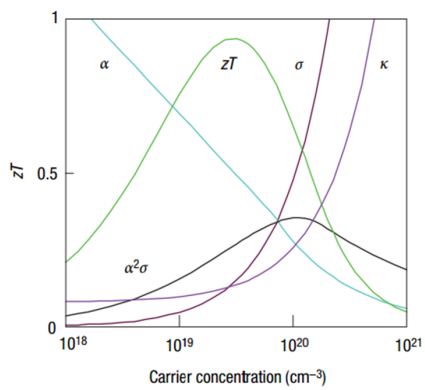

Figure 1-1. Variation of the transport coefficients as a function of carrier concentration. (α: Seebeck coefficient, σ: electrical conductivity, κ: thermal conductivity, $ZT = \sigma\alpha^2T/\kappa$). Copied from [1].

On the other hand, the LDMs have one more parameter to tailor the properties. It is the characteristic length of material which can be thickness of two-dimensional materials, such as thin films, or diameter of one-dimensional materials, such as nanowires. For materials in which the characteristic length is smaller than the wavelength of the charge carriers, the density of states (DOS) function can be changed to the shape that is beneficial to power factor [2, 3]. Furthermore, if the phonon mean free path is larger than the charge carrier mean free path, which is true for most semiconductors, LDMs could have a suppressed lattice thermal conductivity with less effect on electrical conductivity.

1.1.1 Seebeck Coefficient

The Seebeck effect arises from two main sources: diffusion of charge carriers and phonon-drag. When there is a temperature gradient in a material, the charge carriers at the hot side move toward the cold side by thermal diffusion until a dynamic equilibrium is established where the flux of carriers flowing towards the cold side is matched by a reverse flux driven by electric field generated within the material by carriers accumulated at cold side. The difference in the numbers of carriers between hot and cold sides results in electric potential. The carriers also move from hot to cold sides by momentum transfer from phonons to electrons. When a temperature gradient exists in a material, heat is conducted from hot to cold side by a lattice-wave which can be interpreted as a flux of phonons (quanta of lattice vibration). If there is no significant interaction between phonons and electrons, phonons are not important in terms of Seebeck effect. However, if there is a significant interaction, the phonons sweep or drag the electrons from the hot to the cold sides, which is known as the phonon-drag contribution to the thermoelectric effect. In the case of ferromagnetic materials, in addition to thermal diffusion of charge carriers and phonon-drag, there is an additional mechanism that can also move the carriers. Ferromagnetic materials have a spin-wave which is a propagating disturbance in magnetization. And, like the lattice-wave, it can also be interpreted as a flux of quasi-particles called magnons. In analogy with the case of the phonons, the flux of magnons from hot to cold sides drags carriers along with them. Therefore, the total Seebeck coefficient can be obtained by

$$S_T = S_e + S_{ph} + S_m \tag{1.1}$$

where S_e, S_{ph}, and S_m are Seebeck coefficient contributions from diffusion of charge carriers, phonon-drag, magnon-drag, respectively.

The equation proposed by Wilson, which is equivalent to the well-known Mott relation, is relatively simple and frequently used as a way to explain the reason why S_e of LDMs is

expected to be large compared to bulk. In the case where the Fermi level is considerably higher than conduction band edge such as a metal, the Seebeck coefficient is expressed as

$$S_e = \frac{\pi^2 k_B^2 T}{3e}\left(\frac{d\ln g(E)}{dE} + \frac{d\ln v^2(E)}{dE} + \frac{d\ln \tau(E)}{dE}\right)_{E \approx E_F} \tag{1.2}$$

where k_B is Boltzmann constant, T is absolute temperature, e is electric charge of an electron, $g(E)$ is DOS of electrons, v is average electron velocity, and τ is relaxation time for electrons. According to Equation (1.2), the Seebeck coefficient would be improved by increasing $d\ln g(E)/dE$. It is well known that low-dimensional systems exhibit sharp transitions in the DOS as a function of energy. Figure 1-2 qualitatively shows DOS of electrons in bulk (3D), quantum well (2D), quantum wire (1D), quantum dot (0D) systems. At these sharp transitions, the derivative $d\ln g(E)/dE$ can exhibit very large values which can result in significant enhancement of S_e.

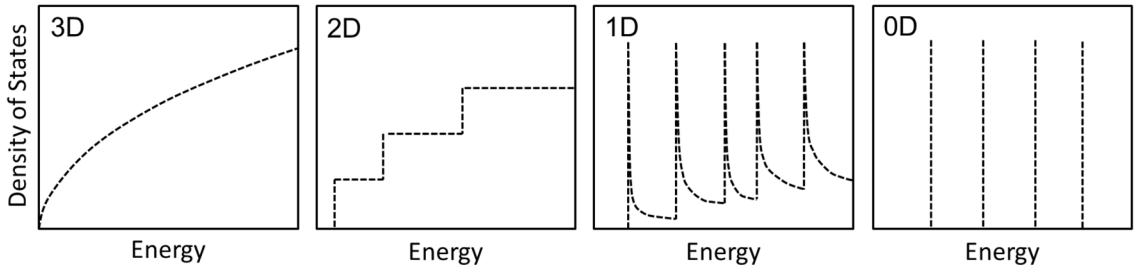

Figure 1-2. Schematic illustration of DOS as a function of energy for 3D, 2D, 1D, and 0D systems.

Although Equation (1.2) and Figure 1-2 show the possibility of enhanced Seebeck coefficient of LDMs in the case of a metal, they are not applicable for semiconductors which are better thermoelectric materials than metals. In order to quantitatively understand the effect of dimensionality on Seebeck coefficient in semiconductor, the Boltzmann equation based on relaxation time approximation is used [4]. Table 1-1 shows equations expressing electronic

dispersion of carriers, electrical conductivity, and S_e obtained using Boltzmann equation, in 3D, 2D, and 1D systems [2-4].

	Bulk (3D)	Quantum well (2D)	Quantum wire (1D)
$E(k)$	$\frac{\hbar^2 k_x^2}{2m_x}+\frac{\hbar^2 k_y^2}{2m_y}+\frac{\hbar^2 k_z^2}{2m_z}$	$\frac{\hbar^2 k_x^2}{2m_x}+\frac{\hbar^2 k_y^2}{2m_y}+\frac{\hbar^2 \pi^2 i^2}{2m_z a^2}$	$\frac{\hbar^2 k_x^2}{2m_x}+\frac{\hbar^2 \pi^2 i^2}{2m_y a^2}+\frac{\hbar^2 \pi^2 j^2}{2m_z a^2}$
σ	$\frac{1}{2\pi^2}\left(\frac{2k_B T}{\hbar^2}\right)^{3/2}(m_x m_y m_z)^{1/2} F_{1/2}\lvert e\rvert\mu_x$	$\frac{1}{2\pi a}\left(\frac{2k_B T}{\hbar^2}\right)(m_x m_y)^{1/2} F_0\lvert e\rvert\mu_x$	$\frac{1}{\pi a^2}\left(\frac{2k_B T}{\hbar^2}\right)^{1/2} m_x^{1/2} F_{-1/2}\lvert e\rvert\mu_x$
S_e	$\frac{k_B}{e}\left(\frac{(5/2+r)F_{3/2+r}}{(3/2+r)F_{1/2+r}}-\eta\right)$	$\frac{k_B}{e}\left(\frac{(2+r)F_{1+r}}{(1+r)F_r}-\eta\right)$	$\frac{k_B}{e}\left(\frac{(3/2+r)F_{1/2+r}}{(1/2+r)F_{-1/2+r}}-\eta\right)$

Table 1-1. Electronic dispersion of carriers, electrical conductivity, and S_e in 3D, 2D, and 1D systems. $\hbar$ is reduced Planck constant, k_x, k_y, and k_z are momentum space coordinates, m_x, m_y, and m_z are DOS effective mass, F is Fermi-Dirac integral, η is reduced Fermi level, i and j are the quantum numbers, a is the characteristic length of material, and r is the scattering parameter. Summarized from [2-4].

As an example, the DOS and power factor for n-type bismuth telluride were calculated based on the reported DOS effective mass and mobility of electrons (Figure 1-3) [2]. The power factor of 3 nm-diameter bismuth telluride quantum wire is theoretically enhanced by a factor of 3 compared to bulk value, as shown in Figure 1-3. Considering that most efficient bulk thermoelectric material have the ZT of ~1 near room temperature and the ZT should be larger than 3 for the thermoelectric device to be competitive with commercial refrigerator, 3-fold enhancement in power factor is large enough to motivate continued research and exploration of the thermal and thermoelectric transport properties of LDMs of nanometer dimensions.

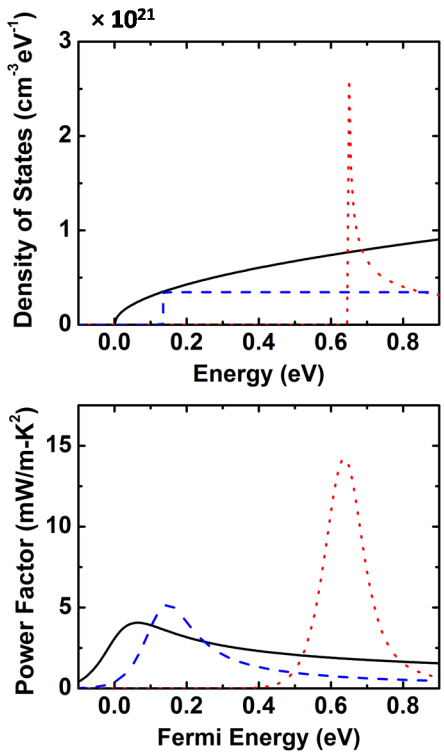

Figure 1-3. DOS as a function of carrier energy and power factor as a function of Fermi energy at T = 300 K for 3D (black solid line), 2D (blue dash line), and 1D (red dot line) systems. The calculation was performed assuming that the characteristic length and scattering parameter are 3 nm and 0, respectively.

The first proof-of-principle experiment that showed enhanced power factor was for lead telluride (PbTe) quantum well structure [5]. The 2D superlattice consisting of $PbTe/Pb_{0.927}Eu_{0.073}Te$ showed 3-4 times larger power factor than bulk when the width of quantum well is ~2 nm. The enhancement was also observed in the silicon (Si) quantum well superlattice consisting of Si/SiGe [6]. In case of 1D system, bismuth (Bi) nanowire was studied. Although Bi has high carrier mobility and large anisotropy of effective mass components that can be exploited to achieve large electrical conductivity, it shows small power factor compared to other Bi-related materials due to small S_e. Since it is a semimetal whose valence band edge is above conduction band edge, the electronic transport of Bi consists of both electron and hole and their contributions to S_e cancel each other out. However, Bi nanowire is theoretically expected to have a semimetal

to semiconductor electronic transition around the diameter of 50 nm [7]. As shown in upper plot of Figure 1-3, the conduction (valence) band edge moves upward (downward) in quantum regime because the confinement for the direction normal to the wire axis split energy bands into discrete subbands. Although the semimetal to semiconductor transition was experimentally proved [8, 9], the enhanced power factor has not yet been observed due to unoptimized carrier concentration or polycrystalline nature of nanowire [9].

S_{ph} can be quantitatively understood with reference to Peltier effect. The Peltier effect is heating or cooling created at the junction of two different materials when an electric current passes through it and the Peltier coefficient (Π) is defined as the ratio of heating or cooling rate to the electric current. S can be obtained from Π by using Kelvin relation $S = \Pi/T$. The relationship between Seebeck and Peltier coefficients is explained in Appendix B. If the electric field is applied, the carriers experience a total force $|e|nE$ per unit volume, where e is electric charge of carrier, n is carrier concentration, and E is electric field. The momentum can be passed on to impurities and other defects or to phonons. If the momentum is transferred to phonons, it will be retained in phonon until the phonon has non-momentum-conserving collisions. If it is supposed that x is the fraction of collisions that involve phonons and τ_{ph} is the momentum relaxation time of phonon, the excess momentum per unit volume carried by the phonons is given by $\Delta p = x\tau_{ph}|e|nE$. Because Π is the ratio of rate of energy flow to the electric current, it can be expressed as

$$\Pi_{ph} = \frac{\Delta w}{i} = \frac{v_{ph}^2 \Delta p}{ne\mu E} = \frac{|e|}{e}\frac{v_{ph}^2 x\tau_{ph}}{\mu} \tag{1.3}$$

where Δw is the rate of energy flowing through a cross section, i is the electric current density, v_{ph} is the phonon velocity, and μ is the carrier mobility. According to Equation (1.3), LDMs might show suppressed S_{ph} compared to bulk because increased scattering of phonons at the surface decreases τ_{ph}. However, the S_{ph} is negligibly small compared to S_e in degenerate semiconductor because momentum is increasingly transferred back to the carriers from phonons as the carrier

concentration increases [10]. As shown in Figure 1-3, the power factor shows a maximum when the Fermi level is near conduction or valence band edge. Therefore, suppressed S_{ph} would not be the obstacle for LDMs to have enhanced total S.

1.1.2 Thermal Conductivity

The thermal conductivity is composed of three parts: electronic thermal conductivity, bipolar thermal conductivity, and lattice thermal conductivity. The electronic conductivity (κ_e) is described by the heat flow by charge carriers. Therefore, it is strongly coupled to electrical conductivity. Drude predicted a theoretical value (Lorentz number) of $\kappa_e/\sigma T$ is constant, which is also known as the Wiedmann-Franz law. The bipolar thermal conductivity (κ_b) should be considered in case of semiconductor. When both holes and electrons are present, it is possible for them to flow in the same direction. It results in heat transfer without electric current. It is given by

$$\kappa_b = \frac{\sigma_n \sigma_p}{\sigma_n + \sigma_p}\left(S_n - S_p\right)^2 T \tag{1.4}$$

where σ_n (σ_p) and S_n (S_p) are electron (hole) contribution to electrical conductivity and Seebeck coefficient, respectively. It could be large in narrow band gap materials or at the high temperatures due to considerable number of minority carriers excited by thermal energy.

The lattice thermal conductivity (κ_{ph}) is determined by the heat transferred by phonons. Atoms vibrating more energetically will transfer their energy to neighboring atoms vibrating less energetically. This is the way for most non-metallic solids to transfer heat. According to the kinetic transport theory, the lattice thermal conductivity is given by

$$\kappa_{ph} = \frac{1}{3} C_{ph} v_{ph} l_{ph} \tag{1.5}$$

where C_{ph}, v_{ph}, and l_{ph} denote the specific heat per unit volume, phonon velocity, and phonon mean free path, respectively. Because increased scattering of phonon at the surface leads to

smaller l_{ph}, LDMs have reduced lattice thermal conductivity than bulk. Thermal conductivity of silicon (Si) nanowires with different diameters was experimentally reported in 2003 [11]. It is significantly lower than that of the bulk Si and, as the diameter is decreased, the thermal conductivity is correspondingly reduced.

Over the past four decades, the Callaway's and Holland's models have proven successful in modeling lattice thermal conductivity, especially for temperature dependence. However, it was found that these models are not applicable to LDMs because these models are based on the phonon dispersion approximated by Debye model instead of complete phonon dispersion [12]. More recently, researchers have attempted to predict the lattice thermal conductivity of LDMs using complete phonon dispersion [12, 13]. The Landauer approach is one of the methods using complete phonon dispersion. According to Landauer approach, κ_{ph} is calculated by [13, 14]

$$\kappa_{ph} = \frac{\pi^2 {k_B}^2 T}{3h} \langle M_{ph} \rangle \langle \langle \lambda_{ph} \rangle \rangle \tag{1.6}$$

where h is Planck's constant, $<M_{ph}>$ is the number of phonon modes that participate in transport, and $<<\lambda_{ph}>>$ is average phonon mean free path for backscattering. The $<M_{ph}>$ and $<<\lambda_{ph}>>$ are obtained from the complete phonon dispersion that can be calculated using the interatomic pair potential model or DFT. The detail on Landauer approach will be explained when analyzing the thermal conductivity of bismuth telluride nanotubes in Chapter 3. Another model proposed by Mingo el al. [12] also make a good agreement with experimental data of silicon nanowires. However, in principle, both models take the same approach except for minor differences in details.

1.2 Measurement Techniques

While understanding and detailed study of the thermoelectric properties of LDMs is becoming important due to possibility of enhanced efficiency, the small size of LDMs and the

lack of an equivalent of an “ammeter” for heat flow make the measurement of thermal conductivity and Seebeck coefficient of LDMs challenging. This section reviews the techniques that have been used to measure thermal conductivity and/or Seebeck coefficient of LDMs.

In order to obtain the Seebeck coefficient, a temperature difference should be created and measured between two points that are apart from each other in the material. At the same time, the thermoelectric voltage induced by temperature difference should be measured. In case of bulk materials, it is relatively easy. Each end of the material is thermally connected to heat source and heat sink and the thermocouple wires are attached electrically and thermally to two different points of the material. The temperature difference then is measured using the thermocouple wires and the induced thermoelectric voltage is measured through one leg of each thermocouple wire. In some cases, this method is also applicable to low-dimensional materials: thin film grown on large area [15-17] and nanowire array formed by nanoporous template [18-20]. However, the application of this method is limited to a certain type of LDMs. It cannot be used for micron-sized thin films (nanoribbons, nanoplates, and nanoflakes) or nanowires synthesized without template. Additionally, the measurement of nanowire array prevents detailed studies on size effect, surface roughness, and defects because they are averaged out. The micro/nano-fabrication is necessary for measuring the Seebeck coefficient of individual micron-sized LDMs. The general description on fabrication and measurement is as follows. The LDMs are dispersed on the electrically insulating surface, such as silicon dioxide. Thereafter, electrodes are patterned on the two ends of the LDM using e-beam lithography and lift-off process. These electrodes serve two purposes: probing temperature of the end of LDM and sensing electric or thermoelectric voltage. A heater structure is also patterned near the one end of LDM. A temperature gradient is created along the LDM by applying current or voltage to heater and the temperature of both ends of LDM is obtained by measuring the change of the resistance of electrodes. At the same time, the induced thermoelectric voltage could be obtained by measuring the voltage between two electrodes. This

method has been used for various LDMs [21-25] because it does not include the process of aligning or manipulating the LDM which is the most difficult part in measuring transport properties of LDMs. However, thermal conductivity cannot be obtained using this method since the substrate thermal conductivity which is orders of magnitude larger than the thermal conductivity of the nanotube completely overwhelms the measurement of heat flow through the LDM.

Methods for measuring thermal conductivity can be classified into two types: steady-state method and transient method. The typical steady-state technique uses similar set-up with measurement of Seebeck coefficient. One end of material makes good thermal contact with the heat sink and a small heater is attached to the other end. Electrical power dissipated in the heater provides the heat flow through the material. Two thermocouple wires separated by some distance are used to measure the temperature difference. However, as opposed to the measurement of Seebeck coefficient, it cannot be applicable even for thin films growth on large area and nanowire array formed by template because of the heat flow though substrate or template. Raman spectroscopy has recently been used for measuring thermal conductivity of suspended graphene [26, 27]. The center of the graphene is exposed to a laser beam, which heats the graphene. At the same time, the temperature of illuminated region is monitored by Raman frequency shift which is proportional to the temperature. However, it cannot be applicable for submicron-sized LDMs, such as nanowires and nanotubes, due to the large spot size of laser. The transient technique uses time-varying heat source and monitors the temperature as a function of time. And the thermal conductivity is obtained through mathematical analysis. There are two transient techniques that can be used for thin films: Time-domain thermoreflectance [28-30] and 3ω method [31-33]. However, the Time-domain thermoreflectance cannot be applicable to submicron-sized LDMs because a laser is used for heating and sensing temperature. 3ω method also cannot be used for submicron-sized LDMs because a thin metal wire should be patterned on the test-material.

Recently, the 3ω method was modified by Lu et al. in order to use it to nanowire or nanotube measurement [34]. It requires a four-probe configuration and the test-material should be suspended between two inner voltage-sensing probes so that probe is the only heat sink for the Joule heat produced in the test-material. The 3ω method uses the test-material itself as both a heater and a thermistor. A sinusoidal current with frequency ω causes 2ω fluctuation in resistance of the test-material as a consequence of the Joule heating which occurs at a frequency of 2ω. The 3ω voltage arising from the sinusoidal current at ω and fluctuating resistance is related to thermal conductivity of test-material. At frequencies below thermal cut-off, the thermal conductivity is given by [34]

$$\kappa = \frac{\sqrt{2} {I_{peak}}^3 R R' L}{\pi^4 V_{3\omega} A} \tag{1.7}$$

where I_{peak} is the peak value of applied sinusoidal current, R and R' are the resistance of test-material between voltage-sensing probes and its derivative with respect to temperature, L is the length of the test-material between voltage-sensing probes, A is the cross-sectional area of the test-material, and $V_{3\omega}$ is 3ω voltage. Although it was successfully used for several LDMs [35-37], there are some drawbacks in 3ω method. It can be used only when the test-material is electrically conducting. And the drive current needs to be large enough to heat the test-material. It increases the risk that the test-material blows up due to the Joule heat produced by the contact resistance between the test-material and probes.

Because LDMs usually has a variation in characteristic length and surface roughness even when they are synthesized in one batch, it is necessary to measure electrical conductivity, thermal conductivity, and Seebeck coefficient together of one specific LDM for better understanding the thermoelectric efficiency of LDMs. In order to address this need, the microfabricated suspended device was developed by Kim et al. [38]. The device consists of two adjacent silicon nitride membranes suspended with long and narrow silicon nitride beams. The

suspended structure allows for a larger temperature gradient across the LDM and uniform temperature distribution on membrane. Each membrane has a platinum meander structure which serves as both heater and thermistor. And another platinum electrode is designed on each membrane to provide electrical connection to the LDM. The main advantage of this method is that the thermal conductivity can be measured even when there is no electrical connection between LDM and device, i.e. of electrically insulating LDMs. However, insulating LDMs are not of interest as thermoelectrics. Independently of thermoelectrics, thermal transport itself is receiving attention because new physics and novel thermal properties arise in LDMs. Although this method has been successfully used for obtaining the *ZT* of many LDMs, such as nanoplates [39] and nanowires [40-42], it has one major drawback. The LDM needs to be positioned between the two suspended membranes. Considering that there is only one test-site on the device, the chances of landing the LDM precisely between the suspended membranes by random drop-casting method is typically very small. Therefore, considerable amount of additional work is required to place the LDM at the right location, including manipulation of the LDMs using AFM probe tips, dielectrophoresis etc. which is tedious and cannot be used for fragile material.

The Seebeck coefficient and/or thermal conductivity measurement techniques for LDMs are summarized in Table1-2.

Transport property	Technique	Material type	Remarks
S	Bulk method	Thin film, nanowire array	-
	Micro/nano-fabrication	Any type	-
κ	Raman spectroscopy	Thin film	Spatial resolution: 1-10 μm
	Time-domain thermoreflectance	Thin film	Spatial resolution: 1-10 μm
	Typical 3ω method	Thin film	Spatial resolution is limited by the dimension of a long metallic wire deposited above the material.
	Modified 3ω method	Any type	Not applicable to electrically insulating materials.
S and κ	Microfabricated suspended device	Any type	Additional work for placing the material on the test-site.

Table 1-2. Techniques for measuring Seebeck coefficient and/or thermal conductivity of LDMs. (S: Seebeck coefficient, κ: thermal conductivity)

1.3 Motivation and Scope of This Work

The motivation of this work is to develop a universal, high yield, microfabricated testbench for the measurement of the electrical conductivity, thermal conductivity, and Seebeck coefficient of LDMs. The design of the testbench has been specifically optimized to facilitate the easy placement of 1D nanowires, nanotubes and 2D nanoflakes specifically for the study of their thermal and thermoelectric transport properties. Although microfabricated devices capable of such measurements have been reported earlier, these require considerable effort in terms of placement and alignment of the LDMs on the device because of the availability of single test-site on the device. We have developed microfabricated device (testbench) with high surface density of test-sites in the central area of the device to enhance the probability of landing a single LDM at the desired position without any physical manipulation when drop-casting LDMs from a solution. In Chapter 2, the design of testbench, the fabrication process, and its thermal and electrical

characteristics are presented. Details on measurement set-up and procedure are also explained in Chapter 2.

Although LDMs are expected to show better thermoelectric efficiency than bulk due to the suppressed lattice thermal conductivity and the enhanced power factor, in case of bismuth telluride which is one of the best thermoelectric material, there has been no experimental report showing *ZT* of LDMs is comparable to or larger than that of its bulk values primarily due to the unexpectedly small Seebeck coefficient. In this work, we have investigated and reported on the complete electrical and thermal transport properties of bismuth telluride nanotubes for the first time. Using the testbench and 3ω method, the thermoelectric efficiency of bismuth telluride nanotubes synthesized by solution-phase method has been obtained. Chapter 3 explains how the nanocrystalline nature and narrow wall (≤ 15nm) of bismuth telluride nanotubes result in enhanced thermoelectric efficiency.

The resistance of ferromagnetic LDMs under magnetic field has been the subject of intense study for the past twenty years because the electronic transport in nanoscale magnetic systems shows unique properties that are not observed in bulk and has the potential to be used for a wide range of applications. Furthermore, recently thermoelectric transport under magnetic field has gained attention after observation of spin-Seebeck effect, which describes spin current or spin accumulation due to thermal gradient, in ferromagnetic thin films. In the Chapter 4, we present the effects of magnetic field on the electronic and thermoelectric transport in GaAs/MnAs core/shell and Co nanowires based on the measurement performed using the testbench.

Reference

[1] G. J. Snyder and E. S. Toberer, "Complex thermoelectric materials," *Nature materials,* vol. 7, pp. 105-114, 2008.

[2] L. Hicks and M. Dresselhaus, "Effect of quantum-well structures on the thermoelectric figure of merit," *Physical Review B,* vol. 47, p. 12727, 1993.

[3] L. Hicks and M. Dresselhaus, "Thermoelectric figure of merit of a one-dimensional conductor," *Physical Review B,* vol. 47, p. 16631, 1993.

[4] E. Rittner, "On the theory of the Peltier heat pump," *Journal of Applied Physics,* vol. 30, pp. 702-707, 1959.

[5] L. Hicks, T. Harman, X. Sun, and M. Dresselhaus, "Experimental study of the effect of quantum-well structures on the thermoelectric figure of merit," *Physical Review B,* vol. 53, p. R10493, 1996.

[6] T. Koga, S. Cronin, M. Dresselhaus, J. Liu, and K. Wang, "Experimental proof-of-principle investigation of enhanced Z 3D T in (001) oriented Si/Ge superlattices," *Applied Physics Letters,* vol. 77, pp. 1490-1492, 2000.

[7] Y.-M. Lin, X. Sun, and M. Dresselhaus, "Theoretical investigation of thermoelectric transport properties of cylindrical Bi nanowires," *Physical Review B,* vol. 62, p. 4610, 2000.

[8] J. Heremans, C. M. Thrush, Y.-M. Lin, S. Cronin, Z. Zhang, M. Dresselhaus, and J. Mansfield, "Bismuth nanowire arrays: Synthesis and galvanomagnetic properties," *Physical Review B,* vol. 61, p. 2921, 2000.

[9] A. Boukai, K. Xu, and J. R. Heath, "Size-dependent transport and thermoelectric properties of individual polycrystalline bismuth nanowires," *Advanced Materials,* vol. 18, pp. 864-869, 2006.

[10] C. Herring, "Theory of the thermoelectric power of semiconductors," *Physical Review,* vol. 96, p. 1163, 1954.

[11] D. Li, Y. Wu, P. Kim, L. Shi, P. Yang, and A. Majumdar, "Thermal conductivity of individual silicon nanowires," *Applied Physics Letters,* vol. 83, pp. 2934-2936, 2003.

[12] N. Mingo, L. Yang, D. Li, and A. Majumdar, "Predicting the thermal conductivity of Si and Ge nanowires," *Nano letters,* vol. 3, pp. 1713-1716, 2003.

[13] C. Jeong, S. Datta, and M. Lundstrom, "Thermal conductivity of bulk and thin-film silicon: A Landauer approach," *Journal of Applied Physics,* vol. 111, p. 093708, 2012.

[14] C. Jeong, S. Datta, and M. Lundstrom, "Full dispersion versus Debye model evaluation of lattice thermal conductivity with a Landauer approach," *Journal of Applied Physics,* vol. 109, p. 073718, 2011.

[15] S. Cho, A. DiVenere, G. Wong, J. Ketterson, J. Meyer, and C. Hoffman, "Thermoelectric power of MBE grown Bi thin films and Bi/CdTe superlattices on CdTe substrates," *Solid state communications,* vol. 102, pp. 673-676, 1997.

[16] M. Ambia, M. Islam, and M. O. Hakim, "Studies on the seebeck effect in semiconducting ZnO thin films," *Journal of materials science,* vol. 27, pp. 5169-5173, 1992.

[17] M. Muhibbullah, M. Hakim, and M. Choudhury, "Studies on Seebeck effect in spray deposited CuO thin film on glass substrate," *Thin Solid Films,* vol. 423, pp. 103-107, 2003.

[18] S. Cronin, Y. Lin, T. Koga, X. Sun, J. Ying, and M. Dresselhaus, "Thermoelectric investigation of bismuth nanowires," in *Thermoelectrics, 1999. Eighteenth International Conference on*, 1999, pp. 554-557.

[19] A. R. Abramson, W. C. Kim, S. T. Huxtable, H. Yan, Y. Wu, A. Majumdar, C.-L. Tien, and P. Yang, "Fabrication and characterization of a nanowire/polymer-based nanocomposite for a prototype thermoelectric device," *Microelectromechanical Systems, Journal of,* vol. 13, pp. 505-513, 2004.

[20] J. Keyani, A. M. Stacy, and J. Sharp, "Assembly and measurement of a hybrid nanowire-bulk thermoelectric device," *Applied Physics Letters,* vol. 89, p. 233106, 2006.

[21] J. P. Small, K. M. Perez, and P. Kim, "Modulation of thermoelectric power of individual carbon nanotubes," *Physical review letters,* vol. 91, p. 256801, 2003.

[22] J. H. Seol, A. L. Moore, S. K. Saha, F. Zhou, L. Shi, Q. L. Ye, R. Scheffler, N. Mingo, and T. Yamada, "Measurement and analysis of thermopower and electrical conductivity of an indium antimonide nanowire from a vapor-liquid-solid method," *Journal of Applied Physics,* vol. 101, p. 023706, 2007.

[23] W. Liang, A. I. Hochbaum, M. Fardy, O. Rabin, M. Zhang, and P. Yang, "Field-effect modulation of Seebeck coefficient in single PbSe nanowires," *Nano letters,* vol. 9, pp. 1689-1693, 2009.

[24] S. H. Lee, W. Shim, S. Y. Jang, J. W. Roh, P. Kim, J. Park, and W. Lee, "Thermoelectric properties of individual single-crystalline PbTe nanowires grown by a vapor transport method," *Nanotechnology,* vol. 22, p. 295707, 2011.

[25] B. Hamdou, J. Kimling, A. Dorn, E. Pippel, R. Rostek, P. Woias, and K. Nielsch, "Thermoelectric Characterization of Bismuth Telluride Nanowires, Synthesized Via Catalytic Growth and Post-Annealing," *Advanced Materials,* vol. 25, pp. 239-244, 2013.

[26] A. A. Balandin, S. Ghosh, W. Bao, I. Calizo, D. Teweldebrhan, F. Miao, and C. N. Lau, "Superior thermal conductivity of single-layer graphene," *Nano letters,* vol. 8, pp. 902-907, 2008.

[27] J.-U. Lee, D. Yoon, H. Kim, S. W. Lee, and H. Cheong, "Thermal conductivity of suspended pristine graphene measured by Raman spectroscopy," *Physical Review B,* vol. 83, p. 081419, 2011.

[28] O. Käding, H. Skurk, and K. Goodson, "Thermal conduction in metallized silicon-dioxide layers on silicon," *Applied Physics Letters,* vol. 65, pp. 1629-1631, 1994.

[29] W. Capinski, H. Maris, T. Ruf, M. Cardona, K. Ploog, and D. Katzer, "Thermal-conductivity measurements of GaAs/AlAs superlattices using a picosecond optical pump-and-probe technique," *Physical Review B,* vol. 59, p. 8105, 1999.

[30] S. Huxtable, D. G. Cahill, V. Fauconnier, J. O. White, and J.-C. Zhao, "Thermal conductivity imaging at micrometre-scale resolution for combinatorial studies of materials," *Nature materials,* vol. 3, pp. 298-301, 2004.

[31] D. G. Cahill, "Thermal conductivity measurement from 30 to 750 K: the 3ω method," *Review of Scientific Instruments,* vol. 61, pp. 802-808, 1990.

[32] T. Borca-Tasciuc, A. Kumar, and G. Chen, "Data reduction in 3ω method for thin-film thermal conductivity determination," *Review of Scientific Instruments,* vol. 72, pp. 2139-2147, 2001.

[33] T. Yamane, N. Nagai, S.-i. Katayama, and M. Todoki, "Measurement of thermal conductivity of silicon dioxide thin films using a 3ω method," *Journal of Applied Physics,* vol. 91, pp. 9772-9776, 2002.

[34] L. Lu, W. Yi, and D. Zhang, "3ω method for specific heat and thermal conductivity measurements," *Review of Scientific Instruments,* vol. 72, pp. 2996-3003, 2001.

[35] M. Ou, T. Yang, S. Harutyunyan, Y. Chen, C. Chen, and S. Lai, "Electrical and thermal transport in single nickel nanowire," *Applied Physics Letters,* vol. 92, pp. 063101-063101-3, 2008.

[36] K. Lee, T. Choi, S. Lee, and D. Poulikakos, "Focused ion beam-assisted manipulation of single and double β-SiC nanowires and their thermal conductivity measurements by the four-point-probe 3-ω method," *Nanotechnology,* vol. 21, p. 125301, 2010.

[37] S. Dhara, H. S. Solanki, V. Singh, S. Sengupta, B. Chalke, A. Dhar, M. Gokhale, A. Bhattacharya, and M. M. Deshmukh, "Tunable thermal conductivity in defect engineered nanowires at low temperatures," *Physical Review B,* vol. 84, p. 121307, 2011.

[38] P. Kim, L. Shi, A. Majumdar, and P. McEuen, "Thermal transport measurements of individual multiwalled nanotubes," *Physical review letters,* vol. 87, p. 215502, 2001.

[39] M. T. Pettes, J. Maassen, I. Jo, M. S. Lundstrom, and L. Shi, "Effects of surface band bending and scattering on thermoelectric transport in suspended bismuth telluride nanoplates," *Nano letters,* vol. 13, pp. 5316-5322, 2013.

[40] J. Zhou, C. Jin, J. H. Seol, X. Li, and L. Shi, "Thermoelectric properties of individual electrodeposited bismuth telluride nanowires," *Applied Physics Letters,* vol. 87, pp. 133109-133109-3, 2005.

[41] F. Zhou, J. Szczech, M. T. Pettes, A. L. Moore, S. Jin, and L. Shi, "Determination of transport properties in chromium disilicide nanowires via combined thermoelectric and structural characterizations," *Nano letters,* vol. 7, pp. 1649-1654, 2007.

[42] A. I. Hochbaum, R. Chen, R. D. Delgado, W. Liang, E. C. Garnett, M. Najarian, A. Majumdar, and P. Yang, "Enhanced thermoelectric performance of rough silicon nanowires," *Nature,* vol. 451, pp. 163-167, 2008.

Appendix A

Derivation of Seebeck Coefficient Formulae

The electric current density, which is defined to be the rate at which charges flow across unit cross-sectional area, is obtained by

$$J = e\int_0^\infty v(E)(f(E) - f_0(E))g(E)dE \tag{A.1}$$

where e is electric charge of carrier, v is the velocity of carriers, f is the distribution function of carriers, f_0 is Fermi distribution function, and g is the density of states of carriers. $(f - f_0)$ describes the distribution of carriers involved in transport because there is no flow of carriers when $f = f_0$. According to the Boltzmann equation based on relaxation time approximation, we can obtain the relationship between the distribution function and disturbance (electric field or temperature gradient).

$$\frac{f(E) - f_0(E)}{\tau(E)} = v(E)\frac{df_0(E)}{dE}\left(\frac{dE_F}{dx} + \frac{E - E_F}{T}\frac{dT}{dx}\right) \tag{A.2}$$

where τ, E_F, and T denote the relaxation time of carriers, the Fermi energy, and absolute temperature, respectively. The term in the bracket represents energy gradient. The first term is the gradient of the electric potential energy and the second term is that of thermal energy. By substituting $(f - f_0)$ using Equation (A.2), Equation (A.1) can be rewritten as

$$J = e\int_0^\infty v^2(E)\tau(E)g(E)\frac{df_0(E)}{dE}\left(\frac{dE_F}{dx} + \frac{E - E_F}{T}\frac{dT}{dx}\right)dE \tag{A.3}$$

The Seebeck coefficient is equivalent to the ratio of electric field to temperature gradient when the electric current density is zero. Therefore, it is given by

$$S = \frac{-\frac{dE_F}{dx}}{\frac{dT}{dx}}\frac{1}{e} = \frac{1}{eT}\left\{\frac{\int_0^\infty v^2(E)\tau(E)g(E)(E-E_F)\left(-\frac{df_0(E)}{dE}\right)dE}{\int_0^\infty v^2(E)\tau(E)g(E)\left(-\frac{df_0(E)}{dE}\right)dE}\right\} \tag{A.4}$$

The relaxation time τ is assumed to depend on E according to $\tau_0 E^r$, where τ_0 is a constant and r is the scattering parameter which is approximated depending on the scattering mechanism of carriers: −1/2 for scattering on acoustic phonons, 0 for scattering on neutral impurities, 3/2 for scattering on ionized impurities. It is well known that the density of states g has power-law dependence on E and the exponent depends on the dimensionality of material: 1/2 for 3D, 0 for 2D, -1/2 for 1D. And the v^2 is proportional to E. Hence, Equation (A.4) becomes

$$S = \frac{-\frac{dE_F}{dx}}{\frac{dT}{dx}}\frac{1}{e} = \frac{k_B}{e}\left\{\frac{\int_0^\infty E^{2+d+r}\left(-\frac{df_0(E)}{dE}\right)dE}{\int_0^\infty E^{1+d+r}\left(-\frac{df_0(E)}{dE}\right)dE} - \frac{E_F}{k_B T}\right\} \tag{A.5}$$

$$= \frac{k_B}{e}\left\{\frac{(2+d+r)F_{1+d+r}(\eta_F)}{(1+d+r)F_{d+r}(\eta_F)} - \eta_F\right\}$$

where k_B and η_F denote Boltzmann constant and the reduced Fermi energy (E_F/k_BT), respectively. And the Fermi-Dirac integral F_n is given by

$$F_n(\eta_F) = \int_0^\infty \frac{\eta^n d\eta}{e^{\eta-\eta_F}+1} \tag{A.6}$$

Further calculation leads us to Mott relation. The electrical conductivity can be given by the ratio of the electric current density to the electric field when temperature gradient is zero.

$$\sigma = \frac{eJ}{-\frac{dE_F}{dx}} = \int_0^\infty e^2 v^2(E)\tau(E)g(E)\left(-\frac{df_0(E)}{dE}\right)dE \tag{A.7}$$

$$= \int_0^\infty \sigma(E)\left(-\frac{df_0(E)}{dE}\right)dE$$

where $\sigma(E)$ is conductivity-like function which is a conductivity that a metal would show if its Fermi energy is equal to E. And using Equation (A.7), Equation (A.4) is rearranged to

$$S = \frac{k_B}{e}\frac{1}{\sigma}\left\{\int_0^\infty \sigma(E)\frac{E-E_F}{k_BT}\left(-\frac{df_0(E)}{dE}\right)dE\right\} \tag{A.8}$$

In case of metal, df_0/dE is smoothed delta function peaked at $E = E_F$. It allows us to use first two term of Taylor series expansion at $E = E_F$ for $\sigma(E)$. After some rearrangements, Equations (A.7) and (A.8) then becomes

$$\sigma = \sigma(E_F)\int_0^\infty \left(-\frac{df_0(E)}{dE}\right)dE + k_BT\,\sigma'(E_F)\int_0^\infty \frac{E-E_F}{k_BT}\left(-\frac{df_0(E)}{dE}\right)dE \tag{A.9}$$

$$\sigma S = \frac{k_B}{e}\left\{\sigma(E_F)\int_0^\infty \frac{E-E_F}{k_BT}\left(-\frac{df_0(E)}{dE}\right)dE \right. \tag{A.10}$$

$$\left. + k_BT\sigma'(E_F)\int_0^\infty \left(\frac{E-E_F}{k_BT}\right)^2\left(-\frac{df_0(E)}{dE}\right)dE\right\}$$

E_F is typically of the order of 5 electron volts which corresponds to $T_F = 50000$ K. Considering $E_F >> k_BT$, the integral part can be modified as

$$\int_0^\infty \left(\frac{E-E_F}{k_BT}\right)^n\left(-\frac{df_0(E)}{dE}\right)dE = \int_{-\infty}^\infty x^n\frac{e^x}{(e^x+1)^2}dx \tag{A.11}$$

It is equal to 1, 0, and $\pi^2/3$ for the case of n = 0, 1, and 2, respectively. Hence, Equations (A.9) and (A.10) can be rewritten to

$$\sigma = \sigma(E_F) \tag{A.12}$$

$$S = -\frac{\pi^2k_B^2T}{3e}\frac{\sigma'(E_F)}{\sigma(E_F)} \tag{A.13}$$

$$= -\frac{\pi^2k_B^2T}{3e}\frac{d\ln\sigma(E)}{dE}\bigg|_{E\approx E_F}$$

Equation (A.13) is well-known Mott relation.

Appendix B

Derivation of Kelvin Relation

The Peltier effect is heating or cooling created at the junction of two different materials by feeding a current. And the Peltier coefficient (Π) is defined as the ratio of heating or cooling rate to the electric current. And it is regarded as positive if the junction at which the current leaves the material is heated and the junction at which it enters is cooled. In the first place, it was not realized that Peltier and Seebeck effect is related to each other. In 1855, W. Thomson established the relationship between two effects using the theory of thermodynamics and also showed that there is a third thermoelectric effect, Thomson effect. The Thomson effect is heating or cooling created when both temperature gradient and electric current exist in the material. And the Thomson coefficient (μ) is defined as the ratio of heating or cooling rate to the applied current and the temperature gradient. And it is positive if heat is absorbed when the current and the temperature gradient is on the same direction.

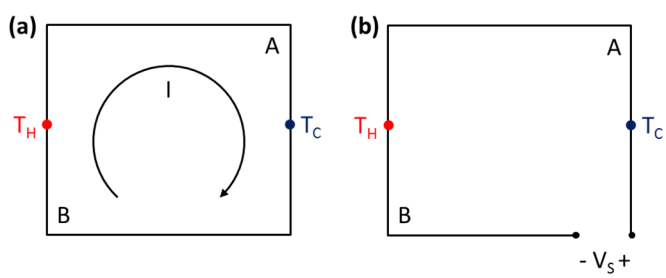

Figure B-1. Simple thermoelectric circuits. (a) Closed circuit. (b) Open circuit.

Consider two dissimilar materials connected to each other with two junctions as shown in Figure B-1(a). If the two junctions are maintained at different temperatures, the electric current will flow in the circuit. Then, the junctions will be heated or cooled by the Peltier effect and the

material will be heated or cooled by the Thomson effect. And the change in entropy should be zero because it is reversible process. Hence, one can obtain

$$\left[\frac{\Pi_{BA}(T_H)}{T_H}+\frac{\Pi_{AB}(T_C)}{T_C}+\int_{T_C}^{T_H}\frac{\mu_A(T)}{T}dT+\int_{T_H}^{T_C}\frac{\mu_B(T)}{T}dT\right]\times I=0 \tag{B.1}$$

where Π_{AB} and Π_{BA} are $\Pi_A-\Pi_B$ and $\Pi_B-\Pi_A$, respectively. And if the T_H-T_C is small enough, it can be modified to

$$\frac{d(\frac{\Pi_{AB}(T)}{T})}{dT}-\frac{\mu_{AB}(T)}{T}=0 \tag{B.2}$$

where μ_{AB} is $\mu_A-\mu_B$. And it can be rearranged to

$$\frac{d\Pi_{AB}(T)}{dT}-\frac{\Pi_{AB}(T)}{T}=\mu_{AB}(T) \tag{B.3}$$

If it is supposed that there is the Seebeck coefficient measurement circuit shown as Figure B-1(b), total energy should be conserved within the entire circuit for the closed loop. The Seebeck effect maintains a driving force which causes a current feeding through the circuit. And it induces the Peltier and Thomson effects. Because the rate of electric energy should be equivalent to the heating rate caused by Peltier and Thomson effects, one can obtain

$$\mathrm{I}\int_{T_C}^{T_H}S_{AB}(T)dT=I\left[\Pi_{AB}(T_H)+\Pi_{BA}(T_C)-\int_{T_C}^{T_H}\mu_{AB}(T)dT\right] \tag{B.4}$$

where S_{AB} is S_A-S_B. And in case that T_H-T_C is small enough, it can be modified to

$$S_{AB}(T)=\frac{d\Pi_{AB}(T)}{dT}-\mu_{AB}(T) \tag{B.5}$$

Using Equations (B.3) and (B.5), we can obtain Kelvin relation defined by

$$\Pi_{AB}(T)=S_{AB}(T)T \tag{B.6}$$

$$\mu_{AB}(T)=\frac{dS_{AB}(T)}{dT}T \tag{B.7}$$

Chapter 2

Microfabricated Thermoelectric Testbench

2.1 Introduction

As discussed in the previous chapter, measurement of the thermoelectric and thermal properties of low-dimensional materials such as nanowires, nanotubes, nanoribbons, and nanoflakes are challenging. There are two approaches for the accomplishment of these measurements in nanoscale materials: (i) Through a top-down multilayer thin film integration of the material under test followed by lithographic patterning into nanoscale structures and integration onto specifically designed measurement test structures [1, 2], and (ii) Integration of bottom-up synthesized low-dimensional materials onto a specifically designed thermal testbench [3-6]. In this work, we are primarily focusing on the second approach with the goal of realizing a microfabricated device (testbench) that can easily measure the thermal and thermoelectric properties of a wide variety of low-dimensional materials. However, these measurements can be achieved only by precise placement of the test-materials on specific regions of the testbench. The previous versions of testbenches have required tedious manipulation of the test-materials using scanning microscope tips or optical tweezers etc. making these methods fairly slow and complex [3, 4]. To overcome these limitations, we have an innovative layout of the testbench consisting of a high surface density of test-sites in the central area of the chip. When a droplet of solution containing low-dimensional materials is placed on the testbench, the high surface density of test-sites enhances the probability of landing a single test-material at one of the desired position without any physical manipulation. In principle, the testbench is compatible with any low-dimensional materials which can span across the two thermally isolated test platform tips (to be

described in detail later in this chapter) which in our design are ~1 μm apart from each other. Furthermore, the use of a single platform for accomplishing such measurements will allow for standardization for a variety of low-dimensional materials.

Figure 2-1 shows mask overview and scanning electron microscope (SEM) image of the testbench. The testbench consists of platforms whose suspended tips are closely placed and thermally isolated from each other. Each platform has an embedded heater and thermocouple temperature sensor. The heater and thermocouple junction are placed at the tip of the platform. A platinum pad is on top of the platform and provides electrical connection to the test-material and is electrically insulated from thermocouple and heater by a thin film of aluminium oxide/hafnium oxide layer. If the test-material mechanically spans (bridges) across two neighboring platform tips, a temperature gradient can be induced between two ends of the test-material by heating one of the platforms using the embedded heater. The temperature of both platform tips (i.e. the temperature at the two ends of the test-material) is obtained using the built-in thermocouples and the thermoelectric voltage induced by temperature gradient is measured by the potential difference between the two top platinum pads across which the test-material spans and is electrically connected.

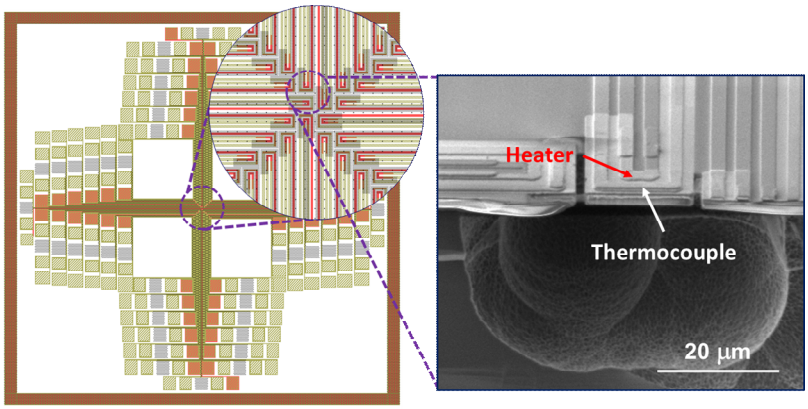

Figure 2-1. (left) Mask overview of the overall testbench chip. Inset shows zoom-in on the central area. (right) Oblique-view SEM image of testbench showing undercut tip area.

The testbench was designed based on following considerations:

1) High density of test-sites. 52 platform tips are gathered at the central area (250 μm × 250 μm) of the chip for improving the probability that a single test-material is bridged between two neighboring platform tips when test-materials are drop-cast from solution. It also provides the possibility of obtaining several test samples on one chip, which results in easiness to have averaged data. It in turn provides more reliable information.

2) Neighboring (tessellated) platform tips that are thermally isolated from each other. The platform is realized into cantilever-like structure, with freestanding tip-regions, to thermally isolate the neighboring platform tips and minimize the flow of parasitic heat through the substrate. This design also concentrates heat at the tip of platform.

3) Reliable and sensitive temperature sensing. Thermistors are one of the most commonly used sensors for the measurement of temperature. However, measuring resistance produces additional Joule heat that might cause unintentional temperature rise and the noise associated with the current source eventually limits the sensitivity of such measurements. On the contrary, thermocouples provide a simple method for measurement of temperature and use no active power dissipation to achieve temperature measurement. Due to the large Seebeck coefficient of polysilicon, in this work we used polysilicon-gold thermocouple as the embedded temperature sensor in each platform.

2.2 Fabrication Process

Figure 2-2 is a schematic diagram showing fabrication process of the testbench sample. A 10 × 10 array of 5 mm^2-sized devices is patterned on a 4" silicon wafer. The fabrication process begins with the deposition of a stress-compensated stack (0.3 μm-thick low pressure chemical vapor deposition (LPCVD) silicon nitride/1.4 μm-thick LPCVD silicon dioxide/0.3 μm-thick

LPCVD silicon nitride) and 0.4 μm-thick LPCVD polysilicon layer (boron-doped, 10^{19} cm^{-3}) on a silicon wafer. The rest of fabrication steps are as follows:

1) The polysilicon layer is patterned to define heater and one leg of thermocouple by photolithography and reactive ion etching (RIE) (Figure 2-2(a)).

2) Thermocouple structure is completed by aligning the titanium/gold leg to the polysilicon leg. 20 nm-thick titanium/350 nm-thick gold layer are deposited and patterned using e-beam evaporation and lift-off process (Figure 2-2(b)).

3) A 20 nm-thick aluminium oxide/30 nm-thick hafnium oxide is deposited by atomic layer deposition (ALD) (Figure 2-2(c)). This layer electrically insulates heater and thermocouple from following metal layer.

4) A 30-nm thick titanium/100 nm-thick platinum/150 nm-thick nickel layer is patterned by e-beam evaporation and lift-off process (Figure 2-2(d)).

5) The RIE and deep reactive ion etching (DRIE) are performed to etch the ALD layer, stress-compensated stack and ~20 μm into the silicon substrate using nickel and photoresist layers as the mask (Figure 2-2(e)).

6) The silicon substrate is etched in an isotropic manner by xenon difluoride (XeF_2) etching and any remaining nickel hard-mask layer is removed by wet etching (Figure 2-2(f)).

7) By drop-cast method, test-material is positioned between two neighboring platform tips. After identifying potential test-materials that successfully span the platinum pads on neighboring platform tips, electron beam induced deposition (EBID) or focused ion beam induced deposition (FIBID) of platinum is used to provide mechanical anchors and good electrical and thermal contact between test-material and platinum pads (Figure 2-2(g)).

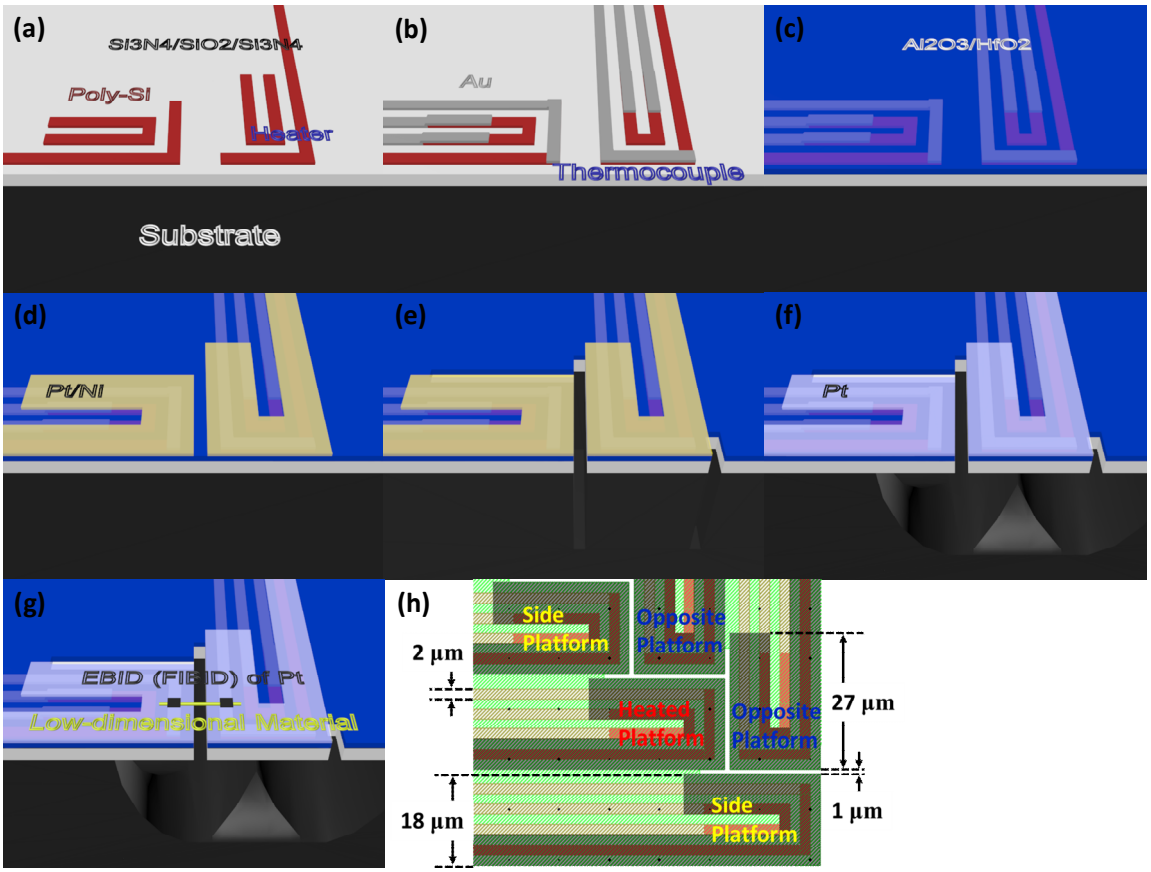

Figure 2-2. (a)-(g) Schematic diagram of fabrication process. (h) Size of each pattern and naming rule for platforms.

Figure 2-2(h) shows the size of each pattern and the naming rule for platforms that is used in the dissertation. There are four platform tips around the heated platform tip. The two platforms perpendicular to the heated plarform are called “opposite platform”. The other two platforms are called “side platform”. The heated and side platforms are not used as a pair in the measuremnt due to the insufficient thermal insulation. The “neighboring platforms” means a pair of heated and opposite platforms.

2.3 Testbench Characterization

2.3.1 Electrical Characteristics

Electrical connectivity and leakage were tested using Keithley 4200-SCS. Because the heater and the thermocouple are composed of polysilicon and gold, the native oxide on the polysilicon surface might result in contact resistance at the junction between polysilicon and gold. Because the contact resistance can usually vary from sample to sample, it will cause variations in the Seebeck coefficient of thermocouple. In such a case, it is necessary to calibrate every single thermocouple, which can be tedious and time-consuming. Furthermore, if the heater has significantly large contact resistance, the assumption that the Joule heat is produced in the polysilicon, which is used for obtaining thermal conductivity, cannot be used. In such a case, we need additional information on how much heat is produced at the junction. As a result, contact resistance can make the measurement more complicated depending upon both its magnitude and variations from sample to sample.

In order to quantitatively estimate the contact resistance, we first obtained the current-voltage characteristic of both thermocouple and heater (Figure 2-3). Both show linear I-V relationship clearly showing the absence of a Schottky barrier. There is a variation in the total resistance of thermocouples as shown Figure 2-3(b). It is because the length of polysilicon varies by platforms depending on the distance between platform tip and wire-bonding pad.

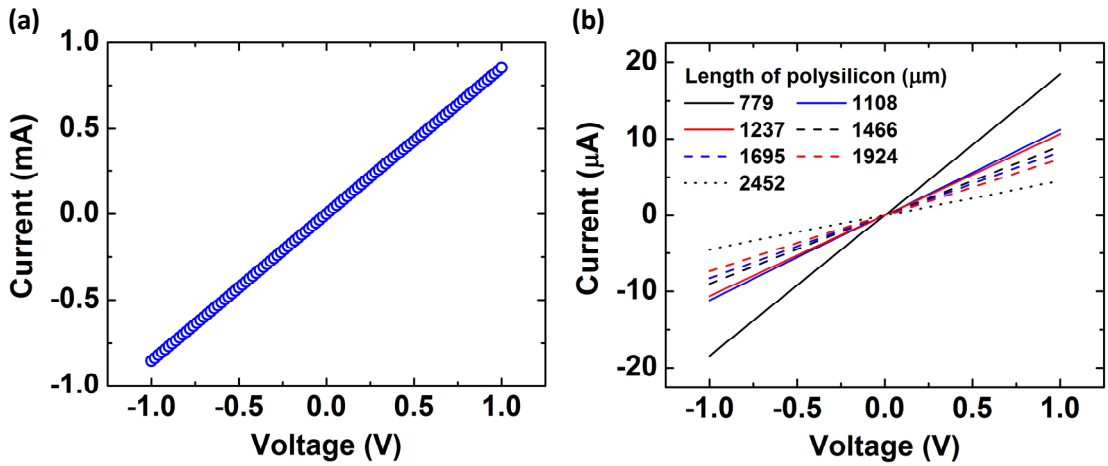

Figure 2-3. Current-voltage characteristic of (a) heater and (b) thermocouples.

For further verification, the measured resistance was compared to the value calculated based on resistivity and cross-sectional area, and length of the fabricated lines. The sheet resistance (146 Ω/sq) of polysilicon film was measured using 4-probe measurement before starting fabrication. Considering the thickness of polysilicon film (400 nm), it corresponds to the resistivity of 58.4 μΩm. Because it is 3 orders of magnitude larger than known resistivity value of gold (0.0244 μΩm), the resistance of thermocouple is dominated by polysilicon and should have linear dependence on the length of polysilicon. Figure 2-4 shows calculated relationship between resistance of thermocouple and length of polysilicon with measured resistance of thermocouples on different platforms. The measured data matches well the calculated data with a mean error of 5.0 %. In case of heater, the resistance is calculated to vary between 1.22 and 1.29 kΩ once again depending upon the length of the gold lines connecting the polysilicon to the contact pads. However, the measured resistance was found to vary between 1.00 and 1.25 kΩ. The variation in the measured values and the difference between measured and calculated values are larger for the heater as compared to the case of thermocouple because polysilicon heater is small and has sharp corners. Because the length of polysilicon heater is fixed for all devices to be 16 μm, small

misalignment between polysilicon heater and gold line result in large percentage change in the effective length of polysilicon. Furthermore, corner rounding effect in photolithography also causes some variations in shape of polysilicon heater. These errors are insignificant in the case of thermocouple since the polysilicon leg is typically very long (mm in length) and therefore small lithographic errors contribute negligibly to the overall resistance error.

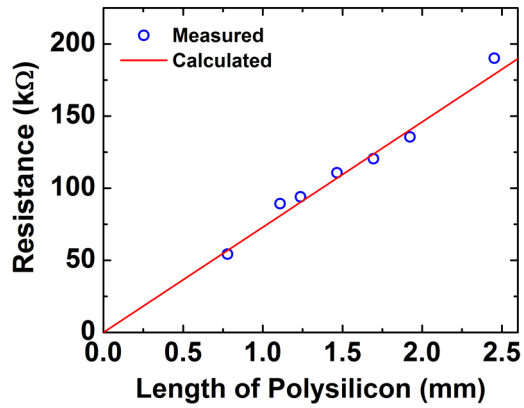

Figure 2-4. Resistance of thermocouples in accordance with length of polysilicon.

Electrical insulation was next measured between the thermocouple - heater and the top platinum pad - heater since any leakage between these structures can readily corrupt the thermoelectric voltage measured by thermocouple temperature sensor or thermoelectric circuit consisting of test-material and platinum pad. Since measurements are performed using ac currents (to be described next), some amount of leakage through capacitive coupling is inevitable and needs to be small enough to be within acceptable limits. Although 1ω leakage signal can be filtered by lock-in amplifier, non-linear effects can result in erroneous 2ω thermoelectric signals if considerably large leakage occurs. In order to test leakage, the dc voltage was applied between heater and thermocouple or heater and platinum pad and the current was monitored (Figure 2-5). There is no sign of dielectric breakdown up to 2 V. This was adequate for the proposed

measurements since the heating voltage used in the experiments was less than 1 V_{rms} and there is no directly applied voltage between heater and thermocouple or heater and platinum pads in actual measurement. The voltage will be applied between two legs of heater.

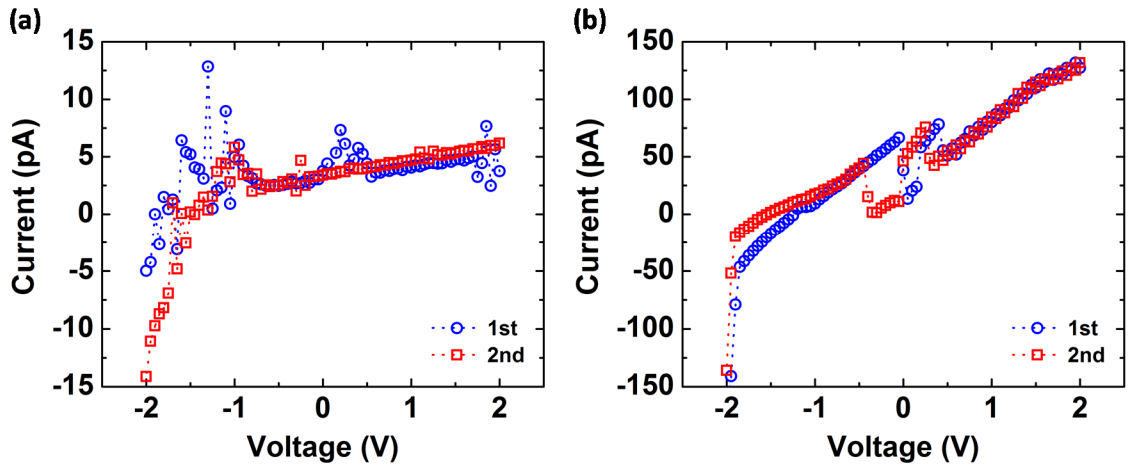

Figure 2-5. Leakage current (a) between heater and thermocouple and (b) between heater and platinum pad.

Further verification of the testbench operation as a thermal test platform was performed. In this case, an input sine wave signal was applied to heater and the thermocouple voltage was monitored to track the temperature of the test platform tip. In the absence of leakage current, the magnitude of the thermocouple voltage is identical between negative and positive half of the drive voltages (heating voltages) and the thermocouple (output) voltage shows a square dependence on the drive sine wave because Joule heat is proportional to square of heating voltage. As shown in Figure 2-6, the testbench was confirmed to satisfy these conditions.

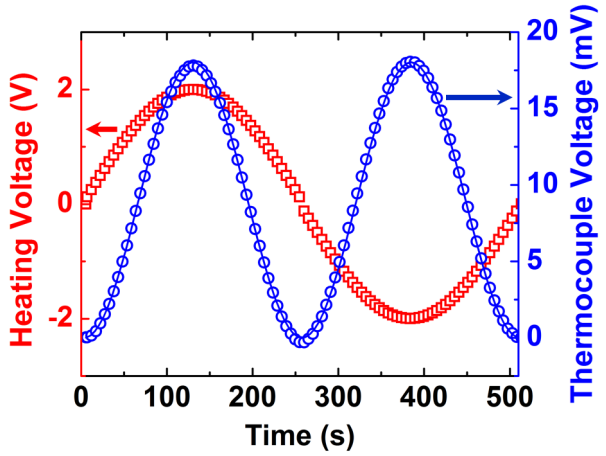

Figure 2-6. Sine wave heating voltage and corresponding thermoelectric voltage. The blue solid line is fitting square of sine curve.

2.3.2 Thermal Characteristics

The thermal cross-talk between neighboring platform tips was checked before and after isotropic trench etching by XeF_2 which releases the tips of the platforms from the substrate. The objective of isotropic trench etch is to turn the platform into a cantilever-like thermally isolated structures at the tips. It provides two main advantages: 1) Neighboring adjacent platform tips are better thermally isolated from each other by increased length of parasitic heat path through the substrate, and 2) The generated heat at the tip through the heater remains concentrated at the tip of platform as well as leads to a higher temperature rise due to the reduced thermal mass of this region. Figures 2-7 presents oblique-view SEM image showing the dependence of the shape of trench on the number of etching cycles and optical microscopic image of the platforms after 10 cycles of etching. As shown in Figures 2-7(c) and (d), the platform tip is suspended enough after 10 cycles. We did not use more cycles because further undercut of the platform results in a very fragile structure which have a very high likelihood of being broken during etching process (20 cycles) or drop-casting step of the test-materials (15 cycles).

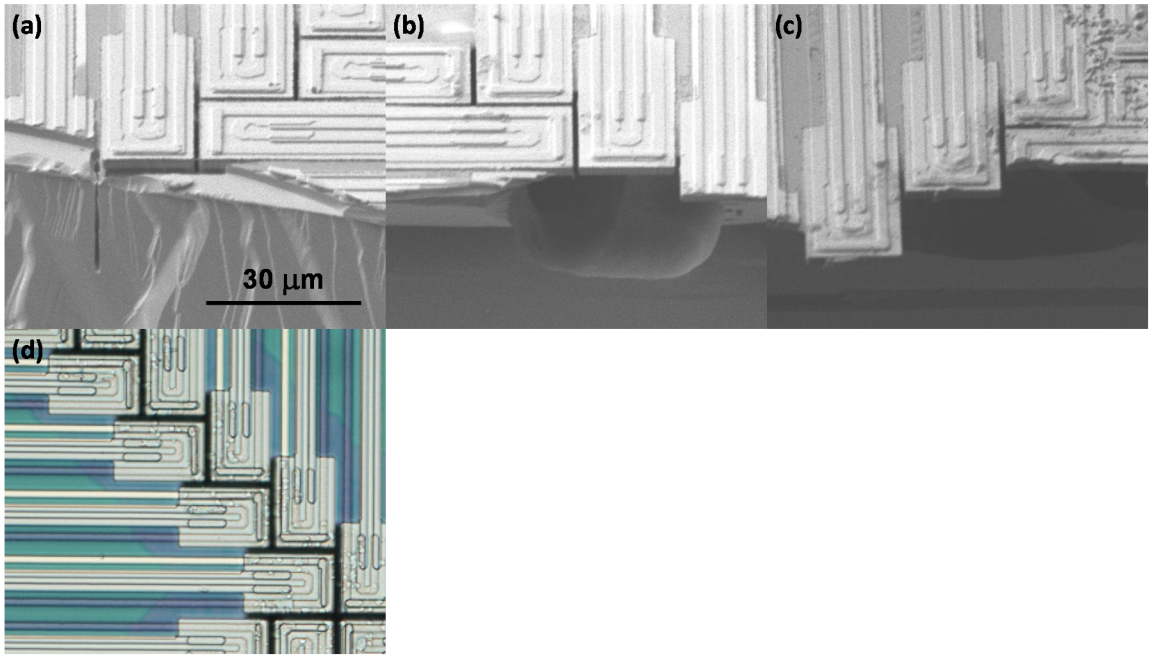

Figure 2-7. Oblique-view SEM images of testbench (a) before XeF_2 etching, (b) after 5 cycles of XeF_2 etching, and (c) after 10 cycles of XeF_2 etching. (d) Optical microscopic image of testbench after 10 cycles of XeF_2 etching

In order to check thermal cross-talk, ac heating voltage of frequency 12 Hz ($=\omega/2\pi$) was applied to the heater using Keithley 3390 function generator and the 2ω signal of thermocouple voltage of heated and opposite platforms was monitored using SR 830 lock-in amplifier. Figure 2-8(a) shows thermocouple voltage of released and unreleased heated platforms. The voltage of thermocouple on the heated platform for the released platform is 24 times larger than that for unreleased platform. This is because the thermal mass of the platform tip is reduced and the thermal resistance from platform tip to heat sink (substrate) is increased by post-releasing. Furthermore, the ratio of thermocouple voltage of opposite platform to that of heated platform is decreased by a factor of 38 by releasing the platform (Figures 2-8 (a) and (b)). This value sets the minimum measurable thermal conductance of the test-materials by the testbench. If this parasitic thermal transport through the substrate is larger than that of test-material, accurate measurement of thermal conductivity of test-material cannot be accomplished.

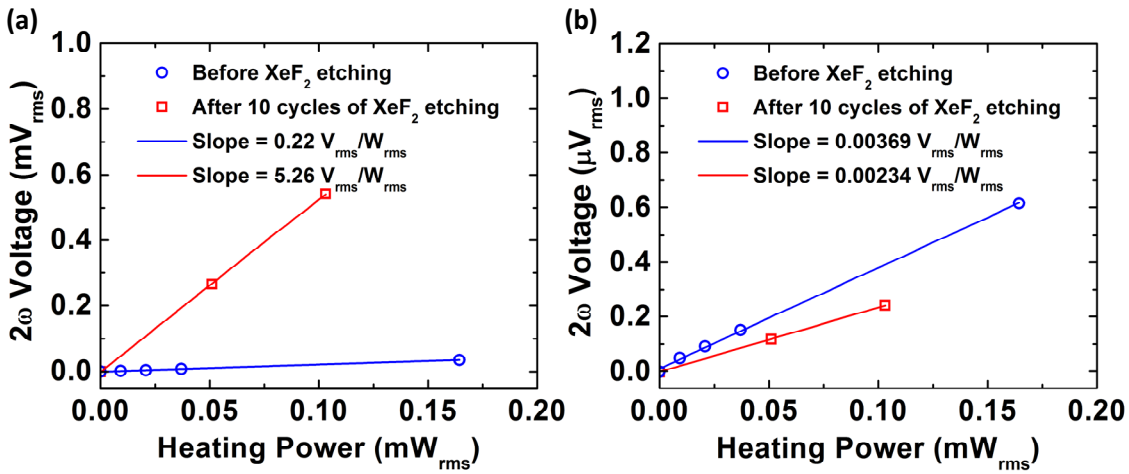

Figure 2-8. Thermocouple voltage of (a) heated and (b) opposite platforms as a function of heating power before and after 10 cycles of XeF_2 etching.

As mentioned previously, ac drive signals are used in actual thermal and thermoelectric measurement in this work because these allow for high sensitivity measurements through the use of lock-in amplifier. The thermocouple monitors time-dependent temperature fluctuation of platform tip provided by ac heating voltages. However, as to be expected, the temperature fluctuations start to roll down as frequency increases beyond the thermal time constant of the platform tip. This frequency response is governed by

$$\Delta T = \frac{\Delta T_0}{\sqrt{1 + (f/f_{3dB})^2}} \tag{2.1}$$

where f_{3dB} is the 3-dB cut-off frequency (corner frequency), and ΔT_0 is the temperature rise of platform tip induced by dc heating voltage. The 3-dB cut-off frequency, which is equivalent to inverse of thermal time constant, needs to be determined because it limits the highest frequency that can be used in these measurements. It was investigated by measuring 2ω voltage of thermocouple using SR 830 lock-in amplifier while sweeping frequency (=ω/2π) of heating voltage from 2 Hz to 9 kHz using Keithley 3390 function generator. The testbench was placed in a vacuum cryostat at an ambient pressure below 5×10^{-6} Torr. Figure 2-9 shows the response of

the thermocouple voltage as a function of frequency for a constant power dissipated in the heater. Although the 3-dB cut-off frequency is around 1.2 kHz, 100 Hz is the maximum frequency that can be used in these measurements because the thermocouple voltage starts to roll down above 100 Hz.

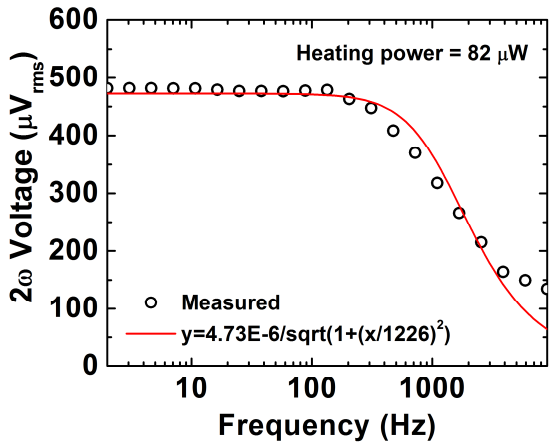

Figure 2-9. Frequency response of thermocouple voltage. The red solid line is fitting curve obtained using Equation (2.1).

2.3.3 Calibration of Thermocouple

The polysilicon-gold thermocouple is intended to measure the temperature rise of the platform tip produced by heating power. However, a calibration is necessary for extracting temperature rise from thermocouple voltage. It needs to be done at various temperatures for measuring thermal and thermoelectric properties as a function of temperature. It was accomplished based on the assumption that within a certain range of temperature the Seebeck coefficient changes linearly as a function of temperature and the temperature of thermocouple junction changes linearly according to the heating power. Using this assumption, we can express the thermocouple voltage in terms of the heating power by

$$V_{TC} = \int_0^{\Delta T} S(T + \Delta T')d\Delta T' \tag{2.2}$$

$$= \int_0^{\Delta T} [S(T) + m\Delta T']d\Delta T'$$

$$= S(T)\Delta T + \frac{m}{2}\Delta T^2$$

$$= S(T)nP_H + \frac{mn^2}{2}P_H^2$$

where S is the Seebeck coefficient, T is the cryostat temperature, ΔT is the temperature rise of thermocouple junction, m is the change in the Seebeck coefficient per unit temperature, P_H is the heating power, and n is the ratio of the temperature rise of thermocouple junction to the heating power. Differentiating Equation (2.2) with respect to heating power gives

$$\frac{dV_{TC}}{dP_H} = S(T)n + mn^2P_H \tag{2.3}$$

The derivative of thermocouple voltage with respect to the heating power can be obtained from the measurement of the thermocouple voltage vs. the heating power. If it is plotted as a function of heating power, according to Equation (2.3), the slope (α) and y-intercept (β) of the plot is related to $S(T)$, n, and m by

$$\alpha = mn^2 \tag{2.4}$$

$$\beta = S(T)n \tag{2.5}$$

Therefore, if we know m, we can calculate $S(T)$.

Let us suppose that we already obtained the Seebeck coefficient at any one temperature (T_o) by using a certain method which will be explained later in this section. In case that the cryostat temperature (T) is below T_o, m can be given by

$$m = \frac{S(T_o) - S(T)}{T_o - T} \tag{2.6}$$

where $T_o - T$ needs to be small enough to satisfy the predefined assumption that the Seebeck coefficient changes linearly as a function of temperature and the temperature of thermocouple junction changes linearly according to the heating power. Using Equations (2.4), (2.5), and (2.6), $S(T)$ can then be expressed as

$$S(T) = \frac{-\beta^2 + \sqrt{\beta^4 + 4\alpha\beta^2(T_o - T)S(T_o)}}{2\alpha(T_o - T)} \tag{2.7}$$

Hence, we can obtain $S(T)$ from $S(T_o)$ by measuring the thermocouple voltage as a function of heating power at the cryostat temperature of T.

On the other hand, in order to obtain the Seebeck coefficient at the temperature above T_o, we need to measure the derivative of thermocouple voltage with respect to the heating power at the cryostat temperature of T_o. Equations (2.5) and (2.6) are then changed to

$$\beta = S(T_o)n \tag{2.8}$$

$$m = \frac{S(T) - S(T_o)}{T - T_o} \tag{2.9}$$

Once again, $T - T_o$ needs to be small enough to satisfy the predefined assumption. Substituting and rearranging Equations (2.4), (2.8), and (2.9) gives

$$S(T) = \frac{\alpha(T - T_o)}{\beta^2} S^2(T_o) - S(T_o) \tag{2.10}$$

Therefore, we can obtain $S(T)$ from $S(T_o)$ by measuring the thermocouple voltage as a function of heating power at the cryostat temperature of T_o. As a result, if we know the Seebeck coefficient at any one temperature, we can calculate the Seebeck coefficient at various temperatures using Equations (2.7) and (2.10) and the plot of the derivative of thermocouple voltage with respect to heating power as a function of heating power.

Initially, we measured the thermocouple voltage as a function of heating power at the cryostat temperatures of every 10 or 20 K between 300 and 15 K. Figure 2-10(a) shows the derivative of the thermocouple voltage with respect to the heating power as a function of heating

power at T = 280 K. Keithley 2400 source meter was used to drive the heater and measure the heating power while the thermocouple voltage was measured using Keithley 2182A nanovoltmeter (Figure 2-10(b)). A specific structure shown in Figure 2-10(b) was used for this measurement because it was found that the electrical coupling between heater and thermocouple makes the derivative of thermocouple voltage noisy when we use the heater and thermocouple of same platform. Specifically, the calibration structure, which is included on each of the testbench, consists of two platform tips are connected to each other through a 2 μm-wide bridge consisting of stress-compensated stack/ALD/titanium/platinum layers and was incorporated as part of the mask design of the testbench.

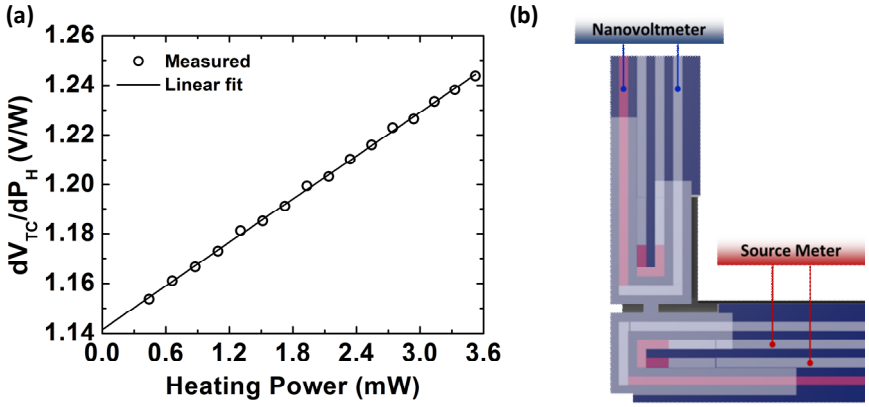

Figure 2-10. (a) Derivative of thermocouple voltage with respect to heating power as a function of heating power at T = 280 K (P_H: heating power, V_{TC}: thermocouple voltage) (b) Schematic illustration of measurement set-up for the derivative of thermocouple voltage with respect to heating power.

As explained before, we still need to know the Seebeck coefficient at any one temperature to complete the calibration. In order to satisfy this condition, we obtained the Seebeck coefficient at T = 300 K by using the heater as a thermistor. The heater resistance at T = 300 K was measured using small dc current (±20 μA) so as not to heat the resistor. Thereafter, the resistance of heater and thermocouple voltage were measured while sweeping current from 20 μA

to 600 μA. Figure 2-11(a) shows resistance of heater and thermocouple voltage as a function of heating power. Keithley 2400 source meter was used to drive the heater and to measure its resistance while the thermocouple voltage was measured using Keithley 2182A nanovoltmeter as shown in Figure 2-11(b). The cryostat temperature thereafter increased to 310 K and the resistance of the heater was measured using small current. The drive power that results in a 10 K rise in temperature was then determined by matching the drive power that results in a resistance of the heater at 300 K equal to the resistance of the heater obtained at T = 310 K. Simultaneously, the corresponding thermocouple voltage was also measured. However, this calibration has still an error which needs to be estimated and compensated due to the fact that the entire platform tip is not at a uniform temperature unlike in the case where the device is allowed to equilibrate in the cryostat.

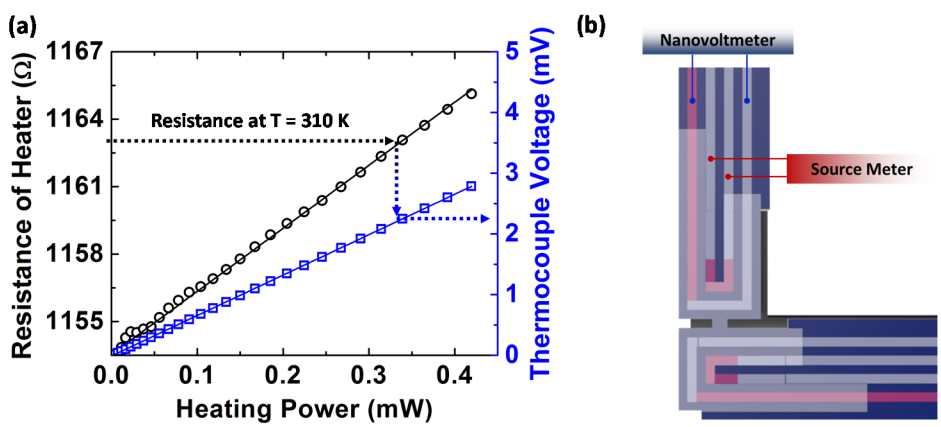

Figure 2-11. (a) Resistance of heater and thermocouple voltage as a function of heating power at T = 300 K. (b) Schematic illustration of measurement set-up for thermocouple calibration at T = 300 K.

In order to obtain the temperature rise of thermocouple junction based on the heat dissipated in the heater, COMSOL finite element modeling (FEM) was performed, as shown in Figure 2-12. Table 2-1 shows thermal conductivity of the various materials constituting testbench

that was used in the FEM analysis. Bulk values of thermal conductivity were used for gold and silicon [7], whereas for platinum, the thermal conductivity was calculated from measured electrical conductivity using Wiedemann-Franz law. For the rest of materials, thermal conductivity values were obtained from reported values in literature [5-9]. For a power dissipation of 0.334 mW at 300 K resulting in a heater resistance corresponding to a resistance value at 310 K, FEM simulation shows that the temperature rise of thermocouple junction is 24.1 % smaller than that of heater. It means that thermocouple voltage corresponding to temperature rise of 10 K in heater corresponds to a temperature difference of 7.59 K between hot junction of the thermocouple located on the platform tip and the cold junction located at the bonding pads at the ambient temperature set by the cryostat. Using this method, the Seebeck coefficient of the thermocouple was calculated to be 292 μV/K.

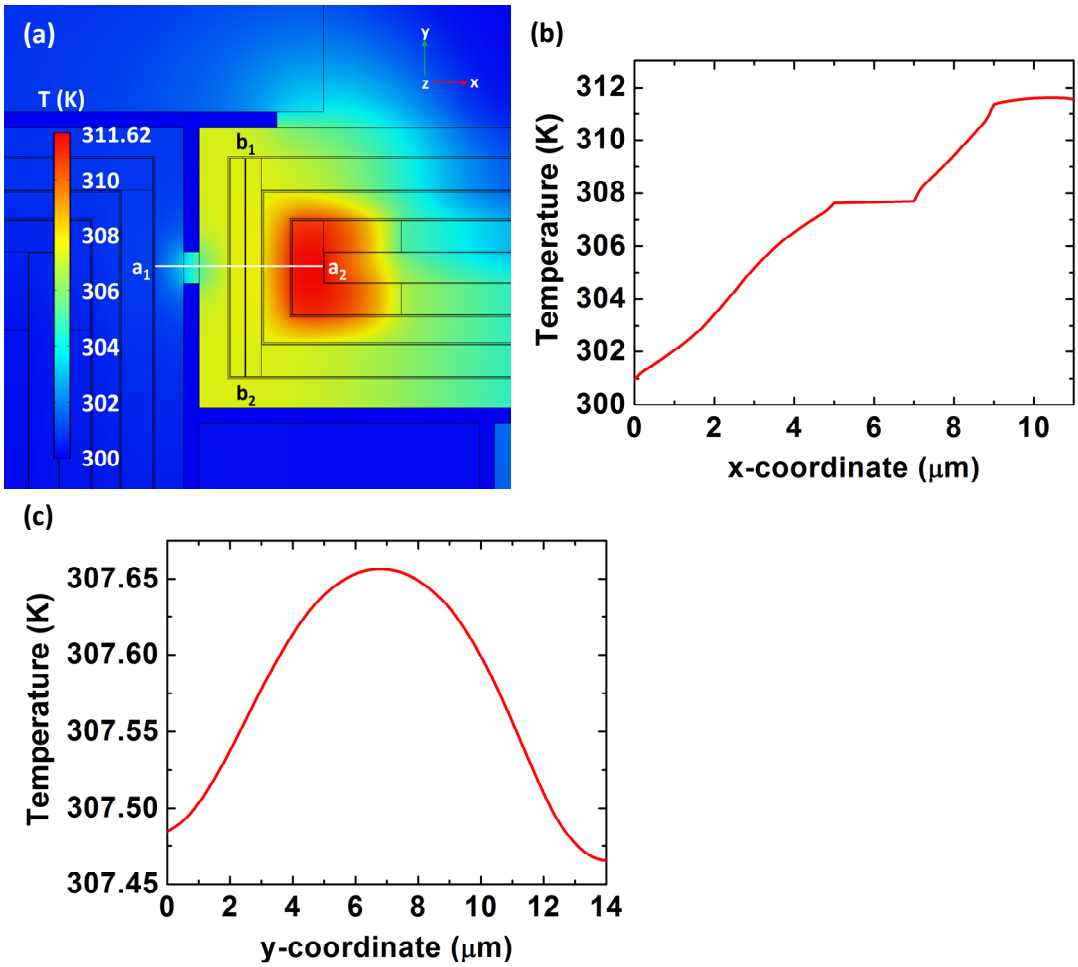

Figure 2-12. Results of FEM analysis for the calibration structure of the testbench at T = 300 K. (a) Color plot of temperature distribution. (b) Temperature profile along the cut-line a_1-a_2 (from the opposite platform to the mid-point of the heater). (c) Temperature profile along the cut-line b_1-b_2 (along the hot junction). z-coordinate value of cut-lines is at the interface between stress-compensated stack and heater. The temperature in (b) and (c) is not equal to the values used for calibration that are averages taken across the volume. For the analysis, COMSOL multiphysics 4.2a was used and the effect of air conduction and radiation was not included. The temperature of bottom of substrate and the power dissipated by the heater were defined as 300 K and 0.334 mW.

Materials	κ (W/m-K)
ALD hafnium oxide	1 [8]
ALD aluminium oxide	1 [9]
LPCVD silicon nitride	3.2 [10]
LPCVD silicon dioxide	1.1 [11]
LPCVD polysilicon	45 [12]
Gold	317
Platinum	24
Silicon	148

Table 2-1. Thermal conductivity of the various materials constituting testbench.

Based on the obtained Seebeck coefficient at $T = 300$ K, we calculated the Seebeck coefficient at $T = 280$ K using Equation (2.7) and the measured derivative of thermocouple voltage with respect to heating power at the cryostat temperature of 280 K. Afterward, the Seebeck coefficient at $T = 260$ K was obtained from the Seebeck coefficient at $T = 280$ K using the same calculation. By continuously using this method at lower temperatures, the polysilicon-gold thermocouple was calibrated between 300 and 15 K (Figure 2-13).

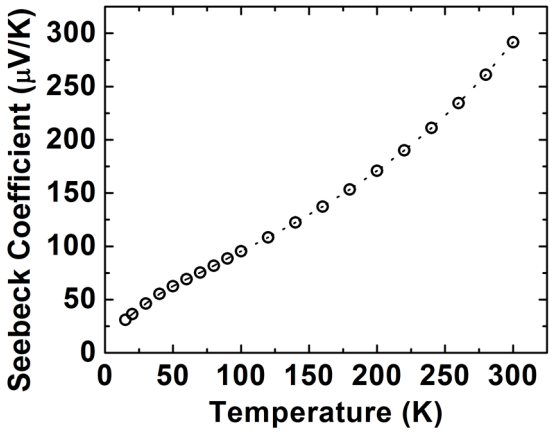

Figure 2-13. Seebeck coefficient of polysilicon-gold thermocouple as a function of temperature.

2.4 Measurement of Thermal Conductivity, Seebeck Coefficient, and Electrical Conductivity

Figure 2-14 shows a schematic illustration of the measurement set-up for thermal and thermoelectric properties of low-dimensional materials. The testbench is placed in a vacuum cryostat with pressure below 5×10^{-6} Torr to minimize the effect of conduction through ambient air. A sinusoidal voltage with angular frequency ω is applied to polysilicon heater using Keithley 3390 function generator for heating platform tip. It produces 2ω temperature fluctuation because heating power is proportional to square of heating voltage. The temperature rise of the heated and the opposite platform tips across which the test-material spans is obtained by measuring the respective 2ω voltage of the polysilicon-gold thermocouple using SR 830 lock-in amplifier. Simultaneously, the heating current and voltage are measured using Keithley 2001 and Keithley 2000 multimeters respectively for calculating the amount of heat dissipated in the heater (heating power). All these measurements are accomplished by writing a program for automated data acquisition using Labview® software. The output voltage of the function generator is not used for calculating the heating power because the voltage actually applied to heater was found to be different from the set-amplitude and depends upon the resistance of the heater due to small output impedance of function generator (50 Ω). The SR 830 lock-in amplifier is also used to measure the 2ω voltage between the two platinum pads of the neighboring platforms connected to each other through test-material which is the thermoelectric voltage induced in thermoelectric circuit consisting of test-material and platinum pad. The thermoelectric voltage induced in the thermocouple or thermoelectric circuit consisting of test-material and platinum pad is equal to 2 times 2ω voltage measured by lock-in amplifier. It is because 2ω voltage has the dc offset that is half of peak-to-peak amplitude as shown in Figure 2-6 and lock-in amplifier detects the amplitude of ac component regardless of input dc offset.

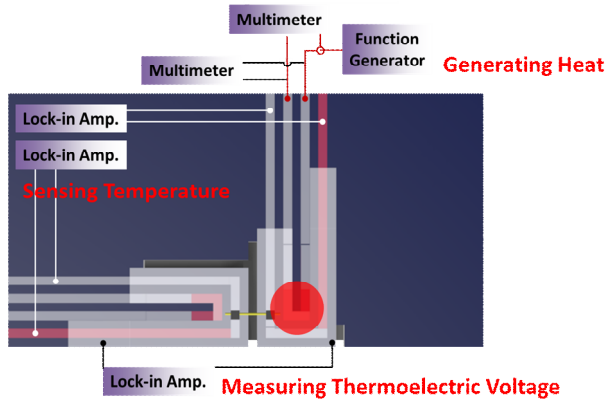

Figure 2-14. Schematic illustration of measurement set-up for thermal and thermoelectric properties of low-dimensional materials.

2.4.1 Thermal Conductivity

An equivalent thermal circuit is used to extract the thermal conductivity of the test-material from the measured heating power and the resulting temperature rise of both thermocouple junctions on the neighboring platform tips across which the test-material spans. Figure 2-15 shows the equivalent thermal circuit of two platforms connected to each other through test-material. The heat generated in the heater will transfer to the heat sink (bottom of substrate) through two paths. One is direct path to bottom of substrate. Another path is through the test-material. Hence,

$$P_H = P_1 + P_2 \tag{2.11}$$

where P_H, P_1, and P_2 are the input heating power, the amount of heat transferring through test-material, and the amount of heat transferring direct to bottom of substrate, respectively. According to the thermal circuit, temperature rise of the heater on heated platform tip ($\Delta T_{HP(H)}$) and thermocouple junction on opposite platform tip ($\Delta T_{OP(TC)}$) can be expressed as

$$\Delta T_{HP(H)} = P_1\left(R_{th\_LDM} + R_{th\_OP} + R_{th\_C}\right) = P_2 R_{th\_HP} \tag{2.12}$$

$$\Delta T_{OP(TC)} = P_1 R_{th\_OP} \tag{2.13}$$

where R_{th_LDM}, R_{th_OP}, and R_{th_HP} are the thermal resistance of the test-material (low-dimensional material), the thermal resistance between the thermocouple junction on opposite platform tip and the heat sink, and the thermal resistance from the heater on heated platform tip to the heat sink, respectively. R_{th_C} represents sum of the thermal resistance from the heater on heated platform tip to the test-material and from the test-material to the thermocouple junction on the opposite platform tip (i.e. the effective contact resistance). Using Equations (2.11), (2.12) and (2.13), R_{th_LDM} can be expressed as

$$R_{th\_LDM} = \frac{P_H}{\Delta T_{OP(TC)}} R_{th\_HP} R_{th\_OP} - R_{th\_HP} - R_{th\_OP} - R_{th\_C} \tag{2.14}$$

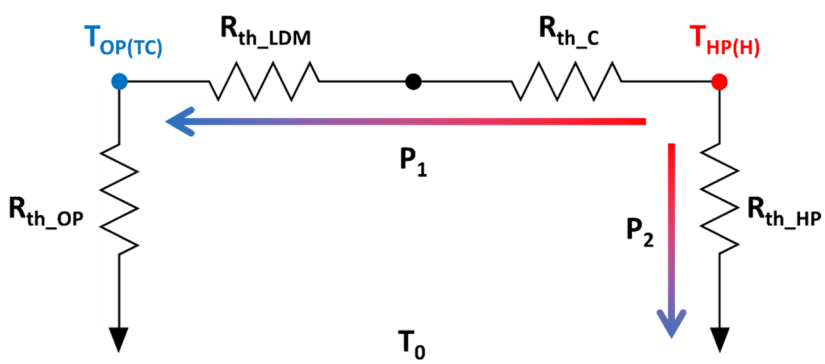

Figure 2-15. Equivalent thermal circuit of two neighboring platforms connected to each other through test-material.

P_H *and* $\Delta T_{OP(TC)}$ are obtained directly from the measurement. However, the measured $\Delta T_{OP(TC)}$ needs to be corrected by subtracting the temperature rise produced by parasitic heat transfer ($\Delta T_{OP(TC)\_para}$), such as conduction through substrate, air conduction, and radiation. In order to obtain the information on $\Delta T_{OP(TC)\_para}$, we measured the temperature rise of the thermocouple junctions on the heated and opposite platform tips without depositing test-material.

Because there is no test-material connecting the two platforms, the measured temperature rise of the thermocouple junction on the opposite platform is equivalent to $\Delta T_{OP(TC)\_para}$. The ratio of $\Delta T_{OP(TC)\_para}$ to $\Delta T_{HP(TC)}$ is plotted as a function of temperature in Figure 2-16. This plot allows us to obtain $\Delta T_{OP(TC)\_para}$ from $\Delta T_{HP(TC)}$ and correct the measured $\Delta T_{OP(TC)}$ in case when the test-material is anchored between platform tips. $\Delta T_{OP(TC)\_para}$ is mainly caused by heat transfer through substrate. Although heat transfer by air conduction and radiation also contribute to it, these are estimated to be at least 100 times smaller than the measured values at $T = 300$ K based on calculations using Stefan-Boltzmann law and the thermal conductivity of air at a pressure of 10^{-5} Torr.

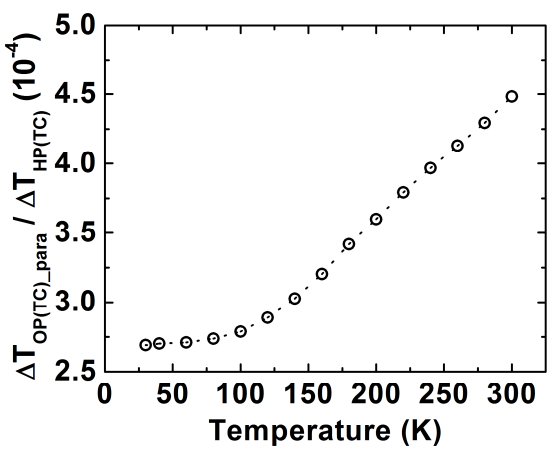

Figure 2-16. Ratio of temperature rise of thermocouple junction on opposite platform tip caused by parasitic heat transfer ($\Delta T_{OP(TC)\_para}$) to that of thermocouple junction on heated platform tip ($\Delta T_{HP(TC)}$).

R_{th_HP}, R_{th_OP}, and R_{th_C} cannot be obtained directly from the measurements. Instead, COMSOL FEM is used to obtain $R_{th\_HP}R_{th\_OP}$ and $-(R_{th\_HP}+R_{th\_OP}+R_{th\_C})$ of Equation (2.14). Thermal conductivity of the various materials constituting testbench used in the FEM analysis is listed in Table 2-1. The procedure is as follows: i) Build a dummy structure representing test-

material based on the SEM image of the sample (Figure 2-17(a)). ii) Derive $\Delta T_{OP(TC)}$ while fixing the heating power as the measured value and changing R_{th_LDM} (Figure 2-17(b)). iii) Plot R_{th_LDM} as a function of $P_H/\Delta T_{OP(TC)}$ (Figure 2-17(c)). According to Equation (2.14), the slope and y-intercept of this plot is equivalent to $R_{th\_HP}R_{th\_OP}$ and $-(R_{th\_HP}+R_{th\_OP}+R_{th\_C})$, respectively.

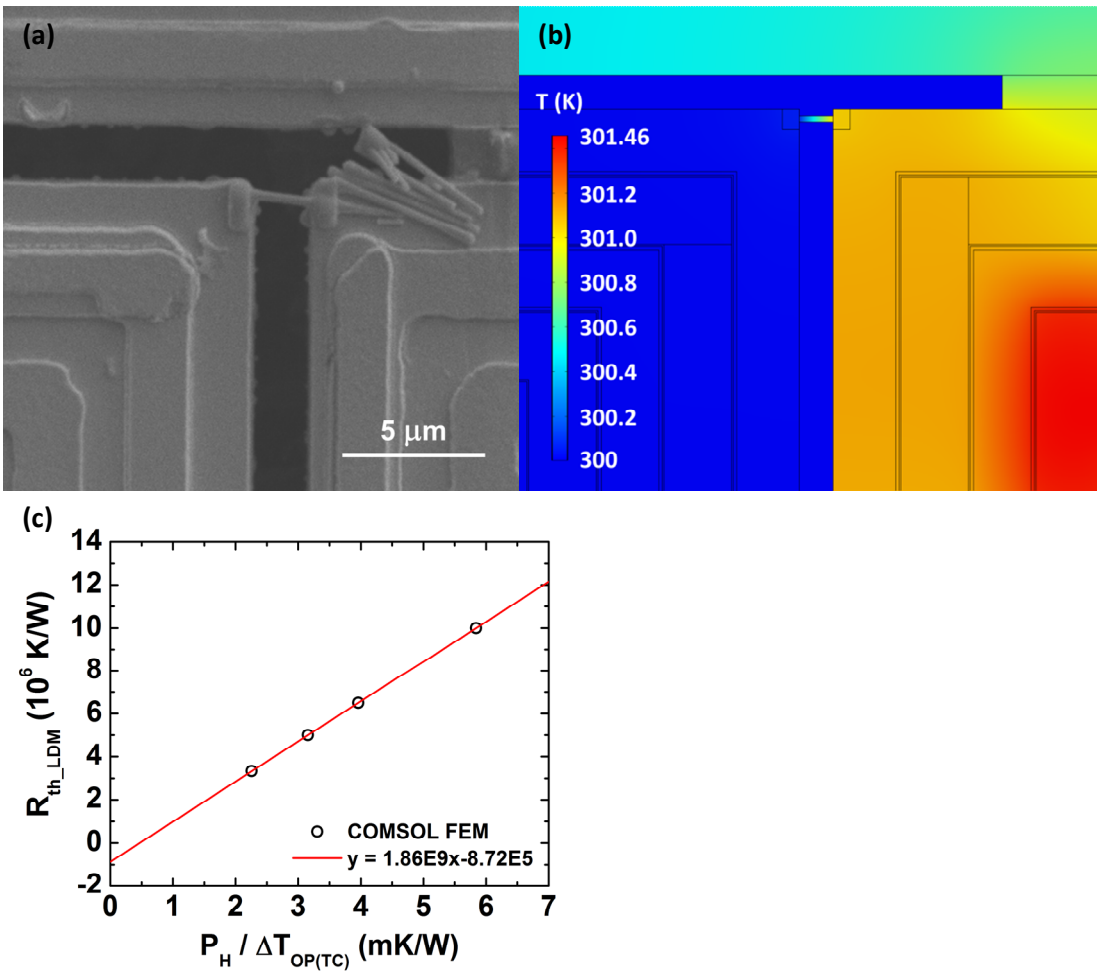

Figure 2-17. (a) SEM image of the testbench on which test-material (GaAs/MnAs core/shell nanowire) is anchored. (b) Image of COMSEL FEM showing temperature distribution of the sample. (c) Relationship between the thermal resistance of test-material and the heating power divided by temperature rise of thermocouple junction on opposite platform tip.

Although COMSOL FEM can provide $R_{th\_HP}R_{th\_OP}$ and $-(R_{th\_HP}+R_{th\_OP}+R_{th\_C})$ at $T = 300$ K, it cannot be applicable at various temperatures due to the lack of data on the thermal conductivity of the various materials constituting testbench. Hence, we still need to know how $R_{th\_HP}R_{th\_OP}$ and $-(R_{th\_HP}+R_{th\_OP}+R_{th\_C})$ change with temperature for calculating R_{th_LDM} at various temperatures. The temperature dependence of R_{th_HP}, R_{th_OP}, and R_{th_C} was obtained by monitoring the temperature rise of the heated platform tip as a function of ambient temperatures without depositing test-material. Figure 2-18 shows the temperature rise of the thermocouple junction on the heated platform tip divided by heating power, which is the thermal resistance from platform tip to heat sink, as a function of temperature. R_{th_HP} and R_{th_OP} should have the same temperature dependence. Furthermore, considering that the thermal resistance from the platform tip to the heat sink mainly originates from the thermal resistance of the suspended part of the platform, it is also reasonable to assume that R_{th_C} has the same temperature dependence. Therefore, we can obtain $R_{th\_HP}R_{th\_OP}$ and $-(R_{th\_HP}+R_{th\_OP}+R_{th\_C})$ at various temperatures from the measured temperature dependence of thermal resistance from platform tip to heat sink and the values at $T = 300$ K extracted from COMSOL FEM.

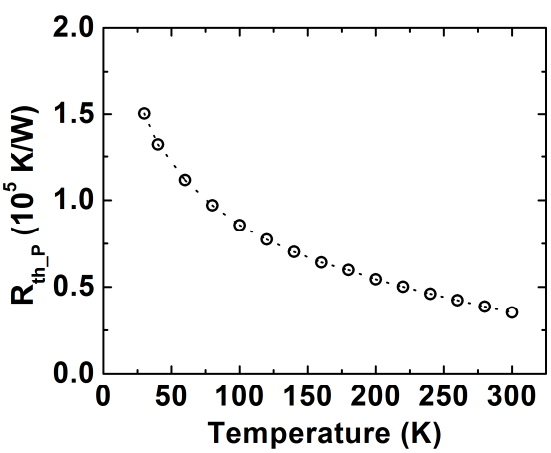

Figure 2-18. Thermal resistance from platform tip to heat sink as a function of temperature.

As a result, we can obtain the thermal conductivity of the test-material from the measured heating power and the resulting temperature rise of the thermocouple junctions on the heated and opposite platform tips by using Equation (2.14) and COMSOL FEM. However, it was found that the temperature rise of the thermocouple junction on the opposite platform tip produced by parasitic heat transfer at $T = 300$ K is equivalent to that produced by the heat transferred through the test-material that has thermal conductance of 9.7×10^{-9} W/K and bridges the two platform tips. Therefore, if the thermal conductance of test-material is comparable to or smaller than this value, the accuracy of the measurement will be reduced.

2.4.2 Seebeck Coefficient

Seebeck coefficient of test-material can be obtained by

$$S_{LDM} - S_{Pt} = \frac{V_{TE}}{\Delta T_{HP(TC)} - \Delta T_{OP(TC)}} \tag{2.15}$$

where S_{LDM}, S_{Pt}, $\Delta T_{HP(TC)}$, $\Delta T_{OP(TC)}$, and V_{TE} are the Seebeck coefficient of test-material, the Seebeck coefficient of platinum, the temperature rise of the thermocouple junction on the heated platform tip, the temperature rise of the thermocouple junction on the opposite platform tip, and the induced thermoelectric voltage, respectively. However, if the test-material lands away from thermocouple junction or the thermal conductance of test-material is large, there might be some temperature difference between thermocouple junction and end of test-material. In such a case, according to equivalent thermal circuit shown in Figure 2-15, the temperature difference between two ends of test-material can be calculated by

$$\Delta T_{HP(LDM)} - \Delta T_{OP(LDM)} = P_1 R_{th\_LDM} = \Delta T_{OP(TC)} \frac{R_{th\_LDM}}{R_{th\_OP}} \tag{2.16}$$

where $\Delta T_{HP(LDM)}$ and $\Delta T_{OP(LDM)}$ are the temperature rise of end of test-material positioned on heated and opposite platform tips. In most cases, S_{Pt} is negligibly small compared to S_{LDM} because

we are interested in materials that exhibit large Seebeck coefficient. However, in case that S_{Pt} is comparable to S_{LDM}, it needs to be added to the measured Seebeck coefficient. It is assumed to be the same as reported diffusive Seebeck coefficient of pure platinum, which is −5.6 μV/K at T = 300 K and linearly decreases with decreasing temperature [13], because phonon-drag effect in evaporated films without being well-annealed is known to be strongly suppressed [14, 15].

2.4.3 Electrical Conductivity

Electrical conductivity is obtained by measuring resistance between two platinum pads connected to each other through test-material. However, measured resistance includes the resistance of the platinum layer. It ranges from 0.7 to 2 kΩ depending on distance between platform tip and wire-bonding pad. It needs to be subtracted from measured resistance, especially when the resistance of test-material is comparable to it. One way to solve this problem is to calculate it from resistivity measured using calibration structure (Figure 2-19(a)) and designed length and cross-section area, and subtract it from measured resistance. Another way is four-probe measurement. During FIBID or EBID process for anchoring test-material on platform tip, we can also electrically connect the platform tips with side platform tips using FIBID, as shown in Figure 2-19(b). If the current is fed through two neighboring platinum layers and the other two layers are used as voltage-sensing probes, the resistance of platinum layers is not included in measured resistance.

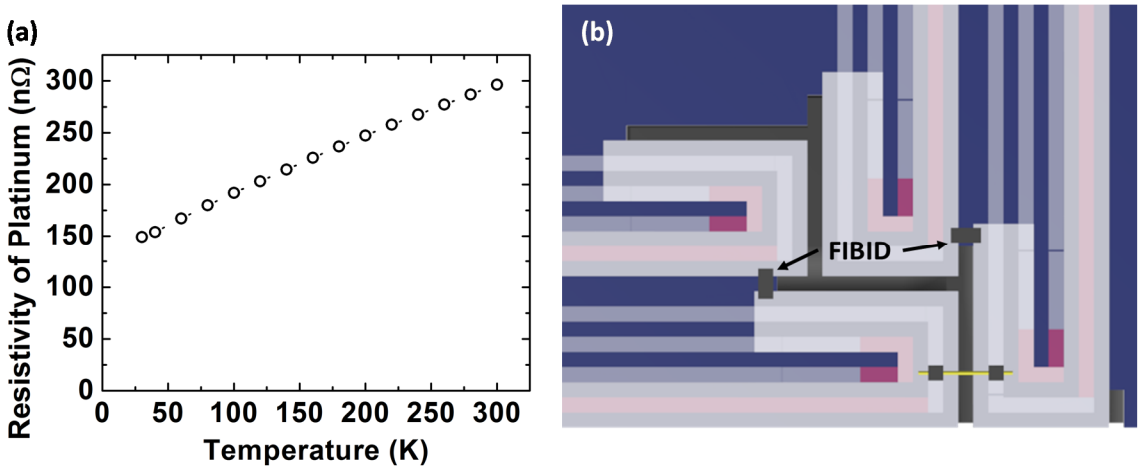

Figure 2-19. (a) Resistivity of platinum obtained using calibration structure as a function of temperature. (b) Schematic illustration showing electrical connection (FIBID) between heated platform tip – side platform tip and opposite platform tip – side platform tip.

2.5 Summary and Conclusion

The testbench has been designed and fabricated to measure thermal and thermoelectric properties of low-dimensional materials. It is composed of 52 closely placed thermally isolated platform tips which are located in central area for enhancing the probability of landing a single test-material between two neighboring platform tips.

After fabrication, we have performed the electrical and thermal characterization of the testbench. Both heater and thermocouple show ohmic behavior and the leakage between heater and thermocouple or heater and platinum pad is small enough not to affect the measurement. By the thermal characterization, it was found that the thermal cross-talk between two neighboring platform tips is decreased by a factor of 38 by releasing the tips of the platforms from the substrate, and the thermocouple voltage starts to roll down due to thermal time constant when frequency of heating voltage is above 100 Hz. Most importantly, the polysilicon-gold thermocouple was successfully calibrated at temperatures between 300 and 15 K.

The measurement method for electrical conductivity, thermal conductivity, and Seebeck coefficient has been explained in the last part of the chapter. The measurement using testbench provide following five values: heating power, temperature rise of heated and opposite platform tips, thermoelectric voltage between two platinum pads, and electrical resistance between two platinum pads. The thermal conductivity is obtained from heating power and temperature rise of both platform tips using equivalent thermal circuit and COMSOL FEM. The Seebeck coefficient is calculated from thermoelectric voltage between two platinum pads and temperature rise of both platform tips. The resistance between two platinum pads provides electrical conductivity.

Reference

[1] A. Boukai, K. Xu, and J. R. Heath, "Size-dependent transport and thermoelectric properties of individual polycrystalline bismuth nanowires," *Advanced Materials,* vol. 18, pp. 864-869, 2006.

[2] A. I. Boukai, Y. Bunimovich, J. Tahir-Kheli, J. K. Yu, W. A. Goddard Iii, and J. R. Heath, "Silicon nanowires as efficient thermoelectric materials," *Nature,* vol. 451, pp. 168-171, 2008.

[3] P. Kim, L. Shi, A. Majumdar, and P. McEuen, "Thermal transport measurements of individual multiwalled nanotubes," *Physical review letters,* vol. 87, p. 215502, 2001.

[4] L. Shi, D. Li, C. Yu, W. Jang, D. Kim, Z. Yao, P. Kim, and A. Majumdar, "Measuring thermal and thermoelectric properties of one-dimensional nanostructures using a microfabricated device," *Journal of heat transfer,* vol. 125, pp. 881-888, 2003.

[5] J. Zhou, C. Jin, J. H. Seol, X. Li, and L. Shi, "Thermoelectric properties of individual electrodeposited bismuth telluride nanowires," *Applied Physics Letters,* vol. 87, pp. 133109-133109-3, 2005.

[6] A. I. Hochbaum, R. Chen, R. D. Delgado, W. Liang, E. C. Garnett, M. Najarian, A. Majumdar, and P. Yang, "Enhanced thermoelectric performance of rough silicon nanowires," *Nature,* vol. 451, pp. 163-167, 2008.

[7] C. Kittel and P. McEuen, *Introduction to solid state physics* vol. 8: Wiley New York, 1976.

[8] M. A. Panzer, M. Shandalov, J. A. Rowlette, Y. Oshima, Y. W. Chen, P. C. McIntyre, and K. E. Goodson, "Thermal properties of ultrathin hafnium oxide gate dielectric films," *Electron Device Letters, IEEE,* vol. 30, pp. 1269-1271, 2009.

[9] Y. Sungtaek Ju, X. REN, W. XIAO, N. Smith, R. Fontana, W. Lee, K. Carey, M. Ho, D. Hsiao, and B. Gurney, "A combined experimental and numerical study of temperature rise in GMR sensors due to self-heating," *IEEE transactions on magnetics,* vol. 37, pp. 1701-1703, 2001.

[10] C. H. Mastrangelo, Y.-C. Tai, and R. S. Muller, "Thermophysical properties of low-residual stress, silicon-rich, LPCVD silicon nitride films," *Sensors and Actuators A: Physical,* vol. 23, pp. 856-860, 1990.

[11] M. B. Kleiner, S. A. Kuhn, and W. Weber, "Thermal conductivity measurements of thin silicon dioxide films in integrated circuits," *Electron Devices, IEEE Transactions on,* vol. 43, pp. 1602-1609, 1996.

[12] A. D. McConnell, S. Uma, and K. E. Goodson, "Thermal conductivity of doped polysilicon layers," *Microelectromechanical Systems, Journal of,* vol. 10, pp. 360-369, 2001.

[13] R. Huebener, "Size effect on phonon drag in platinum," *Physical Review,* vol. 140, p. A1834, 1965.

[14] H. Wiebking, "THERMOPOWER OF QUENCHED METAL FILMS," *Z PHYSIK,* vol. 232, pp. 126-138, 1970.

[15] H. Sugawara, T. Nagano, K. Uozumi, and A. Kinbara, "Electrical and thermoelectric properties of evaporated copper films," *Thin Solid Films,* vol. 14, pp. 349-365, 1972.

Appendix C

Detail on Fabrication Process

Polysilicon layer

1) Cleaning

① Soak a wafer (poly-Si/Si_3N_4/SiO_2/Si_3N_4/Si substrate) in Piranha (H_2SO_4:H_2O_2 = 3:1) for 10 secs and rinse it with deionized (DI) water.

② Etch native oxide using 10:1 BOE (buffered oxide etch) for 10 secs and rinse the wafer with DI water

③ Clean the wafer with acetone, isopropyl alcohol (IPA), and DI water, sequentially.

2) Spin-coating and soft baking

① Spin-coat HMDS at 500 rpm (100 rpm/sec acceleration) for 5 secs, followed by 4000 rpm (1000 rpm/sec acceleration) for 40 secs. The spin rate and time will be same for other spin-coating processes if not mentioned differently.

② Spin-coat SPR 3012 and rub edge with swab soaked in EBR PG (MicroChem) to remove edge bead.

③ Bake the wafer on 95 °C hot plate for 1 min.

3) Exposure and developing

① Perform UV exposure for 7.8 secs (intensity: 6.2 mW/cm^2) with photomask named "Poly" in "EVG 620 mask aligner". "Vac+Hard Contact" mode is used with Hard-cont. pressure of 0.4 bar, WEC pressure of 0.5 bar, EXP pressure of 1.1 bar, and Chuck pressure of 290 mbar. Contact mode and pressure will be same for all photolithography performed for this device.

② Develop with MSCD26 for 65 secs.

4) Etching polysilicon

① Etch polysilicon using "HAR LF" process in "Alcatel AMS-100 deep reactive ion etcher (Silicon)" for 1 min and 20 secs. The flow rate of gas and power are listed in Table C-1.

Gas	Flow rate (sccm)
O_2	100
Ar	200
C_4F_8	100
SF_6	100

	Power (W)	Load	Tune
SH1	2000	800	600
SH2	500	800	600

Table C-1. Process condition for etching polysilicon or silicon in "Alcatel AMS-100 deep reactive ion etcher (Silicon)".

Au layer and ALD layer

1) Cleaning

① Soak the wafer in Remover PG on 60 °C hot plate for 1 hr in order to remove photoresist. And clean it with IPA and DI water.

2) Spin-coating and soft baking

① Spin-coat HMDS and LOR5A (lift-off resist), sequentially. Remove edge bead and bake the wafer on 180 °C hot plate for 5 mins.

② Spin-coat SPR 3012. Remove edge bead and bake the wafer on 95 °C hot plate for 1 min.

3) Exposure and developing

① Preform alignment and UV exposure for 7 secs (intensity: 6.2 mW/cm^2) with photomask named "Au" in "EVG 620 mask aligner". The exposure time is a little shorter compared to polysilicon layer because the develop time needs to be longer due to LOR5A.

② Develop with MSCD26 for 100 secs.

4) Descumming and etching native oxide

① Perform descumming for 1 min and 10 secs in "Alcatel AMS-100 reactive ion etcher (Oxide)" to remove photoresist residue on the surface where the photoresist was developed. The flow rate of gas and power are listed in Table C-2.

Gas	Flow rate (sccm)
O_2	50

	Power (W)	Load	Tune
Source	500	756	773
SH	100	808	544

Table C-2. Process condition for descumming in "Alcatel AMS-100 reactive ion etcher (Oxide)".

② Soak the wafer in 10:1 BOE for 40 secs to etch native oxide on polysilicon. Perform it right before the following metalization.

5) Metalization and lift-off

① E-beam evaporate Ti/Au (20 nm/350 nm) in "Semicore e-gun thermal evaporator".

② Soak the wafer in Remover PG on 60 °C hot plate for 12 hrs.

6) ALD

① Deposit Al_2O_3/HfO_2 (20 nm/30 nm) at 200 °C in "Cambridge System (Savannah 200)".

Pt/Ni layer

1) Spin-coating and soft baking

① Spin-coat HMDS and LOR5A (lift-off resist), sequentially. Remove edge bead and bake the wafer on 180 °C hot plate for 5 mins.

② Spin-coat SPR 3012. Remove edge bead and bake the wafer on 95 °C hot plate for 1 min.

2) Exposure and developing

① Perform alignment and UV Exposure for 4 secs (intensity: 6.2 mW/cm^2) with photomask named "Pt/Ni" in "EVG 620 mask aligner". The exposure time is reduced compared to polysilicon & Au layer in order to prevent narrow line pattern between platforms from collapsing during developing process.

② Develop with MSCD26 for 80 secs.

3) Descumming, metallization, and lift-off

① Perform descumming for 3 mins in "Alcatel AMS-100 reactive ion etcher (Oxide)".

② E-beam evaporate Ti/Pt/Ni (30 nm/100 nm/150 nm) in "Semicore e-gun thermal evaporator". Cool down system for 10 mins after depositing 50 nm of Pt for preventing photoresist burning.

③ Soak the wafer in Remover PG on 60 °C hot plate for 12 hrs.

Trench etch

1) Spin-coating and soft baking

① Spin-coat HMDS and Shipley 1827, sequentially. For Shipley 1827, do it at 2500 rpm instead of 4000 rpm. Remove edge bead and bake the wafer on 110 °C hot plate for 80 secs.

2) Exposure and developing

① Perform alignment and UV exposure for 7.8 secs (intensity: 6.2 mW/cm^2) with photomask named "Release redone" in "EVG 620 mask aligner"

② Develop with AZ351:DI water (1:3) for 65 secs.

③ Bake the wafer on 120 °C hot plate for 8 mins.

3) Etching ALD

① Etch ALD layer for 1 min and 15 secs in “Alcatel AMS-100 reactive ion etcher (Oxide)”. The flow rate of gas and power are listed in Table C-3.

Gas	Flow rate (sccm)
O_2	5
Ar	45
C_4F_8	0
SF_6	10

	Power (W)	Load	Tune
Source	800	863	648
SH	150	115	687

Table C-3. Process condition for etching ALD, silicon oxide, and silicon nitride in “Alcatel AMS-100 reactive ion etcher (Oxide)”.

② Perform oxygen plasma cleaning for 5 mins in “Alcatel AMS-100 reactive ion etcher (Oxide)”.

4) Etching stress-compensated stack

① Repeat steps 1), 2), and 3) 3 times except that photomask is changed to “Release” and etching time is 2 mins 30 secs for each repeat.

5) Etching silicon substrate

① Repeat steps 1), 2), and 3) except that photomask named “Release” is used and etching is performed for 5 mins and 40 secs in “Alcatel AMS-100 deep reactive ion etcher (Silicon)”.

Final Process

1) Dicing

① Spin-coat Shipley 1827 and bake the wafer for 60 secs in order to protect the device during dicing process.

② Perform dicing. The following steps are performed by the chip.

2) Cleaning

① Soak the chip in Remover PG on 60 °C hot plate for 30 mins in order to remove photoresist. And clean it with IPA and DI water.

② Perform oxygen plasma cleaning for 5 mins in "M4L RF gas plasma system". The flow rate of gas and power are listed in Table C-4.

Gas	Flow rate (sccm)	Regulator (sccm)	Power (W)
He	50	1000	350
C_4F_8	300		

Table C-4. Process condition for oxygen plasma cleaning in in "M4L RF gas plasma system".

3) Isotropic trench etch

① Perform 10 cycles of XeF_2 etching in "Xactix XeF_2". The etching condition is listed in Table C-5.

Gas	Pressure (Torr)	Cycles	Etch time
XeF_2	2.0	10	60 secs/cycles
N_2	0		

Table C-5. Process condition for isotropic trench etch in "Xactix XeF_2".

4) Wet etching Ni

① Soak the chip in Nickel Etchant Type I on 40 °C hot plate for 3 mins and rinse it with DI water.

5) Drop-casting test-materials from solution

6) FIBID or EBID of Pt

① Perform FIBID or EBID of Pt in "FEI Company Quanta 200 3D Dual Beam FIB". The deposition time needs to be determined after test because the deposition rate varies by many conditions such as position of gas injection needle tip. In good condition, the deposition rate of FIBID (EBID) is approximately 50 nm/min (10 nm/min) for 1 μm^2-sized window with process condition listed in Table C-6.

Type	Voltage (kV)	Current	Dwell time
FIBID	30	1.0 pA	3 μs
EBID	5	0.67 nA	1.4 ms

Table C-6. Process condition for FIBID and EBID of Pt in "FEI Company Quanta 200 3D Dual Beam FIB".

Chapter 3

Thermoelectric Properties of Nanocrystalline Bismuth Telluride Nanotubes

3.1 Introduction

Nanostructured bulk materials, such as nanocrystalline materials and nanocomposites, have been recently researched because they offers suppressed lattice thermal conductivity caused by phonon-boundary scattering at interfaces between crystalline domains or different materials [1-3]. And interfaces can also act as potential barrier for charge carrier which result in suppressed bipolar (electron-hole pairs) thermal conductivity [2] or enhanced Seebeck coefficient [4, 5]. Low-dimensional materials also have attracted great attention due to the suppressed lattice thermal conductivity [6] and potential for enhancement in power factor, as mentioned in Chapter 1. However, in case of bismuth telluride, there has not been any experimental report that *ZT* of low-dimensional materials is comparable to or larger than that of bulk because of unexpected small Seebeck coefficient. The unintentional doping caused by impurity prevented the electrodeposited nanowires having Seebeck coefficient that is comparable to optimally doped bulk [7, 8]. The nanoplates synthesized by vapor-solid growth method also showed small Seebeck coefficient due to surface band bending [9]. In this chapter, we present on thermal and thermoelectric properties of individual nanocrystalline bismuth telluride nanotubes. And we report for the first time that *ZT* of low-dimensional bismuth telluride is larger than that of bulk near room temperature. The bismuth telluride nanotubes used in this work were synthesized by Prof. Xiaoguang group at University of Science and Technology of China and obtained from Prof. Li group at The Pennsylvania State University through a collaborative arrangement. TEMs of the nanotubes were performed by S. Yu in Prof. Mohney group at The Pennsylvania State University.

3.2 Nanotube Synthesis and Structure

The nanotubes were grown by ethylene glycol mediated solution phase method. The detailed procedure for the synthesis has been described in Reference [10]. Here, it is only briefly described. First, single crystalline Te nanowires were obtained by reducing TeO_2 dissolved in ethylene glycol through $N_2H_4 \cdot H_2O$. Afterward, the Bi precursor solution was added to transform the Te nanowire into bismuth telluride nanotube through nanoscale Kirkendall effect. The energy dispersive X-ray spectrum analysis revealed that the nanotubes have near-stoichiometric Bi/Te atomic ratio (Bi_2Te_3) [10]. Figures 3-1 and 3-2 present scanning electron microscope (SEM) and transmission electron microscope (TEM) images of nanotubes, respectively. The diameter and the wall thickness range from 100 to 200 nm and from 10 to 15 nm, respectively. And the wall is formed through continuous connection of nanosized (~50 nm) crystalline domains and (003) plane of each domain is at the angle of 0-15 ° with the axial direction of nanotube. Because the nanotubes exhibits crystalline morphology and have thin walls, they are expected to have properties of both nanostructured bulk materials as well as those of low-dimensional materials.

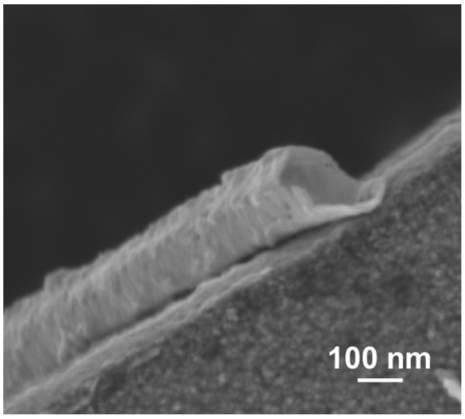

Figure 3-1. SEM (LEO 1530 FESEM at 2 kV) image of Bi_2Te_3 nanotube.

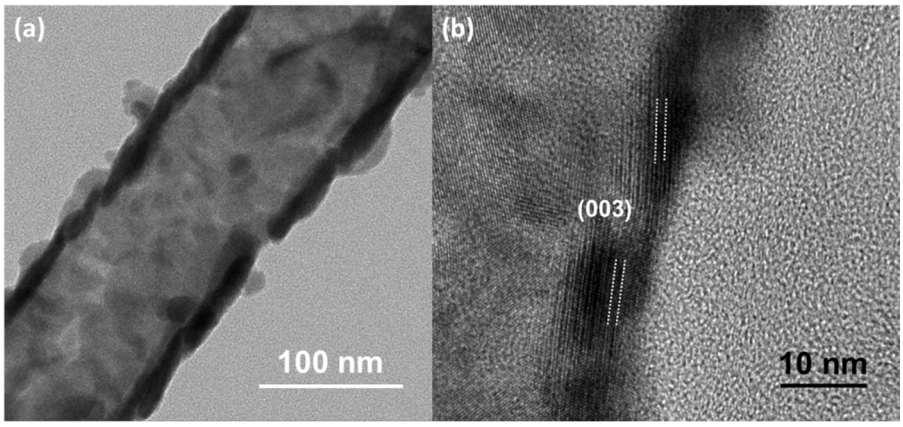

Figure 3-2. TEM images of Bi_2Te_3 nanotube.

3.3 Power Factor

3.3.1 Fabrication and Measurement

The Bi_2Te_3 nanotubes were separated from original reaction solution and dispersed into isopropanol alcohol (IPA). Thereafter, 2 µl of the solution was pipetted on to the central region of the testbench chip and allowed to evaporate at room temperature. After this drop-cast process, platform tips likely having the nanotubes were identified under an optical microscope at 1000x magnification. If no useful sample was identified, the process of drop-casting is repeated. The 100-200 nm tube size is large enough to faintly be observable under optical microscope. The chip containing potential nanotube samples was placed inside the dual-beam (electron and ion beams) system and imaged to clearly isolate the useful devices. Electron beam induced deposition (EBID) of platinum was performed to provide mechanical anchors and good electrical and thermal contact between the nanotube and the platinum pads on the testbench at the two ends of the nanotube as shown in Figure 3-3(a). Only a small amount of platinum (< 10 nm) was deposited to prevent its spread beyond desired clamping area so as to affect the nanotubes during measurement. The samples were named as “tb2p-x”, where tb and 2p stand for testbench and

two-probe, respectively. Measurement of the two-probe resistance of the nanotubes following the deposition of the platinum end clamps showed that the resistance of nanotubes varied considerably from sample to sample (25-200 kΩ), which was indicative of significant contact resistance between the nanotubes and the platinum pad. For minimizing the contact resistance, a rapid thermal anneal (RTA) process step was performed in 1 atm forming gas (4 % H_2/96 % N_2) ambient at 200 °C. After 10 minutes of RTA, resistance of most nanotubes reduced to around 25 kΩ. The two-probe resistance did not show any significant decrease by further RTA. Figure 3-3(b) shows the two-probe resistance and its dependence on RTA time; all performed at 200 °C. This can be interpreted as the contact resistance being reduced to a small enough value when compared to the resistance of nanotube that no further improvement can be seen by further annealing.

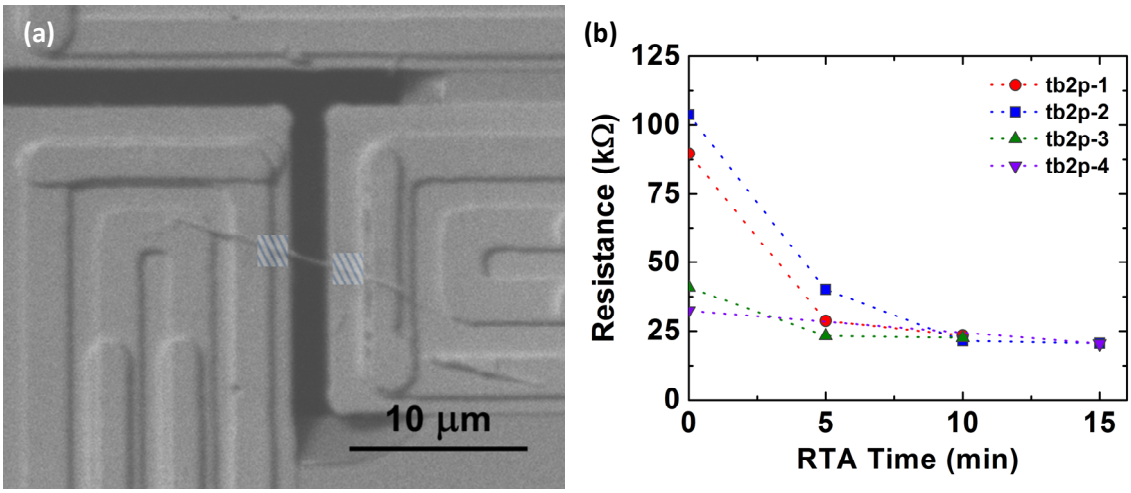

Figure 3-3. (a) SEM image of testbench on which individual nanotube is anchored using EBID of platinum (tb2p-2). The shaded regions are the area on which EBID platinum was deposited. (b) Resistance of nanotubes as a function of RTA time.

In order to measure the Seebeck coefficient and the electrical conductivity of the nanotubes as a function of temperature, the sample was placed in a vacuum cryostat with pressure

below 5×10^{-6} Torr. A sinusoidal voltage with a frequency of 12 Hz ($\omega = (2\pi \times 12)$ rad/s) was applied to the polysilicon heater on one platform tip using Keithley 3390 function generator. This produces a temperature fluctuation at the platform tip at a frequency of 2ω. The temperature rise of the heated and the opposite platform tips was obtained by measuring the 2ω voltage of the polysilicon-gold thermocouple using SR 830 lock-in amplifier. The 2ω voltage between the two platinum pads on the heated and opposite platform tips, which is the thermoelectric voltage induced in nanotube-platinum thermoelectric circuit, was also measured using a lock-in amplifier. The amount of heat dissipated in the heater (heating power) was obtained by measuring applied voltage and current to the heater using Keithley 2001 and Keithley 2000 multimeters. Figure 3-4 plots the temperature rise of both platform tips and the 2ω voltage between platinum pads as a function of the power dissipated in the heater on the heated platform tip.

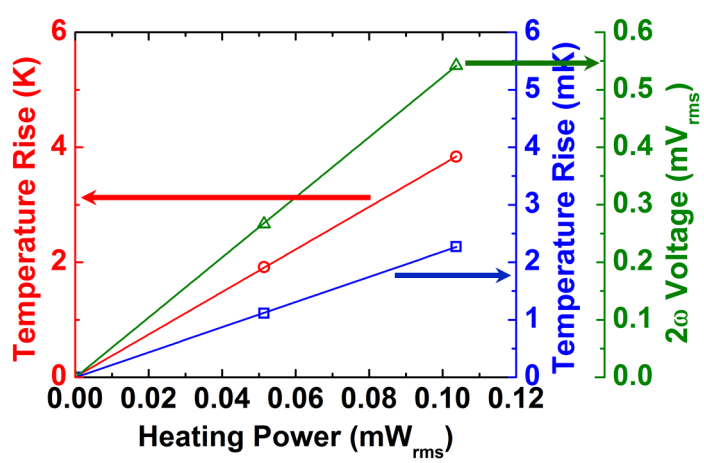

Figure 3-4. Temperature rise of the heated (shown in red/circles) and opposite (shown in blue/squares) platform tips and the 2ω thermoelectric voltage (green/triangles) induced in nanotube-platinum thermoelectric circuit as a function of heating power.

The induced thermoelectric voltage is expressed as

$$V_{TE} = (S_{NT} - S_{Pt})(\Delta T_{HP} - \Delta T_{OP}) \tag{3.1}$$

where S_{NT}, S_{Pt}, ΔT_{HP}, and ΔT_{OP} are the Seebeck coefficient of nanotube, Seebeck coefficient of platinum pad, temperature rise of heated platform tip, and temperature rise of opposite platform tip, respectively. The V_{TE} is equal to 2 times 2ω voltage measured by lock-in amplifier. It is because 2ω voltage has the dc offset that is half of peak-to-peak amplitude as shown in Figure 2-6 and lock-in amplifier detects the amplitude of ac component regardless of input dc offset. S_{Pt} is much smaller than S_{NT}. However, for obtaining more accurate value of S_{NT}, we used reported diffusive Seebeck coefficient of pure platinum, which is −5.6 μV/K at T = 300 K and linearly decreases with decreasing temperature, for S_{Pt} [11] because the phonon-drag effect in evaporated films without being well-annealed is known to be strongly suppressed [12, 13].

Figure 3-5 shows the Seebeck coefficient of 4 samples of Bi_2Te_3 nanotubes plotted as a function of temperature along with the reported value of the Seebeck coefficient of bulk Bi_2Te_3 [14]. Positive sign indicates that holes are the majority carriers. The doping type is consistent with a previous report that bulk bismuth telluride is p-type when the atomic ratio of tellurium is below 63% [15]. The Seebeck coefficient of nanotubes was found to be between 275 and 357 μV/K at T = 300 K which is 11-44 % larger than the reported values for bulk Bi_2Te_3 (248 μV/K) [14].

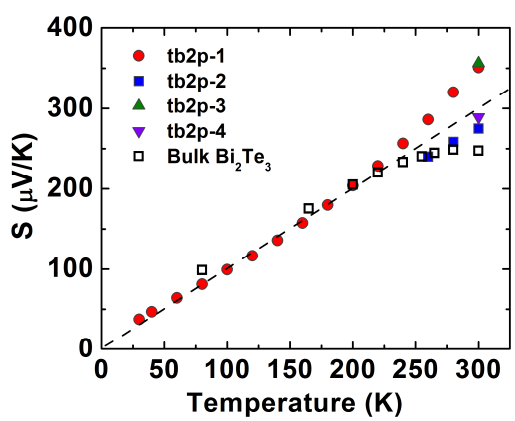

Figure 3-5. Seebeck coefficient of Bi_2Te_3 nanotubes and reported value of bulk Bi_2Te_3 [14] as a function of temperature. The dash line is guideline for eye.

Figures 3-6(a) and (b) show the electrical conductivity and the power factor of Bi_2Te_3 nanotubes as a function of temperature, respectively. The power factor of bulk Bi_2Te_3 has been observed to decrease with increasing temperature because the electrical conductivity decreases rapidly as the temperature increases [14]. However, in case of nanotubes, the power factor was found to increase with temperature primarily because of the electrical conductivity which was found to exhibit minimal dependence on temperature (Figure 3-6(a)). It must be noted that the magnitude of the electrical conductivity of the nanotubes is much smaller than the bulk electrical conductivity value at all temperatures and indicates significantly higher scattering of charge carriers occurring most likely at the surface of the nanotubes. For calculating the electrical conductivity from measured electrical conductance, the diameter of the nanotubes was obtained from SEM images of the particular nanotubes used in measurement. The wall thickness was assumed to be 12.5 nm which is the average of minimum (10 nm) and maximum (15 nm) observed in the TEM images of various nanotubes. These variations give rise to an error ranging from −17 to +25 % in the electrical conductivity and the power factor.

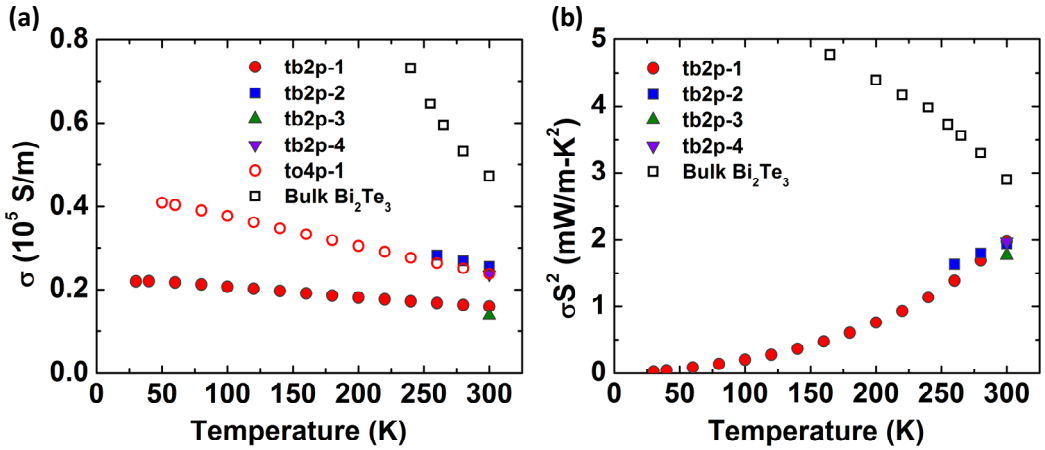

Figure 3-6. (a) Electrical conductivity and (b) power factor of Bi_2Te_3 nanotubes and reported value of bulk Bi_2Te_3 [14] as a function of temperature. to4p-1 is the sample that has four probes and was made to measure thermal conductivity of nanotube using 3ω method. The electrical conductivity obtained from to4p-1 does not include contact resistance.

3.3.2 Theoretical Analysis

The enhancement in Seebeck coefficient is explained by filtering low-energy electrons (minority carriers) at domain boundary. According to two-band conduction model, the Seebeck coefficient is expressed as

$$S = \frac{n\mu_n S_n + p\mu_p S_p}{n\mu_n + p\mu_p} \tag{3.2}$$

where p (n) is hole (electron) concentration, μ_p (μ_n) is hole (electron) mobility, and S_p (S_n) is Seebeck coefficient for hole (electron). In case of p-type material, at low temperatures, n is much smaller than p and it leads S to be almost equivalent to S_p. However, as temperature increases, n increases and S becomes smaller than S_p. This is the reason why S of bulk Bi_2Te_3 starts to saturate at T = ~200 K. However, nanotubes did not show this saturation. It was reported that p-type nanocrystalline BiSbTe has the onset of thermal excitation of electron shifted to higher temperature. This behavior is understood to originate from negatively charged defects, such as Bi_{Te} antisites (Bi atoms occupy Te sublattice sites) or Bi vacancies, in domain boundary which selectively filter low-energy electrons [2, 16]. Since nanotube is p-type nanocrystalline system and consists of bismuth and tellurium, it is reasonable to expect that it contains same type of defects at the boundaries. The negatively charged domain boundaries act as a potential barrier for electrons and the electrons with smaller energy than barrier height are barely able be transport from one domain to neighboring domain. This essentially reduces the effective n contribution to Seebeck coefficient and results in increased S as per Equation (3.2).

In order to quantitatively understand the effect of filtering of low-energy electrons on Seebeck coefficient, Boltzmann equation based on relaxation time approximation was used. According to it, Seebeck coefficient is given by [17, 18]

$$S_{p(n)} = (-)\frac{k_B}{q}\left(\frac{(r+5/2)F_{r+3/2}(\eta_{p(n)})}{(r+3/2)F_{r+1/2}(\eta_{p(n)})} - \eta_{p(n)}\right) \tag{3.3}$$

where k_B is the Boltzmann constant, q is the electric charge of an electron (in absolute value), $\eta_{p(n)}$ is the reduced Fermi energy ($=E_F/k_BT$) with respect to valence (conduction) band edge, and r is the scattering parameter. The scattering parameter of bulk Bi_2Te_3 varies from −½ to 0 at temperatures ranging from 150 and 300 K. It is around –½ at $T = 150$ K and keeps increasing with temperature [19]. It is well known that the carrier concentration is calculated by [17, 18]

$$p(n) = 4\pi\left(\frac{2m^*_{p(n)}k_BT}{h^2}\right)^{3/2} F_{1/2}(\eta_{p(n)}) \tag{3.4}$$

where $m^*_{p(n)}$ is the density of states effective mass of hole (electron). F_j is the complete Fermi-Dirac function given by

$$F_j(\eta_{p(n)}) = \int_0^\infty \frac{x^j dx}{e^{(x-\eta_{p(n)})}+1} \tag{3.5}$$

If a potential barrier for electrons exists at domain boundary, electrons passing over the barrier from a neighboring domain have larger average energy than electrons at thermal equilibrium and the energy distribution of electrons comes back to thermal equilibrium in a length equal to the energy relaxation length from the barrier (Figure 3-7(a)). In the case where the energy relaxation length exceeds domain size, the distribution disturbed at domain boundary does not return to thermal equilibrium inside the domain (Figure 3-7(b)). Based on reported electron mobility (1200 $cm^2V^{-1}s^{-1}$) and energy relaxation time (10 ps) at $T = 300$ K for bulk Bi_2Te_3 [20], the energy relaxation length of electron is estimated to be 176 nm using $l_E = \sqrt{D\tau_E}$, where D is the diffusion coefficient and τ_E is the energy relaxation time. Even using reduced mobility for electrons in nanotube which can be obtained by comparing the electrical conductivity of nanotube to that of bulk (Figure 3-6(a)), is the energy relaxation length $l_E|_{\text{Nanotube}}$ ~125 nm which is still larger than crystalline domain size observed in the TEM images of the nanotubes which is ~50 nm. This

justifies our assumption that only electrons whose energy is above the barrier height are involved in thermoelectric transport. In this case, instead of complete Fermi-Dirac function, we use the incomplete Fermi-Dirac function which is expressed as

$$iF_j(\eta_n) = \int_b^{\infty} \frac{x^j dx}{e^{(x-\eta_n)} + 1} \tag{3.6}$$

where b is barrier height with respect to conduction band edge. For the sake of simplicity, in this derivation, it was assumed that there is no tunneling through the potential barrier.

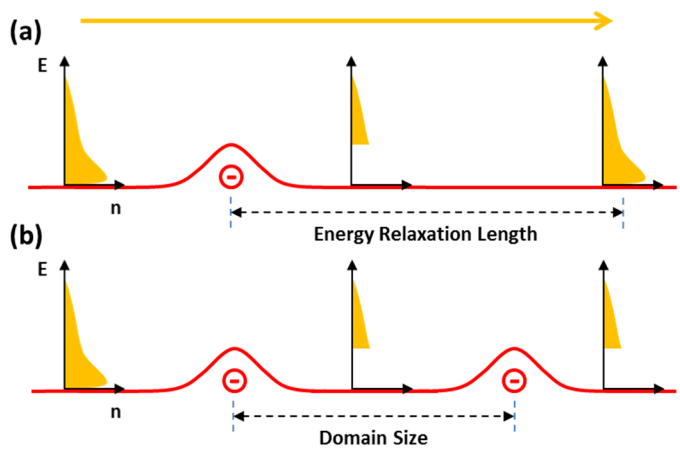

Figure 3-7. Schematic illustration showing energy distribution of electrons near domain boundary in case that domain size is (a) larger or (b) smaller than energy relaxation length. (E: energy of electron, n: electron concentration per unit energy)

Figure 3-8 shows the calculated values of the electrical conductivity and the Seebeck coefficient obtained by using complete Fermi-Dirac function. In these calculations, the doping concentration was adjusted to fit to the experimentally measured bulk electrical conductivity and Seebeck coefficient data for Bi_2Te_3 [14]. A carrier concentration of 5.7×10^{18} cm^{-3} was found to fit well to reported value of bulk electrical conductivity. The dopants were assumed to be fully ionized above 150 K and density of states effective mass, mobility, band gap and their temperature dependence were taken from references as listed in Table 3-1.

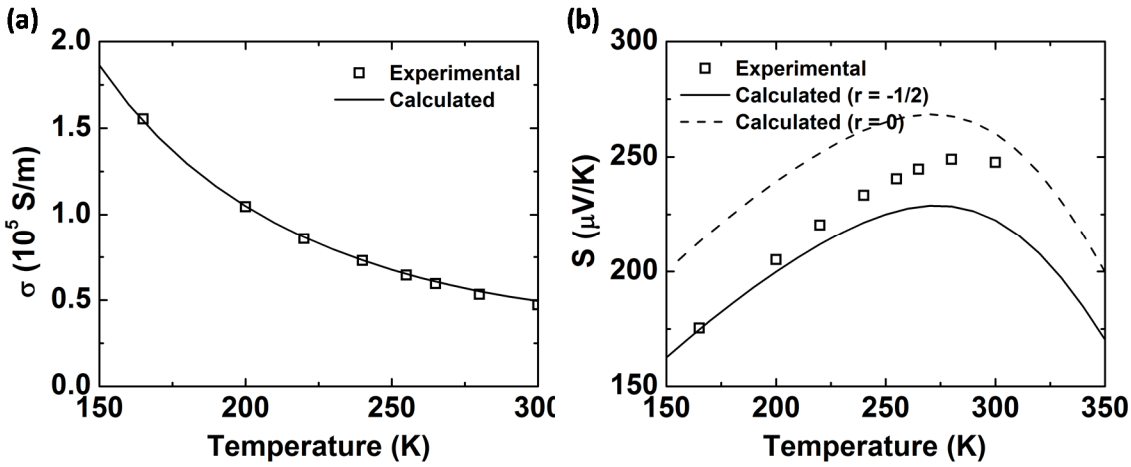

Figure 3-8. Reported (a) electrical conductivity and (b) Seebeck coefficient of bulk Bi_2Te_3 [14] and calculated data. (*r*: scattering parameter)

	T = 300 K		Temperature Dependence	
	Hole	Electron	Hole	Electron
Density of states effective mass	$0.69m_0$ [21]	$0.45m_0$ [21]	$T^{0.17}$ [22]	$T^{0.12}$ [22]
Mobility ($cm^2V^{-1}s^{-1}$)	510 [22]	1200 [22]	$T^{-2.0}$ [22]	$T^{-1.7}$ [22]
Band gap (meV)	$150-0.0947T^2/(T+122.5)$ [22]			

Table 3-1. Properties of bulk Bi_2Te_3 used for calculating electrical conductivity and Seebeck coefficient.

Next, we applied the effect of filtering low-energy electrons at the domain boundary, and recalculated S using n and S_n obtained by incomplete Fermi-Dirac function. The ratio of hole and electron mobility in the nanotubes was assumed to be same with that in bulk. The barrier height was used as fitting parameter and the optimal value was determined to be ~80 meV. The calculated data for S are plotted along with experimental data for Bi_2Te_3 nanotubes in Figure 3-

9(a). For the nanotubes tb2p-2 and tb2p-4, the measured values of S are in good agreement with the calculated data. However, the calculations very poorly model the experimentally obtained S values for nanotubes tb2p-1 and tb2p-3 even if the barrier height is considered to be infinite; i.e. even if S_n is considered to be zero! Considering that the electrical conductivity of tb2p-1 and tb2p-3 nanotubes are significantly smaller than the bulk values as shown in Figure 3-6(a), it is thought that there is disorder in the nanotubes to scatter holes (majority carriers) and it in turn increases Seebeck coefficient. These scattering centers could be present either in the nanotubes or at the contact barrier between nanotube and platinum pad on the testbench. For example, it was observed in the SEM image of tb2p-1 that the middle part of nanotube is unusually wider than the ends as seen in Figure 3-9(b). The holes might be scattered at the transition region from narrow to wide or wide to narrow diameter regions. This disorder seems to have happened either during fabrication or measurement since it has never been observed in TEM images of several nanotubes that were examined as part of this work. The overall impact of the disorder scattering of holes on the power factor is unclear since as discussed earlier, the error of −17 to +25 % due to the estimation of the wall thickness on the overall electrical conductivity of the nanotubes is far more significant.

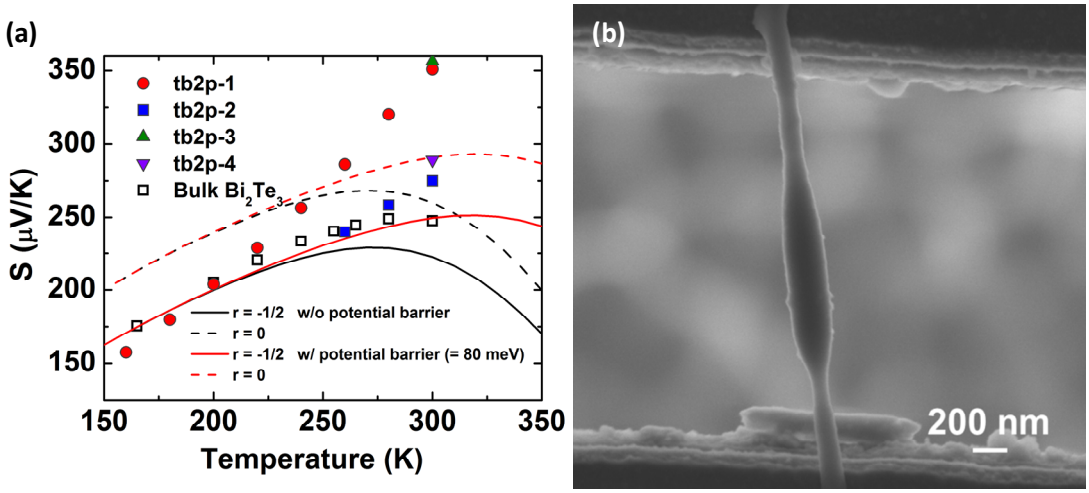

Figure 3-9. (a) Seebeck coefficient of Bi_2Te_3 nanotubes and reported value of bulk Bi_2Te_3 [14] and calculated data at temperatures ranging from 150 to 300 K. (*r*: scattering parameter) (b) SEM (LEO 1530 FESEM at 5 kV) image of suspended part of nanotube in tb2p-1.

3.4 Thermal Conductivity

3.4.1 Fabrication and Measurement

Thermal conductivity of the Bi_2Te_3 nanotubes could not be obtained using the testbench because the thermal conductance of nanotubes was found to be smaller than the parasitic thermal conductance through substrate between neighboring platforms tips (9.7×10^{-9} W/K). Therefore, we used a modified 3ω method, which is based on the 3ω method described by L. Lu et al. [23], and adapted it to nanowire or nanotube measurement. This measurement requires a four-probe configuration and the test-material should be suspended between two inner voltage-sensing probes so that two probes are the only heat sink for the Joule heat produced in the test-material. The 3ω method essentially uses the test-material itself as both a heater and a thermistor. A sinusoidal current with frequency ω results in a temperature fluctuation of the test-material at 2ω by Joule heating, which in turn results in a modulation of the resistance of the nanotube. The 3ω voltage produced by 1ω current and 2ω resistance modulation is related to the thermal

conductivity (efficiency of thermal transport) of the test-material and is given by the expression [23]

$$\kappa = \frac{\sqrt{2} {I_{peak}}^3 R R' L}{\pi^4 V_{3\omega} A \sqrt{1 + (2\omega\gamma)^2}} \tag{3.7}$$

where κ is the thermal conductivity of test-material (nanotube), I_{peak} is the peak value of applied sinusoidal current, R and R' are the resistance of the test-material between voltage-sensing probes and its temperature derivative respectively, L is the length of the test-material between voltage-sensing probes and A is cross-sectional area of test-material. γ is the characteristic thermal time constant of the test-material which is defined by

$$\gamma = \frac{L^2 \rho C_p}{\pi^2 \kappa} \tag{3.8}$$

where ρ is the mass density, C_p is the specific heat.

For using this method, we fabricated a new test device which consists of 40 platinum parallel lines patterned in the central area of chip and connect to individual bonding pad at the end. Each platinum line is 1 μm-wide and separated from each other by 2 μm-wide and 10 μm-deep trenches. First, 300 nm of silicon dioxide was grown on a silicon substrate using thermal oxidation. Chromium (15 nm)/platinum (100 nm)/nickel (150nm) layers were patterned using photolithography and lift-off. This was followed by reactive ion etching of the 300 nm oxide in Alcatel AMS-100 oxide etcher and a deep silicon etch in Alcatel AMS-100 silicon etcher to result in a 10 μm-deep trench between the patterned metal lines and the nickel layer was used as the hard mask for this step. Lastly, the nickel was wet etched. Figure 3-10(a) is the oblique-view SEM image of the device. After fabrication of the device, Bi_2Te_3 nanotubes were drop-casted and clamped electrically and thermally to the platinum lines using EBID and RTA at 200 °C for 15 minutes (Figure 3-10(b)) The samples were named as “to4p-x”, where to and 4p stand for three-omega and four-probe, respectively.

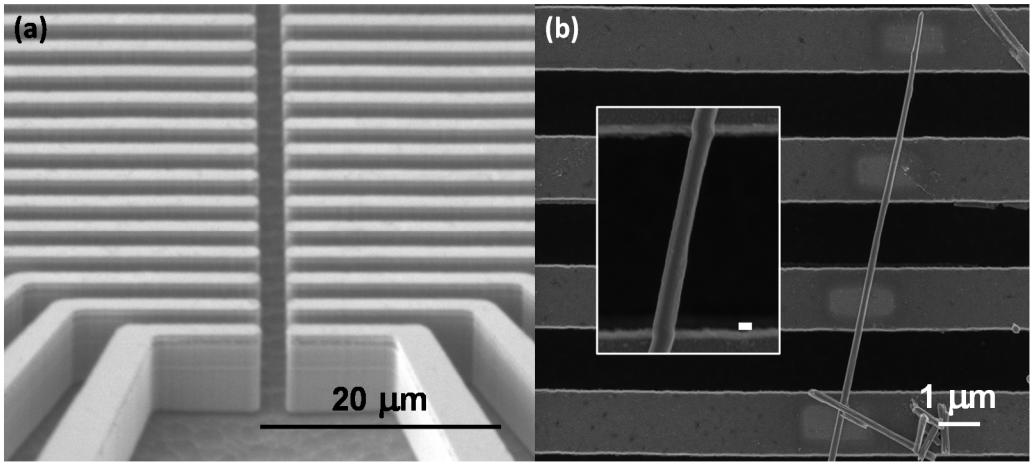

Figure 3-10. (a) Oblique-view SEM image of the device used for 3ω method. (b) SEM (LEO 1530 FESEM at 2 kV) image of the device on which the nanotube is anchored using EBID. The inset is magnified image of suspended part of nanotube between two inner voltage-sensing probes. (The scale bar is 100 nm.)

The device was placed in a vacuum cryostat with pressure below 5×10^{-6} Torr. A sinusoidal current with frequency ω was fed into the nanotube through two outer probes using Keithley 6221 AC and DC current source. And 1ω and 3ω voltage between two inner probes was measured using SR 830 lock-in amplifier as shown in Figure 3-11(a). First, we measured 3ω voltage while varying the frequency from 5 Hz to 26 kHz. Figure 3-11(b) shows the 3 ω voltage as function of frequency. Both the magnitude and the phase (180 °) of the 3ω voltage were found to be constant throughout the measurement frequency range and consistent with the behavior of a low-frequency response of a thermal low-pass filter ($2\omega\gamma \ll 1$). Since the 3dB cut-off frequency was not obtained within the range of the experimentally detectable frequency range of lock-in amplifier, it was not possible to evaluate the specific heat of the nanotubes. The test frequency f was set to at 95 Hz and the 3ω voltage was measured while the current was swept through the range of 1.4-1.8 μA at T = 300 K and 2.0-2.4 μA at T =50 K, and a graph of $V_{3\omega}$ vs I^3 was plotted as shown in Figure 3-11(c). Separately, the resistance of the nanotube was obtained by measuring 1ω voltage for small drive currents (20 nA) so as not to cause significant heating. Figure 3-11(d)

shows the small signal resistance of the Bi_2Te_3 nanotube as a function of temperature. From the slope of 3ω voltage vs. cubic of current and the measured resistance, thermal conductivity of the nanotubes was obtained using Equation (3.7). To cross-check the frequency response, we estimated the 3 dB cut-off frequency of 3ω voltage using Equations (3.7) and (3.8) based on ρ (7530 kg/m^3) and C_{ap} (544 J/kg-K) of bulk bismuth telluride and κ (0.86 W/m-K) and L (1.72 μm) of to4p-1 nanotube. This gives a value of 56 kHz for the 3 dB cut-off frequency which is beyond the maximum detectable frequency in third harmonic of the SR 830 which is 34 kHz.

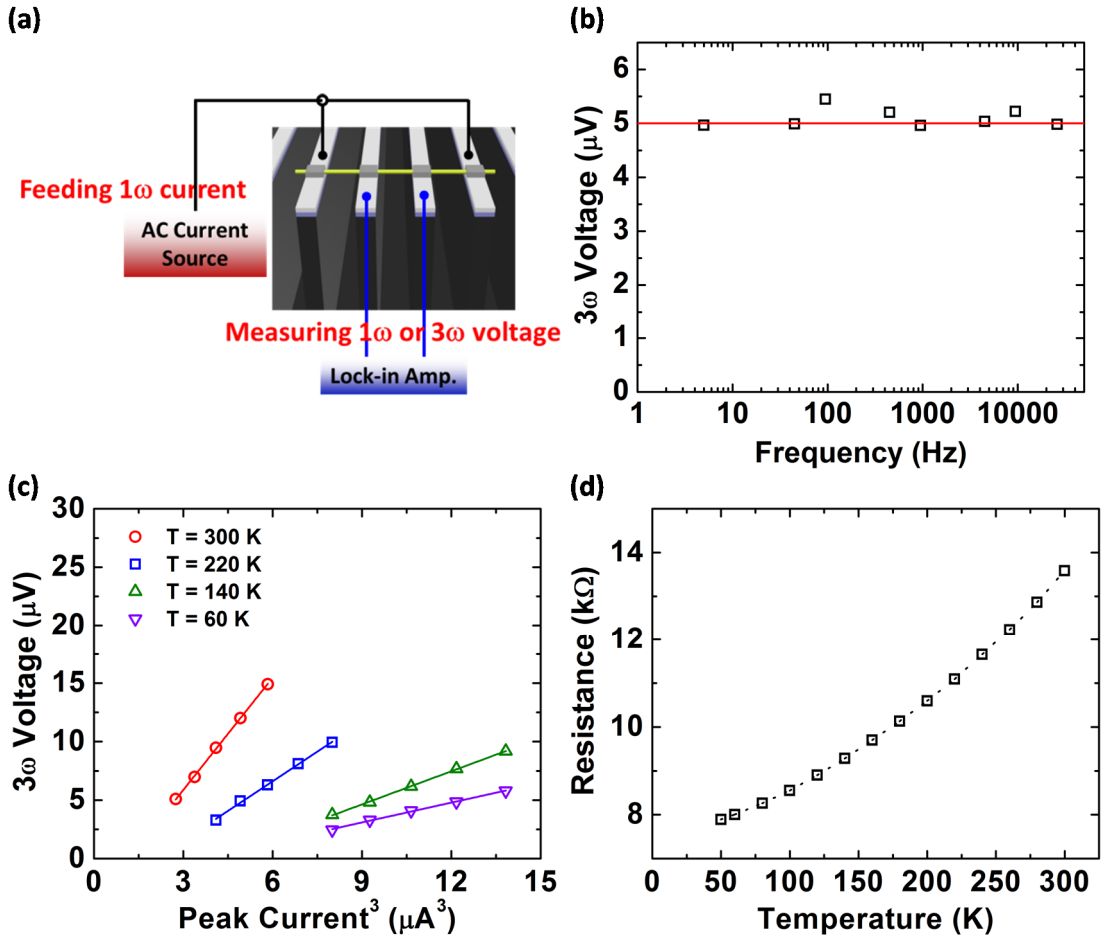

Figure 3-11. (a) Schematic illustration of 3ω method measurement set-up. (b) Frequency dependence of 3ω voltage at T = 300 K. (c) 3ω voltage vs. cubic of current at various temperatures. (d) Resistance of nanotube as a function of temperature.

Figure 3-12 shows thermal conductivity of Bi_2Te_3 nanotube and the reported value of bulk Bi_2Te_3 [14] as a function of temperature. The thermal conductivity of the nanotube is reduced by 64 % as compared to the thermal conductivity of bulk Bi_2Te_3 at $T = 300$ K. This suppression of thermal conductivity further increases with decreasing temperature.

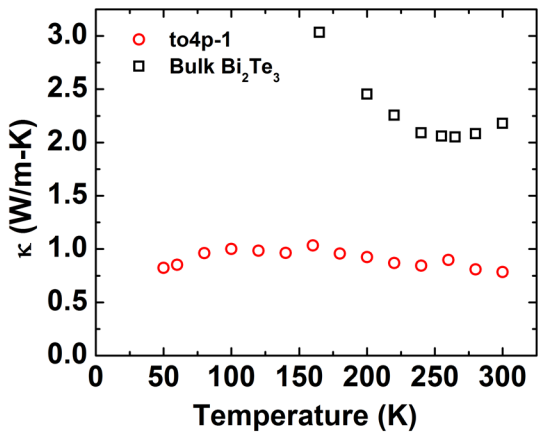

Figure 3-12. Thermal conductivity of Bi_2Te_3 nanotube and reported value of bulk Bi_2Te_3 [14] as a function of temperature.

For providing electrical contact between nanotube and platinum line of the device, we also investigated the use of focused ion beam induced deposition (FIBID) instead of EBID since it is known that FIBID usually gives better electrical contact. However, we noticed considerable difference in the electrical transport behavior of the nanotubes between using EBID and FIBID. The resistance decreased considerably when FIBID is used and showed semiconductor-like behavior (decreasing resistivity with increasing temperature) as shown in Figure 3-13(a). In contrast using EBID, the resistance showed metallic behavior and was more than 4 times higher in value as shown in Figure 3-11(d). It is suspected that the measured lower resistance in the case of FIBID mostly originates from the extended deposition of platinum beyond the patterned region. This was confirmed using TEM imaging of the nanotubes on thin silicon nitride TEM grids which

clearly showed that the platinum spreads out to beyond the desired area during FIBID as shown in the inset of Figure 3-13(a). The resistance of FIBID platinum is known to show semiconductor-like behavior [24]. This further supports the observed characteristics. In this case, the thermal conductance is found to linearly increase with temperature as shown in Figure 3-13(b), which is also different with the case of EBID (Figure 3-12). The resistance and thermal conductance are plotted instead of the electrical and thermal conductivity in this case. It is because we do not know what to assume for the cross-sectional area of the sample due to uneven and unknown amount of FIBID of platinum from sample to sample.

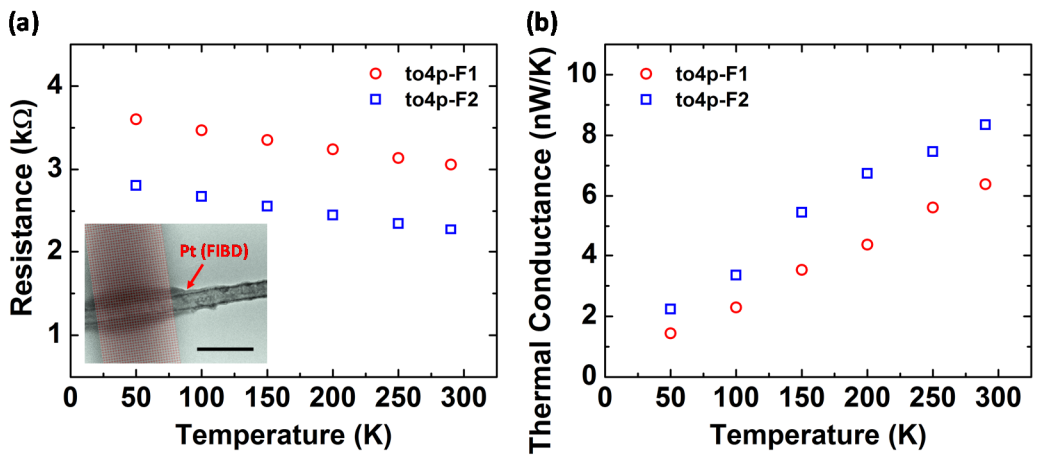

Figure 3-13. (a) Resistance of nanotubes as a function of temperature in case that FIBID was used. The inset is TEM image of nanotube on which FIBID platinum is deposited. The shaded region is the area on which FIBID platinum is intended to be deposited. The scale bar is 500 nm. (b) Thermal conductance of nanotube as a function of temperature in case where FIBID was used.

3.4.2 Theoretical Analysis

In order to understand the reason for suppressed thermal conductivity of nanotube, we theoretically calculated electronic (κ_e), bipolar (κ_b), and lattice thermal conductivity (κ_{ph}) and compared their sum with measured value. The κ_{ph} of nanotube was calculated using Landauer approach [25, 26]. According to Landauer approach, κ_{ph} is calculated by

$$\kappa_{ph} = \frac{\pi^2 {k_B}^2 T}{3h} \langle M_{ph} \rangle \langle\langle \lambda_{ph} \rangle\rangle \tag{3.9}$$

where $<M_{ph}>$ is number of phonon modes that participate in transport and $<<\lambda_{ph}>>$ is average phonon mean free path for backscattering. And $<M_{ph}>$ is given by [25]

$$\langle M_{ph} \rangle \equiv \int_{-\infty}^{+\infty} M_{ph}(\hbar\omega_{ph}) W_{ph}(\hbar\omega_{ph}) d(\hbar\omega_{ph}) \tag{3.10}$$

where M_{ph} is number of phonon subbands crossing phonon energy $\hbar\omega_{ph}$. The complete phonon dispersion curve, which is necessary to compute M_{ph}, was obtained using interatomic pair potential model that B. Qiu et al. reported [27] within General Utility Lattice Program (GULP). Figure 3-14 shows obtained M_{ph} in accordance with phonon energy. Here, we have assumed that the nanotubes have the same phonon dispersion as the bulk material.

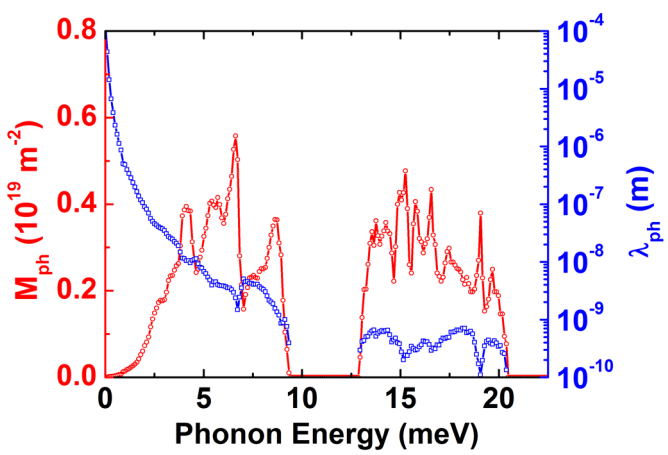

Figure 3-14. The number of phonon subbands and phonon mean free path for backscattering of bulk Bi_2Te_3 at $T = 300$ K.

W_{ph} is "window function" given by [25]

$$W_{ph}(\hbar\omega_{ph}) = \frac{3}{\pi^2} \left(\frac{\hbar\omega_{ph}}{k_B T} \right)^2 \left(-\frac{df_B}{d(\hbar\omega_{ph})} \right) \tag{3.11}$$

where f_B is Bose-Einstein distribution function. The average phonon mean free path for backscattering $<<\lambda_{ph}>>$ is given by [25]

$$\langle\langle\lambda_{ph}\rangle\rangle \equiv \int_{-\infty}^{+\infty} \lambda_{ph}(\hbar\omega_{ph}) M_{ph}(\hbar\omega_{ph}) W_{ph}(\hbar\omega_{ph}) d(\hbar\omega_{ph}) \tag{3.12}$$

$$/ \int_{-\infty}^{+\infty} M_{ph}(\hbar\omega_{ph}) W_{ph}(\hbar\omega_{ph}) d(\hbar\omega_{ph})$$

where λ_{ph} is spectral phonon mean free path and it is equivalent to $(4/3)v_{ph}\tau_{ph}$ in case of three dimensional conductors. v_{ph} is the spectral phonon group velocity. It was obtained from complete phonon dispersion using $\partial\omega_{ph}(k)/\partial k$. τ_{ph} is the phonon momentum relaxation time. It is given by Matthiessen's rule expressing total inverse relaxation time as a sum of inverse relaxation times caused by each scattering mechanism. The expressions used for relaxation time are $\tau_u^{-1}= BT\omega_{ph}^2 e^{-C/T}$ for umklapp scattering, $\tau_i^{-1}=A\omega_{ph}^4$ for impurity scattering and $\tau_i^{-1}= v_{ph}/Fl$ for boundary scattering [28]. We used the constants $A = 1.32 \times 10^{-45}$ s^3, $C = 10$ K, and $Fl = 1 \times 10^{-4}$ m from Reference [25] and $B = 4.0 \times 10^{-18}$ s/K was adjusted to reproduce the experimental lattice thermal conductivity of bulk Bi_2Te_3 [29] and is shown in Figure 3-15. λ_{ph} obtained with this procedure is plotted in Figure 3-14.

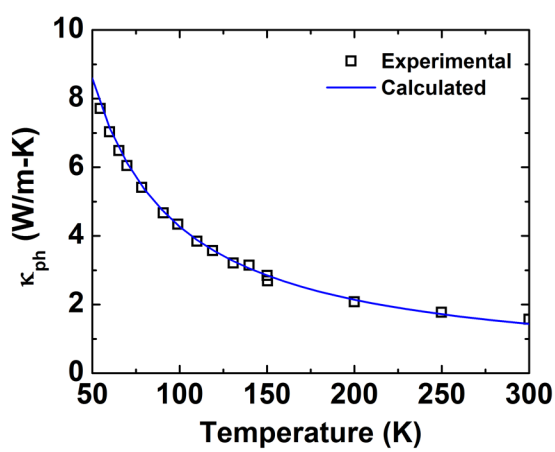

Figure 3-15. The reported lattice thermal conductivity of bulk Bi_2Te_3 [29] and fitted data using Landauer approach as a function of temperature.

In order to predict reduction in phonon mean free path caused by increased scattering of phonon at the surface of nanotube, Fuchs and Sondheimer theory [26, 30, 31] was adopted. According to it, the spectral phonon mean free path for backscattering of thin film (λ_{ph_thin}) can be scaled based on that of bulk (λ_{ph_bulk}) by

$$\lambda_{ph\_thin}(\omega_{ph}) = \lambda_{ph\_bulk}(\omega_{ph})\left[1 - \frac{3(1-p)}{2\delta}\int_1^{\infty}\left(\frac{1}{t^3} - \frac{1}{t^5}\right)\frac{1-e^{-\delta t}}{1-pe^{-\delta t}}dt\right] \quad (3.13)$$

where δ depends on film thickness (t) by $\delta = 4t/3\lambda_{ph\_bulk}$ and p is the specularity parameter which describes the probability that phonon scatters specularly at the surface. Based on the average of minimum (10 nm) and maximum (15 nm) wall thickness observed in TEM images of the nanotubes used in this work, 12.5 nm was used as the film thickness. And the surface scattering was assumed to be diffusive ($p = 0$) in consideration of the rough surface of the nanotubes. Using Equations 3.12 and 3.13, we obtained $<<\lambda_{ph}>>$ of nanotubes. Figure 3-16 plots $<<\lambda_{ph}>>$ of bulk and nanotube as a function of temperature.

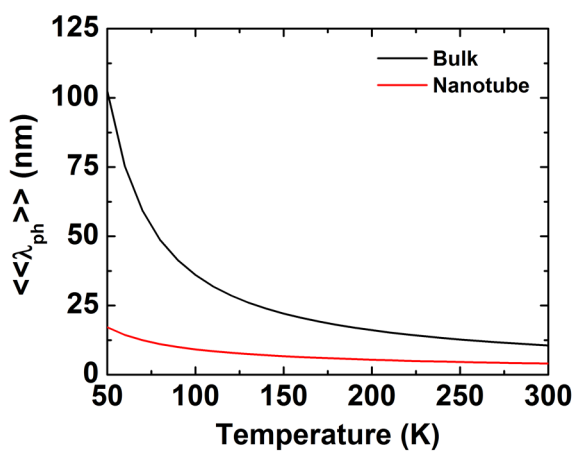

Figure 3-16. Calculated average phonon mean free path.

The dash-dot lines in Figure 3-17 show calculated κ_{ph} of bulk (black) and nanotube (red). The κ_e (dash lines in Figure 3-17) was calculated from electrical conductivity using Wiedemann-

Franz law. The Lorenz number in semiconductor varies by carrier concentration. It is approximately estimated to be 1.5×10^{-8} WΩK^{-2} in non-degenerate semiconductor such as our case whereas it approaches to metallic limit (2.45×10^{-8} WΩK^{-2}) in degenerate semiconductor. The κ_b is expressed by

$$\kappa_b = \frac{\sigma_p \sigma_n}{\sigma_p + \sigma_n}\left(S_p - S_n\right)^2 T \tag{3.14}$$

where σ_p (σ_n) is the electrical conductivity of hole (electron). σ_p and σ_n were obtained by Boltzmann equation based on relaxation time approximation that we had used for calculating

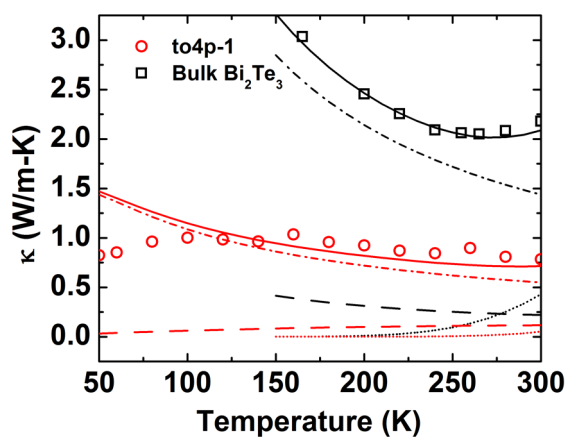

Figure 3-17. Thermal conductivity of Bi_2Te_3 nanotubes and reported value of bulk Bi_2Te_3 [14] as a function of temperature. The red and black represent nanotube and bulk, respectively. The symbols are measured data and the lines are calculated data. (solid lines: total thermal conductivity, dash lines: electronic thermal conductivity, dot lines: bipolar thermal conductivity, dash-dot lines: lattice thermal conductivity)

Seebeck coefficient. The dot lines in Figure 3-17 show calculated bipolar thermal conductivity κ_b of bulk (black) and nanotube (red) Bi_2Te_3. At $T = 300$ K, the values of κ_e and κ_b are 47 and 88 % smaller for the Bi_2Te_3 nanotubes as compared to corresponding bulk values respectively. The suppression of κ_e results from reduced mobility of charge carriers caused by scattering at the surface of nanotube. κ_b is also affected by reduced mobility. However, according to Equation 3.14,

in addition to the reduced 47% mobility effect, κ_b is also suppressed by the filtering effect that shifts the onset of thermal excitation of electrons to higher temperature and can account for the additional suppression beyond that expected due to mobility.

The solid lines in Figure 3-17 are the sum of calculated κ_e, κ_b, and κ_{ph}. In the case of nanotube, above 100 K, calculated data is in good agreement with measured value. There is no additional suppression of κ_{ph} caused by domain boundaries. It is thought to be due to two factors. First, the nanotube has less change in crystal orientation at domain boundary than other nanostructuring processes, such as ball milling followed by hot pressing and melt spinning followed by spark plasma sintering [2, 16, 32]. The *c*-axis of each domain is preferred to be perpendicular to the axial direction of nanotube whereas other processes create randomly oriented domains. Secondly, the phonon mean free path is already significantly reduced by phonon-surface scattering. It decreases the impact of phonon-domain boundary scattering to the reduction of phonon mean free path. However, below 100 K, the measured thermal conductivity decreases slightly with decreasing temperature, and is not consistent with the calculated data. The most possible explanation is that unlike the case at high temperatures the domain boundary might act as an additional scattering factor at low temperatures since the phonon mean free path is larger compared to high temperatures.

3.5 ZT

In this work, we could not measure all the three transport properties on a single nanotube because the thermal conductivity of Bi_2Te_3 nanotubes was much smaller than the parasitic thermal conductance of the testbench. However, to get an accurate estimate of the *ZT* value of the Bi_2Te_3 nanotubes, measurements of the power factor and thermal conductivity was performed on several representative samples to achieve a representative value that is not specific to a given

sample. Therefore, we can still estimate it based on power factor obtained from four testbench samples and thermal conductivity obtained from one 3ω sample. To estimate *ZT* more accurately, once again the uncertainty of the wall thickness needs to be considered. For the nanotubes examined in this work, the wall thickness varied between 10 and 15 nm in TEM images, and therefore we assumed a value of 12.5 nm for calculating electrical and thermal conductivity. Hence, the difference in wall thickness between testbench samples and 3ω sample is an error source. The error will be +50 or −33 % in the extreme case. However, considering electrical conductivity of tb2p-2 at T = 300 K and its change with temperature is only 7.8 % larger and 4.7 % smaller than those of to4p-1, it is reasonable to think that wall thickness of tb2p-2 is close to to4p-1. And Seebeck coefficient of tb2p-4, which is only 5.1 % larger than that of tb2p-2, allows us to think that tb2p-4 does not have the disorder scattering holes and small difference (0.5 % smaller) in electrical conductivity with to4p-1 implies that wall thickness is almost same as to4p-1. If we average the *ZT* of only tb2p-2 and tb2p-4 in consideration of the disorder and uncertainty of wall thickness in tb2p-1 and tb2p-3, the *ZT* of the nanotubes can be estimated to be 0.75 at T = 300 K which is 88 % larger than that of bulk Bi_2Te_3 (0.40).

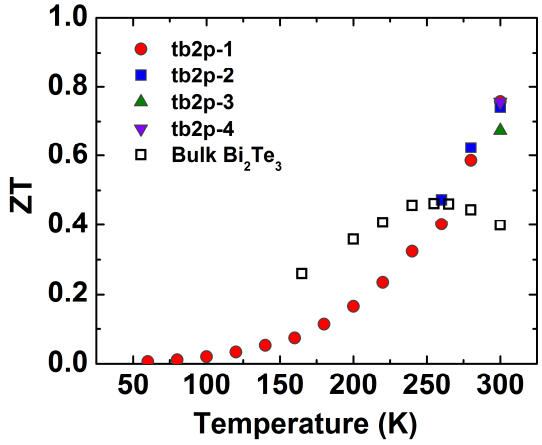

Figure 3-18. *ZT* of Bi_2Te_3 nanotubes and bulk Bi_2Te_3 obtained by Reference [14] as a function of temperature.

3.6 Summary and Conclusion

We have measured thermal and thermoelectric properties of individual nanocrystalline Bi_2Te_3 nanotubes synthesized by solution phase method using microfabricated testbench and 3ω method and it has been revealed that the nanotubes offer improved *ZT* compared to bulk Bi_2Te_3 near room temperature due to enhanced Seebeck coefficient and suppressed thermal conductivity. This improvement in *ZT* originates from nanocrystalline nature and low-dimensionality of nanotube. Domain boundary filtering of low-energy electrons provides enhanced Seebeck coefficient. The scattering of phonon at the surface of nanotube leads to suppressed thermal conductivity. These have been theoretically analyzed using Boltzmann equation based on relaxation time approximation and Landauer approach. This work clearly demonstrates the possibility of achieving enhancement in thermoelectric efficiency by combining nanocrystalline and low-dimensional systems.

Reference

[1] X. Tang, W. Xie, H. Li, W. Zhao, Q. Zhang, and M. Niino, "Preparation and thermoelectric transport properties of high-performance p-type Bi 2 Te 3 with layered nanostructure," *Applied Physics Letters,* vol. 90, pp. 012102-012102-3, 2007.

[2] B. Poudel, Q. Hao, Y. Ma, Y. Lan, A. Minnich, B. Yu, X. Yan, D. Wang, A. Muto, and D. Vashaee, "High-thermoelectric performance of nanostructured bismuth antimony telluride bulk alloys," *science,* vol. 320, pp. 634-638, 2008.

[3] Y. Cao, X. Zhao, T. Zhu, X. Zhang, and J. Tu, "Syntheses and thermoelectric properties of Bi 2 Te 3/Sb 2 Te 3 bulk nanocomposites with laminated nanostructure," *Applied Physics Letters,* vol. 92, pp. 143106-143106-3, 2008.

[4] K. Kishimoto, M. Tsukamoto, and T. Koyanagi, "Temperature dependence of the Seebeck coefficient and the potential barrier scattering of n-type PbTe films prepared on heated glass substrates by rf sputtering," *Journal of Applied Physics,* vol. 92, pp. 5331-5339, 2002.

[5] J. Martin, L. Wang, L. Chen, and G. Nolas, "Enhanced Seebeck coefficient through energy-barrier scattering in PbTe nanocomposites," *Physical Review B,* vol. 79, p. 115311, 2009.

[6] A. I. Hochbaum, R. Chen, R. D. Delgado, W. Liang, E. C. Garnett, M. Najarian, A. Majumdar, and P. Yang, "Enhanced thermoelectric performance of rough silicon nanowires," *Nature,* vol. 451, pp. 163-167, 2008.

[7] J. Zhou, C. Jin, J. H. Seol, X. Li, and L. Shi, "Thermoelectric properties of individual electrodeposited bismuth telluride nanowires," *Applied Physics Letters,* vol. 87, pp. 133109-133109-3, 2005.

[8] E. Menke, M. Brown, Q. Li, J. Hemminger, and R. Penner, "Bismuth telluride (Bi2Te3) nanowires: Synthesis by cyclic electrodeposition/stripping, thinning by electrooxidation, and electrical power generation," *Langmuir,* vol. 22, pp. 10564-10574, 2006.

[9] M. T. Pettes, J. Maassen, I. Jo, M. S. Lundstrom, and L. Shi, "Effects of surface band bending and scattering on thermoelectric transport in suspended bismuth telluride nanoplates," *Nano letters,* vol. 13, pp. 5316-5322, 2013.

[10] G. Zhang, Q. Yu, Z. Yao, and X. Li, "Large scale highly crystalline Bi2Te3 nanotubes through solution phase nanoscale Kirkendall effect fabrication," *Chemical Communications,* pp. 2317-2319, 2009.

[11] R. Huebener, "Size effect on phonon drag in platinum," *Physical Review,* vol. 140, p. A1834, 1965.

[12] H. Wiebking, "THERMOPOWER OF QUENCHED METAL FILMS," *Z PHYSIK,* vol. 232, pp. 126-138, 1970.

[13] H. Sugawara, T. Nagano, K. Uozumi, and A. Kinbara, "Electrical and thermoelectric properties of evaporated copper films," *Thin Solid Films,* vol. 14, pp. 349-365, 1972.

[14] L. Testardi, J. Bierly, and F. Donahoe, "Transport properties of p-type Bi< sub> 2</sub> Te< sub> 3</sub> Sb< sub> 2</sub> Te< sub> 3</sub> alloys in the temperature range 80–370° K," *Journal of Physics and Chemistry of Solids,* vol. 23, pp. 1209-1217, 1962.

[15] J. Fleurial, L. Gailliard, R. Triboulet, H. Scherrer, and S. Scherrer, "Thermal properties of high quality single crystals of bismuth telluride—Part I: Experimental characterization," *Journal of Physics and Chemistry of Solids,* vol. 49, pp. 1237-1247, 1988.

[16] W. Xie, J. He, H. J. Kang, X. Tang, S. Zhu, M. Laver, S. Wang, J. R. Copley, C. M. Brown, and Q. Zhang, "Identifying the specific nanostructures responsible for the high thermoelectric performance of (Bi, Sb) 2Te3 nanocomposites," *Nano letters,* vol. 10, pp. 3283-3289, 2010.

[17] E. Rittner, "On the theory of the Peltier heat pump," *Journal of Applied Physics,* vol. 30, pp. 702-707, 1959.

[18] L. Hicks and M. Dresselhaus, "Effect of quantum-well structures on the thermoelectric figure of merit," *Physical Review B,* vol. 47, p. 12727, 1993.

[19] V. Kulbachinskii, H. Negishi, M. Sasaki, Y. Giman, M. Inoue, P. Lostak, and J. Horak, "Thermoelectric Power and Scattering of Carriers in Bi2—xSnxTe3 with Layered Structure," *physica status solidi (b),* vol. 199, pp. 505-513, 1997.

[20] L. W. da Silva and M. Kaviany, "Micro-thermoelectric cooler: interfacial effects on thermal and electrical transport," *International Journal of Heat and Mass Transfer,* vol. 47, pp. 2417-2435, 2004.

[21] B. Gol'tsman, V. Kudinov, and I. Smirnov, "Semiconducting thermoelectric materials based on Bi2Te3," *Nauka, Moscow,* vol. 14, pp. 320-322, 1972.

[22] I. Bejenari and V. Kantser, "Thermoelectric properties of bismuth telluride nanowires in the constant relaxation-time approximation," *Physical Review B,* vol. 78, p. 115322, 2008.

[23] L. Lu, W. Yi, and D. Zhang, "3ω method for specific heat and thermal conductivity measurements," *Review of Scientific Instruments,* vol. 72, pp. 2996-3003, 2001.

[24] L. Peñate-Quesada, J. Mitra, and P. Dawson, "Non-linear electronic transport in Pt nanowires deposited by focused ion beam," *Nanotechnology,* vol. 18, p. 215203, 2007.

[25] C. Jeong, S. Datta, and M. Lundstrom, "Full dispersion versus Debye model evaluation of lattice thermal conductivity with a Landauer approach," *Journal of Applied Physics,* vol. 109, p. 073718, 2011.

[26] C. Jeong, S. Datta, and M. Lundstrom, "Thermal conductivity of bulk and thin-film silicon: A Landauer approach," *Journal of Applied Physics,* vol. 111, p. 093708, 2012.

[27] B. Qiu and X. Ruan, "Molecular dynamics simulations of lattice thermal conductivity of bismuth telluride using two-body interatomic potentials," *Physical Review B,* vol. 80, p. 165203, 2009.

[28] M. Asen-Palmer, K. Bartkowski, E. Gmelin, M. Cardona, A. Zhernov, A. Inyushkin, A. Taldenkov, V. Ozhogin, K. Itoh, and E. Haller, "Thermal conductivity of germanium crystals with different isotopic compositions," *Physical Review B,* vol. 56, p. 9431, 1997.

[29] P. Walker, "The thermal conductivity and thermoelectric power of bismuth telluride at low temperatures," *Proceedings of the Physical Society,* vol. 76, p. 113, 1960.

[30] K. Fuchs, "The conductivity of thin metallic films according to the electron theory of metals," in *Proc. Cambridge Philos. Soc*, 1938, p. 100.

[31] E. H. Sondheimer, "The mean free path of electrons in metals," *Advances in Physics,* vol. 1, pp. 1-42, 1952.

[32] Y. Ma, Q. Hao, B. Poudel, Y. Lan, B. Yu, D. Wang, G. Chen, and Z. Ren, "Enhanced thermoelectric figure-of-merit in p-type nanostructured bismuth antimony tellurium alloys made from elemental chunks," *Nano letters,* vol. 8, pp. 2580-2584, 2008.

Appendix D

Matlab Code for Calculating Seebeck Coefficient

```
h = 6.62606957e-34 / ( 2 * pi ) ;            % reduced Planck constant (m^2kg/s)
k = 8.6173324e-5 ;                           % Boltzmann constant (eV/K)
e = 1.602176565e-19 ;                        % elementary charge (C)
m = 9.11e-31 ;                               % mass of electron (kg)
po = 5.7e18 ;                                % doping concentration (cm^-3)
barrier = 0.08 ;                             % potential barrier (eV)
r = 0 ;                                      % scattering parameter

for t = 1 : 21
        temp(t) = 350 - 10 * ( t - 1 ) ;             % temperature
        me = 0.45 * ( temp(t) / 300 ) ^ 0.12 * m ;   % density of states effective mass
        mh = 0.69 * ( temp(t) / 300 ) ^ 0.17 * m ;
        muh = 510 * ( temp(t) / 300 ) ^ -2 ;         % mobility (cm^2/V-s)
        mue = 1200 * ( temp(t) / 300 ) ^ -1.7 ;
        Eg = 1e-3 * ( 150 - ( 0.0947 * temp(t) ^ 2 ) / ( temp(t) + 122.5 ) ) ;     % band
gap (eV)

        % obtain Fermi level from doping concentration
        etahmin = - Eg / ( 2 * k * temp(t) ) ;       % min of Fermi level for iteration
        etahmax = 5 ;                                % max of Fermi level for iteration
        imax = 1000 ;
        for i = 1 : imax
                etah(i) = ( etahmax + etahmin ) / 2 ;                % Fermi level wrt VB
                etae(i) = - Eg ./ ( k .* temp(t) ) - etah(i) ;       % Fermi level wrt CB
                FDCH(i) = fermidirac ( 1/2 , etah(i) ) ;             % Fermi-Dirac integral
function % refer to R. Kim and M. Lundstrom, "Notes on Fermi-Dirac Integrals (3rd
Edition)", 2008 (https://nanohub.org/resources/5475)
                FDCE(i) = fermidirac ( 1/2 , etae(i) ) ;
                dh(i) = 1 ./ ( 2 .* pi .^ 2 ) .* ( 2 .* k .* e .* temp(t) ./ h .^ 2 ) .^
( 3 / 2 ) .* mh .^ ( 3 / 2 ) .* FDCH(i) .* 1e-6 ;           % hole concentration
                de(i) = 1 ./ ( 2 .* pi .^ 2 ) .* ( 2 .* k .* e .* temp(t) ./ h .^ 2 ) .^
( 3 / 2 ) .* me .^ ( 3 / 2 ) .* FDCE(i) .* 1e-6 ;           % electron concentration
                err = dh(i) - de(i) - po ;
                if abs ( err ) < ( de(i) * 1e-3 )            % check charge neutrality
                        break ;
                end
                if i == imax
                        error( 'Increase the maximum number of iterations.' )
                end
                if err < 0
                        etahmin  = etah(i) ;
```

```
                end
                if err > 0
                        etahmax  = etah(i) ;
                end
                etahh(t) = etah(i) ;
                etaee(t) = etae(i) ;
                ni(t) = de(i) ;
                hi(t) = dh(i) ;
        end

        IFDCE = incomplete ( 1/2 , etaee(t) , barrier / k / temp(t) ) ;     % incomplete
Fermi-Dirac integral function % refer to M. Goano, "Algorithm 745: computation of the
complete and incomplete Fermi-Dirac integral," ACM Transactions on Mathematical Software
(TOMS), vol. 21, pp. 221-232, 1995
        Ini(t) = 1 ./ ( 2 .* pi .^ 2 ) .* ( 2 .* k .* e .* temp(t) ./ h .^ 2 ) .^ ( 3 /
2 ) .* me .^ ( 3 / 2 ) .* IFDCE .* 1e-6 ;            % electron concentration w/ potential
barrier
        FDAH = fermidirac ( r + 1/2 , etahh(t) ) ;
        FDBH = fermidirac ( r + 3/2 , etahh(t) ) ;
        FDAE = fermidirac ( r + 1/2 , etaee(t) ) ;
        FDBE = fermidirac ( r + 3/2 , etaee(t) ) ;
        IFDAE = incomplete ( r + 1/2 , etaee(t) , barrier / k / temp(t) ) ;
        IFDBE = incomplete ( r + 3/2 , etaee(t) , barrier / k / temp(t) ) ;

        Sh(t) = k .* ( ( r + 5/2 ) .* FDBH ./ ( r + 3/2 ) ./ FDAH - etahh(t) ) ;
        Se(t) = - k .* ( ( r + 5/2 ) .* FDBE ./ ( r +3/2 ) ./ FDAE - etaee(t) ) ;
        S(t) = ( Sh(t) .* hi(t) .* muh + Se(t) .* ni(t) .* mue ) ./ ( hi(t) .* muh +
ni(t) .* mue ) ;              % Seebeck coefficient w/o potential barrier
        Se_b(t) = - k .* ( ( r + 5/2 ) .* IFDBE ./ ( r + 3/2 ) ./ IFDAE - etaee(t) ) ;
        S_b(t) = ( Sh(t) .* hi(t) .* muh + Se_b(t) .* Ini(t) .* mue ) ./ ( hi(t) .* muh +
Ini(t) .* mue ) ;             % Seebeck coefficient w/ potential barrier
        sigma_e(t) = mue .* ni(t) .* e .* 1e2 ;
        sigma_h(t) = muh .* hi(t) .* e .* 1e2 ;
        sigma(t) = sigma_e(t) + sigma_h(t) ;         % electrical conductivity
end

figure(1)
plot ( temp , S , 'r' )
hold on
plot ( temp , S_b , 'b' )
axis ( [ 150 350 1e-4 4e-4 ] )
title ( 'Seebeck Coefficient' )
ylabel ( 'S (V/K)' )
xlabel ( 'Temperature (K)' )
hold off
```

```
figure (2)
plot ( temp , sigma , 'r' )
axis ( [ 150 350 0 2e5 ] )
title ( 'Electrical Conductivity' )
ylabel ( 'sigma (S/m)' )
xlabel ( 'Temperature (K)' )
```

Appendix E

GULP Code for Phonon Dispersion of Bismuth Telluride

```
opti conp prop phon

cell
10.45 10.45 10.45 24.13 24.13 24.13

fractional
Te1 core 0.792 0.792 0.792
Bi core 0.399 0.399 0.399
Te2 core 0.000 0.000 0.000

spacegroup
R -3 M

species
Te1 core -0.26
Bi core 0.38
Te2 core -0.24

Morse 6
Te1 core Bi core 0.975 1.285 3.089 0 0.0 4.0
Te2 core Bi core 0.582 1.257 3.251 0 0.0 4.0
Te1 core Te1 core 0.076 1.675 3.642 0 0.0 5.0
Bi core Bi core 0.085 2.212 4.203 0 0.0 5.5
Te2 core Te2 core 0.066 2.876 4.312 0 0.0 5.0
Te1 core Te2 core 0.807 0.731 4.497 0 0.0 5.5

dispersion 1 250
0.0 0.0 0.0 to -0.5 0.5 0.0

shrink 32 32 32

output phon bi2te3_ph
```

Appendix F

Matlab Code for Calculating Lattice Thermal Conductivity

```
h = 6.5821192815e-16 ;                          % Planck constant (eVs)
k = 8.617332478e-5 ;                            % Boltzmann constant (eV/K)
e = 1.602176565e-19 ;                           % elementary charge (C)

% fitting parameters
l_nano = 12.5e-9 ;
l = 1e-4 ;                                      % Characteristic length of sample (m)
sp = 0 ;                                        % Phonon-surface specularity parameter 1 ->
compeltely specular scattering 0 -> completely diffuse scattering
F = ( 1 + sp ) / ( 1 - sp ) ;
A = 1.32e-45 ;
B = 4e-18 ;
C = 10 ;

load M_ph_bi2te3.mat                            % Array "M_ph" in this file consists of
phonon energy (1st raw), number of phonon subbands crossing phonon energy (2nd raw),
phonon group velocity (3rd raw). % For obtaining this from GULP, refer to C. Jeong,
"Calculating number of modes(transmission) from given E-k dispersion", 2009
https://nanohub.org/resources/7382)

for t = 1 : 26
        temp(t) = 300 - 10 * ( t - 1 ) ;
        E = M_ph(1,:) ;                         % Phonon energy
        nE = length(E) ;
        Mph = M_ph(2,:) ;                       % Number of phonon subbands crossing phonon
energy
        v = M_ph(3,:) ;                         % Phonon group velocity
        dE = [ E(2) - E(1) E(3:nE) - E(1:nE-2) E(nE) - E(nE-1) ] ./ 2 ;

        tb = v ./ l ./ F ;                      % Relaxation time for boundary scattering
        tu = B .* temp(t) .* ( E ./ h ) .^ 2 .* exp( -1 .* C ./ temp(t) ) ;        %
Relaxation time for umklapp scattering
        td = A .* ( E ./ h ) .^ 4 ;             % Relaxation time for impurity scattering
        tau = 1 ./ ( tb + tu + td ) ;

        dfdE = 1 ./ k ./ temp(t) .* exp( E ./ k ./ temp(t) ) ./ ( exp( E ./ k ./ temp(t) )
- 1 ) .^ 2 ;
        Wph = 3 ./ pi .^ 2 .* ( E ./ k ./ temp(t) ) .^ 2 .* dfdE ;  % Window function
        MMph = sum( Mph .* Wph .* dE ) ;        % Number of phonon modes participating in
transport
        Lamda = 4/3 .* v .* tau ;               % Spectral phonon mean free path
```

```
        for n = 1 : 250                        % Fuchs and Sondheimer theory
                if Lamda(n) > 0
                        syms x;
                        delta = 4 / 3 * l_nano / Lamda(n) ;
                        integral = double(int(( 1/x^3 - 1/x^5 ) * ( 1 - exp( -1 * delta *
x )) , x , 1 , inf)) ;
                        Lamda_nano(n) = Lamda(n) * ( 1 - 3 / 2 / delta * integral ) ;
                end

                if Lamda(n) == 0
                        Lamda_nano(n) = 0;
                end
        end
% Average phonon mean free path for backscattering
        LLamda = sum ( Lamda .* Mph .* Wph .* dE ) ./ sum( Mph .* Wph .* dE ) ;
        LLamda_nano = sum ( Lamda_nano .* Mph .* Wph .* dE ) ./ sum( Mph .* Wph .* dE ) ;
        pmp (t) = LLamda ;
        pmp_nano(t) = LLamda_nano ;
% Lattice thermal conductivity
        kph(t) = k .^ 2 .* temp(t) .* pi .^ 2 ./ 3 ./ ( 2 .* pi .* h ) .* MMph .*
LLamda .* e ;
        kph_nano(t) = k .^ 2 .* temp(t) .* pi .^ 2 ./ 3 ./ ( 2 .* pi .* h ) .* MMph .*
LLamda_nano .* e ;
end

figure(1)
plot ( temp , kph_nano , 'r' )
hold on
plot ( temp , kph_nano , 'b' )
axis ( [ 50 350 0 7 ] ) ;
title ( 'Thermal Conductivity' )
ylabel ( 'kai (W/m-K)' )
xlabel ( 'Temperature (K)' )
hold off

figure(2)
plot( temp, pmp , 'r' )
hold on
plot( temp, pmp_nano, 'b' )
title ( 'Phonon mean free path' )
ylabel ( 'MFP (m)' )
xlabel ( 'Temperature (K)' )
hold off
```

Chapter 4

Thermoelectric Properties of Ferromagnetic Nanowires

4.1 Introduction

The electronic transport in nanoscale magnetic systems is of great interest from the perspective of fundamental research because it shows unique properties that are not observed in bulk, such as shape anisotropy. Furthermore, from technical point of view, these materials have the potential to be used for a wide range of applications, such as high-density storage media. For these reasons, the change in the electrical resistance of ferromagnetic low-dimensional materials with applied magnetic field, such as anisotropic magnetoresistance (AMR) and giant magnetoresistance (GMR), has been intensively studied for the past twenty years [1, 2]. Recently, thermoelectric transport in ferromagnetic materials has also gained particular attention after spin current was observed to be generated by a temperature gradient in a ferromagnetic thin film owing to the different Seebeck coefficients of spin-up and spin-down electrons (spin-Seebeck effect) [3]. For further growth in these fields, a thorough understanding of electronic and thermoelectric transport in magnetic systems is necessary. Simultaneous measurement of both the resistance and the Seebeck coefficient of individual ferromagnetic nanowires under the influence of magnetic field is likely to provide a deeper understanding on the relationship between magnetism, electronic transport, and thermoelectric transport. In this chapter, we present the magnetic field dependence of electrical conductivity (resistivity), thermal conductivity and Seebeck coefficient of gallium arsenide (GaAs)/manganese arsenide (MnAs) core/shell nanowires and cobalt (Co) nanowires. The GaAs/MnAs core/shell nanowires and Co nanowires used in this work were synthesized by J. Kally in Prof. Samarth group and Prof. Chan group at The

Pennsylvania State University, respectively. TEMs were performed by S. Yu in Prof. Mohney group at The Pennsylvania State University. The following sections deals with the fundamentals of magnetic materials relevant to this chapter.

4.1.1 Ferromagnetism

Atoms have magnetic moment originating from the spin of electrons (spin angular momentum) and the motion of electrons with respect to its nucleus (orbital angular momentum). If an atom possesses a magnetic moment, it acts as a tiny magnet. In ferromagnetic materials, these magnets spontaneously align themselves and become oriented in the same direction, resulting in the formation of magnetic domains. For the formation of magnetic domains, the atoms require some kind of interatomic force that holds the magnetic moment of many atoms parallel to each other. In the absence of such interactions, thermal energy of the system is likely to align neighboring magnetic dipoles in opposite direction with respect to each other which corresponds to a local potential energy minima of the system and would therefore result in a net zero magnetic moment. In 3d transition metals, such as iron, nickel, and cobalt, main interaction originates from spin angular momentum of partially occupied 3d electrons since the nuclear contribution is negligible. According to the Stoner model [4], it is assumed that an exchange interaction between 3d electrons generates an energy splitting between spin-up and spin-down 3d bands (Figure 4-1). If the orbitals of unpaired electrons from adjacent atoms overlap, they are likely to have spin that is parallel to each other. The electrons with parallel spin are further apart compared to those with antiparallel spin, which reduces the electrostatic energy of electrons and is more stable. Consequently, it produces a difference in the numbers between spin-up and spin-down electrons and gives rise to a spontaneous magnetization. In case that this exchange interaction is much stronger than competing dipole-dipole interaction and thermal agitation, the

material has magnetic domains and becomes ferromagnetic. However, if the exchange interaction is not strong enough, the material becomes paramagnetic. For example, if the temperature of the material is increased to beyond a certain point, called Curie temperature, the material cannot maintain a spontaneous magnetization and undergoes a phase transition from the ferromagnetic phase to paramagnetic phase.

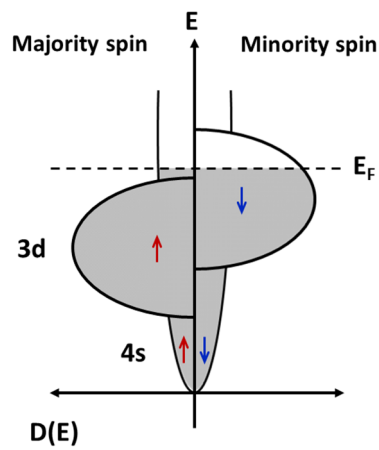

Figure 4-1. Illustration of spin-polarized density of states of a 3d transition metal. The arrow indicates spin-up or spin-down. The shaded area indicates the states filled with electrons.

4.1.2 Anisotropic Magnetoresistance

Ferromagnetic 3d transition metals show anisotropic magnetoresistance (AMR) which describes the dependence of electrical resistance on the angle between the direction of electric current flow and the direction of the magnetization. The origin of AMR is explained well by the two current model proposed by Mott [5, 6]. In 3d transition metals, even though 4s and 3d bands are contributing to the electrical conductivity, 4s electrons carry most of the current because their effective mass is smaller than that of 3d electrons. According to Mott's model, spin-up and spin-down 4s electrons are considered as two separate channels which are connected in parallel. As

discussed previously, exchange interaction splits the 3d band into spin-up and spin-down bands. If it is supposed that spin-up electrons are in majority, as shown in Figure 4-1, then spin-up 3d band has less empty states than spin-down 3d band and the scattering of spin-up 4s electrons into spin-up 3d states would be less than the scattering of spin-down 4s electrons into spin-down 3d states. Therefore, the resistance of spin-up channel is smaller than that of spin-down channel and the spin-up channel carries the most of current. It means that small change in the scattering behavior of spin-up 4s electrons strongly would affect the total resistance. The interaction between spin of electrons and their orbital motion (spin-orbit interaction) can give rise to spin-flip scattering, such as the scattering of spin-up 4s electrons into spin-down 3d states. And the scattering probability depends on the angle between electric current and magnetization. It is maximized when the magnetization is parallel or antiparallel to the electric current, which results in maximum resistance. On the other hand, the resistance is minimized when the magnetization is perpendicular to the electric current.

4.2 Thermoelectric Properties of GaAs/MnAs Core/shell Nanowires

4.2.1 Temperature Dependence

The semiconductor/ferromagnet hybrid structures have gained great attention since they are expected to have a variety of novel properties and can be used for many applications, such as magnetic sensors, magneto-optical devices, and nonvolatile memories [7, 8]. The GaAs/MnAs core/shell nanowires are of particular interest because GaAs is an important semiconductor for optoelectronics and MnAs is ferromagnetic metal whose Curie temperature is above room temperature. It is also a suitable material for investigating magneto-thermoelectric effects, such as magneto-Seebeck, magneto-caloric, and spin-Seebeck effects, in low-dimensional ferromagnetic

systems because of the thin MnAs layer can be obtained in these nanowires. The nanowires were grown on GaAs (111)B substrates in an EPI 930 molecular beam epitaxy (MBE) chamber, using a catalyst-free technique, as detailed in an earlier report [9]. According to TEM analysis, cross-section of nanowires is hexagonal in shape and the longest diagonal of GaAs core and the thickness of MnAs shell are estimated to be 200 nm and 15 nm respectively, as shown in Figure 4-2.

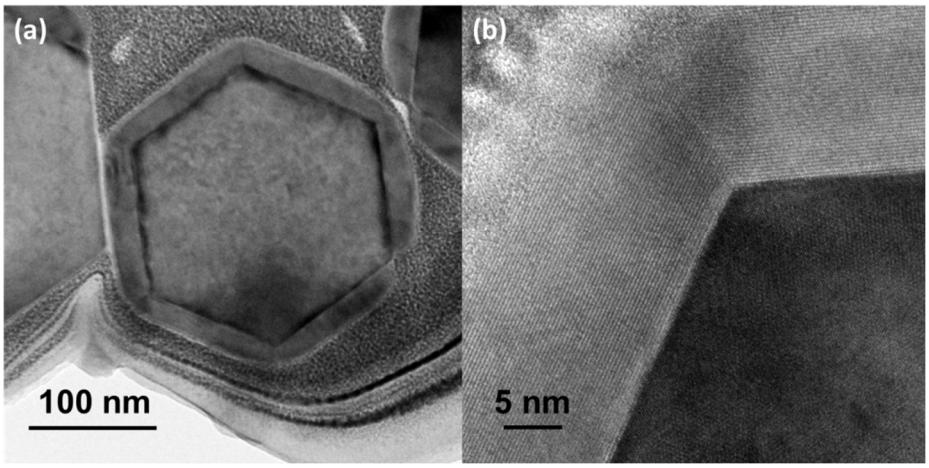

Figure 4-2. (a) Cross-section TEM images of GaAs/MnAs core/shell nanowire. (b) Magnified TEM image of the interface between GaAs and MnAs.

As a preliminary experiment for magnetoresistance and magneto-Seebeck coefficient, we measured electrical conductivity, thermal conductivity and Seebeck coefficient as a function of temperature without applying magnetic field. The nanowires were drop-cast from an IPA solution on the testbench and platinum clamp patches were deposited on the ends of nanowire using focused ion beam induced deposition (FIBID) to make mechanical contact and improve electrical and thermal contact between nanowire and platinum pad of testbench. In this case, electron beam induced deposition (EBID) followed by rapid thermal anneal (RTA) process, which was used for bismuth telluride nanotubes as explained in Chapter 3, was not used because it was found that it

could not provide good enough electrical contact between nanowire and platinum pad due to native oxide on the surface of MnAs shell. Figure 4-3 shows a SEM image of the testbench on which single GaAs/MnAs core/shell nanowire is anchored using FIBID.

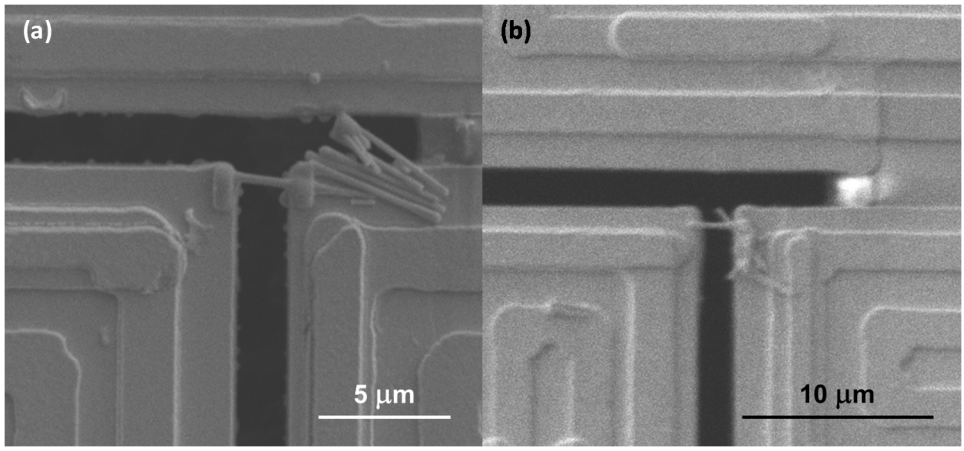

Figure 4-3. SEM images of (a) sample #1 and (b) sample #2.

Thereafter, the sample was placed in a vacuum cryostat with pressure below 5×10^{-6} Torr. We measured the heating power, the temperature of heated and opposite platform tips and thermoelectric voltage induced in nanowire-platinum thermoelectric circuit while applying the heating voltage to the heater. The resistance between two platinum pads was also measured. The measurement was performed at cryostat temperatures ranging from 300 down to 25 K. After the measurement, COMSOL FEM and equivalent thermal circuit modeling were performed to obtain the thermal conductivity from the measured data. The measurement and the process for obtaining the thermal conductivity, Seebeck coefficient, and electrical conductivity from the measured data are explained in more detail in Chapter 2.

Figure 4-4(a) shows the temperature dependence of thermal conductivity of nanowires. In the case of GaAs/MnAs core shell wires, the dominant contribution to the thermal transport in nanowire come from GaAs core because of its large cross-sectional area and lattice thermal

conductivity. The thermal conductivity of the two nanowires investigated in this work is determined to be 7.5 and 8.4 W/m-K at $T = 300$ K. This value is smaller than recently reported theoretical value of 20 W/m-K for 200 nm-diameter GaAs nanowire [10]. Furthermore, the thermal conductivity of the nanowires is found to decrease with decreasing temperature whereas theoretical value has a maximum value near 100 K. However, it must be noted that around 100 K the rate of decrease of thermal conductivity with temperature shows a small slowdown before a final steep decrease beyond 75K. Although GaAs core of the nanowires is single crystalline, it has stacking faults perpendicular to the growth direction as can be seen in Figure 4-2(b). In some regions, the nanowires undergo a transformation in crystal structure from zinc blende with a [111] growth direction to a wurtzite structure with a [0001] growth direction [9]. Such structural boundaries are expected to cause enhanced phonon-boundary scattering and therefore will lead to smaller thermal conductivity. Depending upon the defect density and periodicity, it is even possible that the phonon-boundary scattering is more dominant than the umklapp phonon-phonon scattering processes that are known to increase thermal conductivity with decreasing temperature.

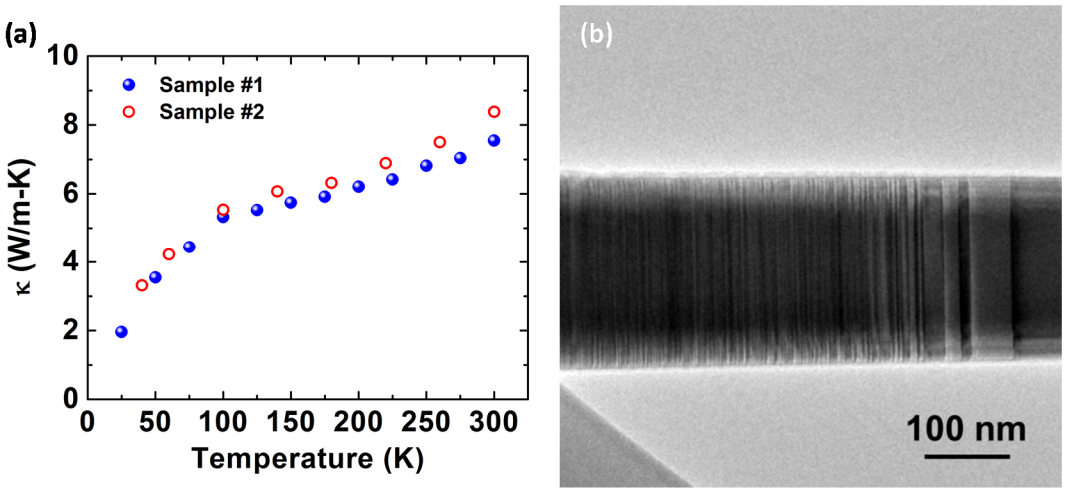

Figure 4-4. (a) Thermal conductivity of GaAs/MnAs core/shell nanowires as a function of temperature (b) A plan-view TEM image of GaAs nanowire showing stacking faults along the growth direction.

Figure 4-5 shows the Seebeck coefficient of a GaAs/MnAs core/shell nanowire as a function of temperature. Because GaAs core is intrinsic, measured Seebeck coefficient and electrical conductance originate from MnAs shell. In the case of sample #2, Seebeck coefficient and electrical conductivity were not obtained because the electrical contact resistance between nanowire and platinum pad was much larger than the resistance of nanowire itself. According to COMSOL FEM, the temperature difference between the two ends of the nanowire is 15.0 % smaller than that between the two thermocouple junctions at the two pad tips at $T = 300$ K. This error was corrected by using Equation (2.16). The absolute Seebeck coefficient of MnAs shell is determined to be -17.2 μV/K at $T = 300$ K which is ~22% larger than previously reported Seebeck coefficient of bulk MnAs (-14 μV/K) [11]. The explanation for the increased Seebeck coefficient may lie in quantum size effect. However, considering that Seebeck coefficient of bulk MnAs has been barely reported, it is too early to draw any firm conclusions in this regards. Furthermore, the absolute value of Seebeck coefficient of the nanowire is found to linearly decrease with decreasing temperature whereas that of bulk MnAs has been found to reache a maximum at $T = \sim 200$ K. The non-linear dependence of bulk MnAs Seebeck coefficient is known to originate from magnon-drag contribution [11]. However, in the case of nanowire, the magnon-drag contribution is thought to be suppressed due to increased magnon-surface scattering because the thickness of MnAs shell is only 15 nm. And the total Seebeck coefficient exhibits linear dependence on temperature because the magnon-drag contribution is much smaller than diffusion contribution.

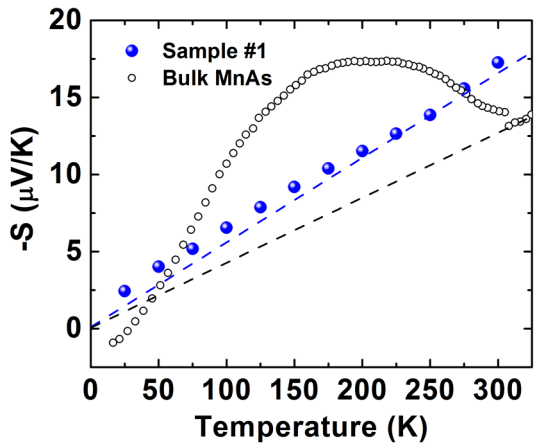

Figure 4-5. Seebeck coefficient of GaAs/MnAs core/shell nanowire and reported value of bulk MnAs [11]. The dashed line is guideline for eye.

Figure 4-6(a) shows the experimentally measured temperature dependence of electrical conductivity of MnAs shell. The electrical conductivity of sample #1 was found to exhibit a smaller slope than the data from previous measurements using four-probe measurements on nanowire [12]. This is thought to be due to contact resistance between the nanowire and the platinum pad. However, it is reasonable to assume that thermal contact is not as badly affected as the electrical contact because, although the electrical contact resistance of sample #2 is large, measured thermal conductivity of sample #1 and sample #2 is similar to each other. Furthermore, it may be concluded that the temperature difference at the junction between nanowire and platinum pad is negligibly small and electrical contact resistance would not affect measured Seebeck coefficient

Figure 4-6(b) shows the temperature dependence of *ZT* of GaAs/MnAs core shell nanowire as a function of temperature. The electrical conductivity was recalculated because we need electrical conductivity of core/shell nanowire instead of that of only shell. The plot also shows the *ZT* that was calculated using thermal conductivity and Seebeck coefficient of sample #1 and the electrical conductivity from four-probe measurement [12] which could be a more

accurate quantification of the *ZT* of the nanowire. The *ZT* decreased with decreasing temperature and the error between using the two electrical conductivities does not show a dramatic difference as would be expected from the large divergence of the electrical conductivity between the four probe and two probe measurements. This is mainly because the Seebeck coefficient approaches to zero at low temperatures and thus the power factor is dominated by the Seebeck coefficient rather than the electrical conductivity.

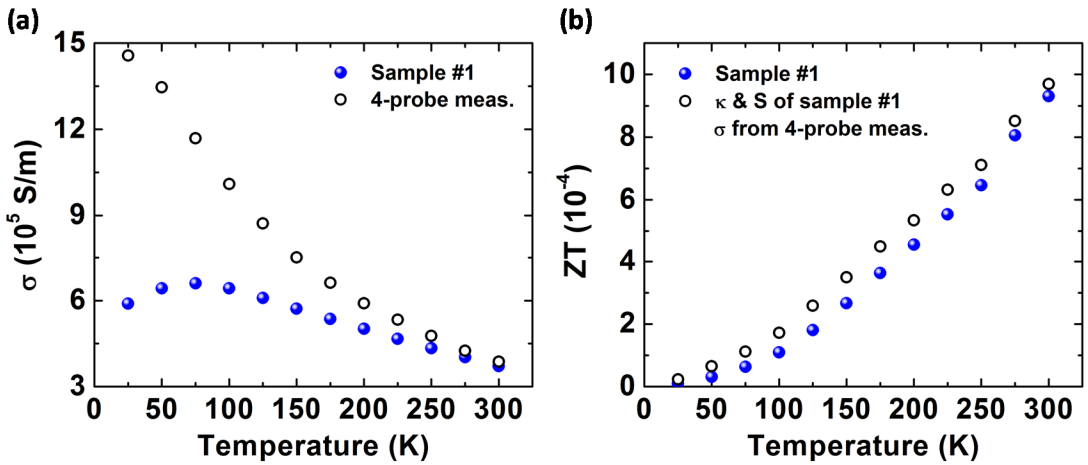

Figure 4-6. (a) Electrical conductivity of MnAs shell as a function of temperature (b) *ZT* of GaAs/MnAs core/shell nanowire as a function of temperature. The four-probe electrical conductivity were obtained from our previous report on same nanowire [12].

4.2.2 Magnetic Field Dependence

The electrical resistivity and Seebeck coefficient of GaAs/MnAs core/shell nanowires were also measured as a function of applied magnetic field. The resistance was measured using Quantum Design Physical Properties Measurement System (PPMS). The magnetic field was applied perpendicular to the wire axis. These measurements were carried out after first saturating the magnetization of the MnAs shell at 80 kOe. The device clearly showed a negative

magnetoresistance background that does not saturate, and is consistent with the previous report. The non-saturating magnetoresistance is thought to have origins in magnons and as has been discussed in earlier interpretations of their behavior in ferromagnetic thin films and nanowires[13, 14]. The damping of spin waves caused by external magnetic field suppresses the electron-magnon scattering and therefore leads to a decrease of resistance.

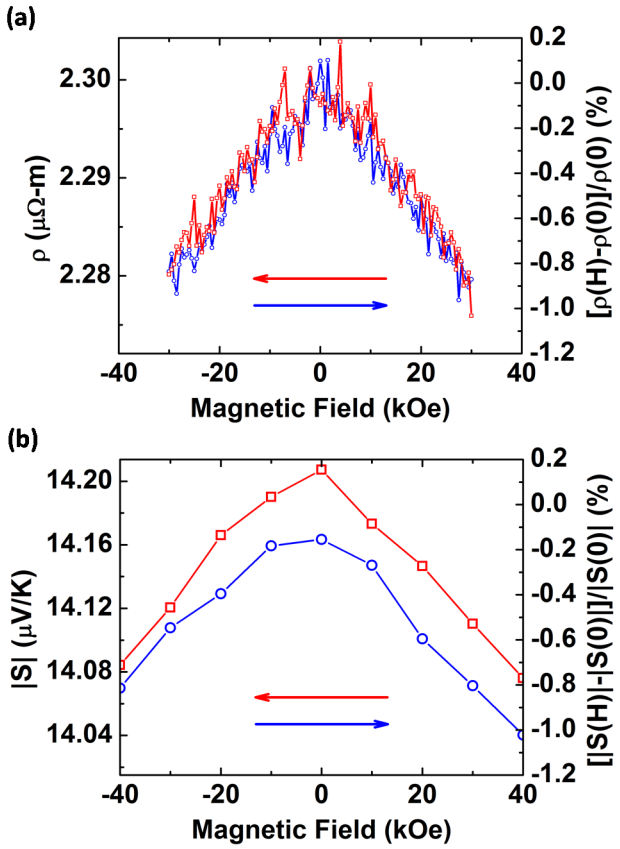

Figure 4-7. (a) Resistivity and its percentage change and (b) Seebeck coefficient and its percentage change of GaAs/MnAs core/shell nanowires as a function of magnetic field perpendicular to the wire axis at $T = 250$ K.

Unlike the previous report [12], our sample does not show hysteresis in AMR. It is thought to be caused by two factors. First, the hysteresis originates from wurtzite GaAs core [12].

Therefore, the amount of resistance change depends on the ratio of the wurzite to zinc blende GaAs core. A possibility could be that the specific nanowire that we measured has low wurzite content. Secondly, the resistivity measurements are fairly noisy due to two-probe measurement. Therefore, if the change of resistance is small, it would not be easily distinguished from the noise.

For measuring Seebeck coefficient, the same measurement set-up as explained in Chapter 2 was used except that the device was placed in the PPMS in order to apply the magnetic field. Figure 4-7(b) shows the Seebeck coefficient as a function of magnetic field. The absolute value of Seebeck coefficient exhibits maximum at zero magnetic field and decreases as the magnetic field is increased. This can also be explained by magnon contribution. A ferromagnetic material under temperature gradient is likely to have a higher density of magnons in the hotter region which diffuse to the colder region. In the process of diffusion, the magnons drag the electrons to the colder region due to electron-magnon scattering. As a result, ferromagnetic materials have one more contribution to the Seebeck coefficient in addition to diffusion and phonon-drag Seebeck coefficient. Phonon-drag contribution, at low temperature, decreases with decreasing temperature simply because of phonon freezes out. Similarly, in case of magnon-drag contribution, as the magnetic field is increased, the magnon-drag effect becomes smaller due to a damping of spin waves. As mentioned earlier, we expect magnon-drag to be depressed in the MnAs shell because increased scattering of the magnons at the surface. However, it could still have small amount of magnon-drag Seebeck coefficient and it is decreased with magnetic field. The quantitative analysis between electrical conductivity and Seebeck coefficient could not be achieved because the theory on magnon-drag contribution to Seebeck coefficient in the ferromagnetic materials has so far not been established well.

4.3 Thermoelectric Properties of Co nanowires

4.3.1 Temperature Dependence

The electronic transport in Co nanowires grown by an electrodeposition process in a nanoporous membrane template have are reported next because these nanowires provide an ideal nanomaterial to study size effects in one-dimensional magnetic systems. However, there are very few studies on magneto-Seebeck effect due to the inherent difficulties in making such measurements. Using the testbench, we investigated thermoelectric properties of Co nanowires under the influence of a magnetic field and the relation between AMR caused by s-d scattering and magneto-Seebeck coefficient. Cobalt nanowires was synthesized by direct electrodeposition into the nano-channels of an anodized aluminum oxide (AAO) membrane with 70 nm pore size [15]. High-resolution TEM analysis showed is the nanowires to be single crystalline and with a hexagonal close-packed structure with [0001] direction (*c*-axis) along the wire axis (Figure 4-8).

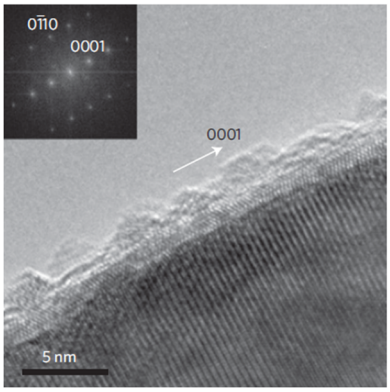

Figure 4-8. TEM image of Co nanowire. Copied from the previous report on same nanowire [16].

As a preliminary experiment for studying the effects of a magnetic field, we measured electrical conductivity, thermal conductivity, and Seebeck coefficient as a function of temperature

without applying a magnetic field. The Co nanowires were drop-cast from IPA solution on testbench and FIBID of platinum was used to make mechanical contact and improve electrical and thermal contact between nanowire and platinum pad of testbench. The EBID followed by RTA process could not be used because it was found that it does not provide good electrical contact between nanowire and platinum pad due to the native oxide on the surface of nanowire. Figure 4-9 shows SEM image of the sample.

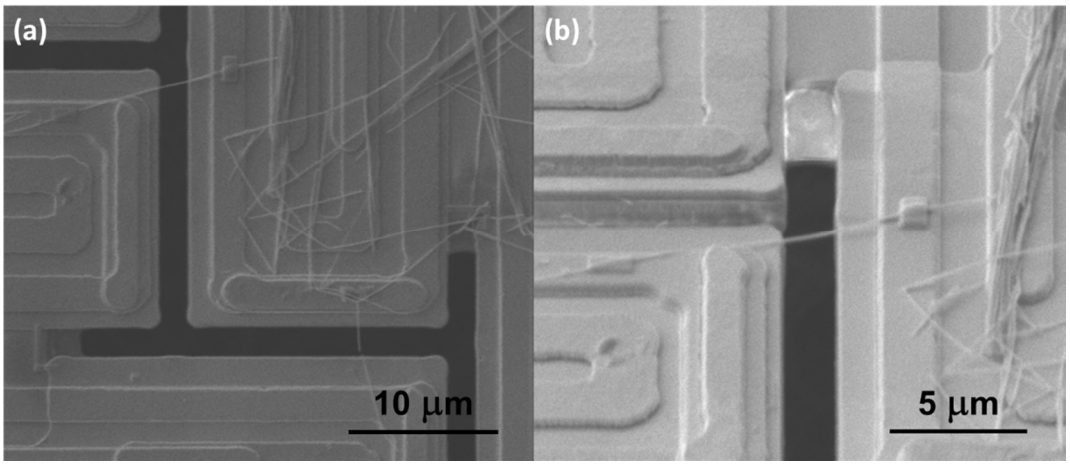

Figure 4-9. (a) Top-view and (b) oblique-view SEM images of testbench on which Co nanowire is anchored using FIBID of platinum.

Thereafter, the sample was placed in a vacuum cryostat with pressure below 5×10^{-6} Torr. The heating power, the temperature of heated and opposite platform tips and thermoelectric voltage induced in nanowire-platinum thermoelectric circuit were measured while applying the heating voltage to the heater. The resistance between two platinum pads was also measured. The measurement was performed at cryostat temperatures of 300, 200, and 100 K. Thereafter, COMSOL FEM and equivalent thermal circuit modeling were performed to extract the thermal conductivity from the measured data. The measurement and the process for obtaining the thermal

conductivity, Seebeck coefficient, and electrical conductivity from the measured data are explained in more detail in Chapter 2.

Table 4-1 shows the thermoelectric properties of nanowires measured using the testbench in this work and those of bulk Co that have been previously reported [17]. The Seebeck coefficient of Co nanowire is comparable with that of bulk Co. Considering that the diameter of 70 nm is not narrow enough to show one-dimensional density of states, it is reasonable that the Seebeck coefficient of nanowire is similar to that of bulk. The electrical conductivity is decreased by a factor of 4 and 6 at T = 300 and 200 K, respectively. And the thermal conductivity is also decreased by a similar factor. This is primarily because of the increased scattering of electrons at the surface of nanowire.

	Nanowire			Bulk [17]		
T (K)	300	200	100	300	200	100
σ (10^6 S/m)	4.2	5.0	5.8	16.7	31.1	106.5
κ (W/m-K)	26.5	21.1	14.9	98.9	119.3	164.3
S (μV/K)	−28.29	−14.77	−7.28	−30.82	−19.75	−8.43
L (10^{-8} WΩK^{-2})	2.10	2.11	2.57	1.97	1.92	1.54

Table 4-1. Thermoelectric properties of Co nanowire and bulk Co.

However, at T = 100 K, the electrical conductivity is decreased by a factor of 18 while the thermal conductivity is decreased by a factor of 11, which results in unexpected increase of Lorenz number. This is considered to arise from contact resistance between nanowire and platinum pad of the testbench which affects the two-probe electrical conductivity much more significantly as opposed to the thermal conductivity at low temperatures. Even if Ga+ ions are expected to bombard and etches the native oxide during the FIBID process, there is a possibility

of some native oxide still remaining on the nanowire surface and can act as an effective electrical barrier at low temperatures. The increasing resistance with decreasing temperature below 50 K is another indication of electrical contact resistance (Figure 4-10).

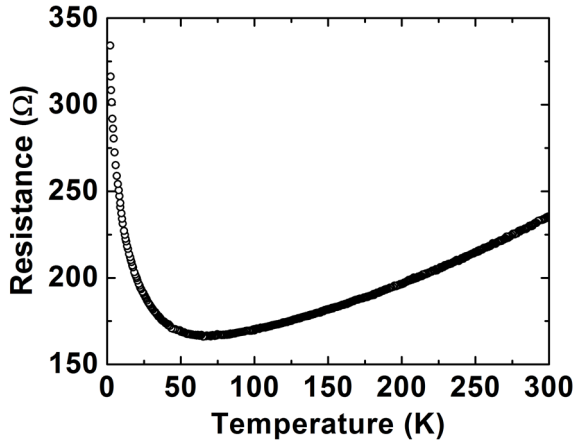

Figure 4-10. Resistance of Co nanowire as a function of temperature

4.3.2 Magnetic Field Dependence

The electrical resistivity, thermal conductivity and Seebeck coefficient were measured as a function of magnetic field. The resistance was measured using the PPMS with magnetic field perpendicular, 45 ° angled and parallel to the wire axis. The negative magnetoresistance was observed in all cases and the magnitude was largest with perpendicular magnetic field (Figure 4-11(a)). The change of resistance is known to originate from s-d scattering. The s-d scattering probability depends on the angle between magnetization and the electric current due to spin-orbit coupling. The probability is maximized when the magnetization is parallel or antiparallel to the current and it turns into maximum resistance. On the other hand, the resistance is minimized when the magnetization is perpendicular to the electric current because of minimized scattering probability. Considering the change of resistance with parallel or antiparallel magnetic field is

negligibly small compared to that with perpendicular magnetic field, the magnetization can be considered to be aligned parallel or antiparallel to the wire axis without external magnetic field. From the perspective of shape anisotropy, the nanowire favors an orientation of the magnetization along the wire axis. Moreover, our Co nanowire has *c*-axis, which is the easy axis related to crystal anisotropy, along the wire axis. Therefore, the angle between magnetization and electric current changes from 0 ° to 90 ° by perpendicular magnetic field whereas it does not change much with parallel magnetic field.

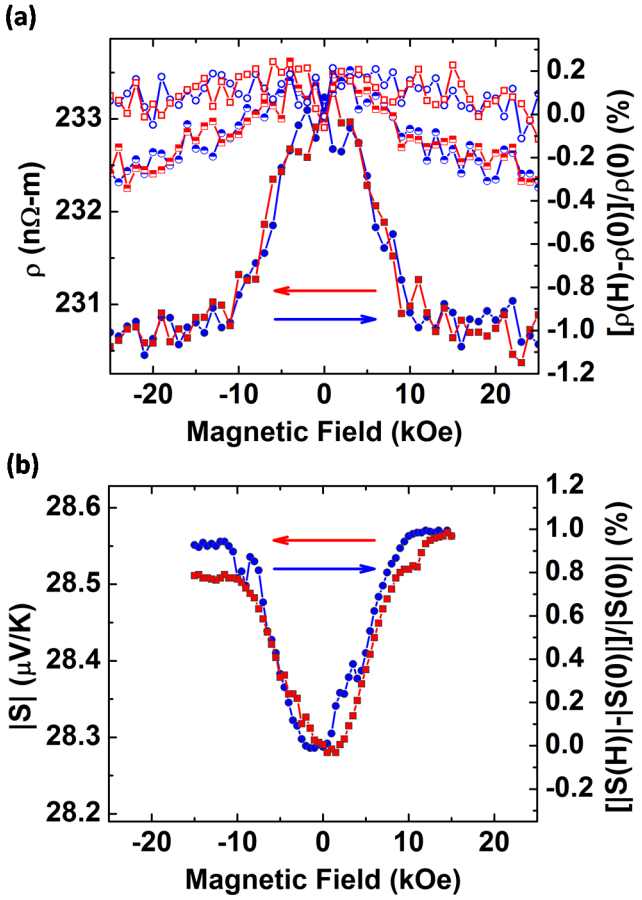

Figure 4-11. (a) Resistivity and its percentage change of Co nanowire as a function of magnetic field perpendicular (solids), 45 ° (half solids), and parallel (open) to the wire axis at $T = 300$ K. (b) Seebeck coefficient and its percentage change of Co nanowire as a function of magnetic field perpendicular to the wire axis at $T = 300$ K.

For measuring Seebeck coefficient and thermal conductivity, the same measurement set-up as explained in Chapter 2 was used except that the device was placed in the PPMS in order to apply magnetic field. The magnetic field was applied perpendicular to the wire axis. The absolute value of Seebeck coefficient increased with magnetic field (Figure 4-11(b)).

The effects of s-d scattering on magneto-Seebeck coefficient is less known compared to magnetoresistance. In recent publications [18, 19], a linear relationship between magneto-Seebeck coefficient and magnetoresistance was found in AMR dominated structure. According to Mott relation, the Seebeck coefficient and electrical resistivity is related to each other by

$$S = -\frac{\pi^2 k_B^2 T}{3e} \frac{d\ln\sigma(E)}{dE}\bigg|_{E\approx E_F} \tag{4.1}$$

$$= \frac{\pi^2 k_B^2 T}{3e} \frac{1}{\rho} \frac{d\rho(E)}{dE}\bigg|_{E\approx E_F}$$

Figure 4-12 shows the relationship between absolute value of Seebeck coefficient and inverse of resistivity that was extracted from the data with perpendicular magnetic field in Figure 4-11(a). The red circles show the data in the saturated regime. In this regime, the electron-magnon scattering is the main source for change in resistance and Seebeck coefficient. On the other hand, the blue circles represent data in the regime related to s-d scattering (non-saturated regime). Considering that the Seebeck coefficient and inverse of resistivity shows linear relationship and have similar increase rate to each other (~ 1%) in non-saturated regime, the energy derivative of resistivity is independent of the magnetic field. However, it is not so for all ferromagnetic metal. For example, in case of nickel (Ni) nanowires, the increase-rate of Seebeck coefficient (5 %) is different from that of inverse of resistivity (2 %) even if the relationship between Seebeck coefficient and inverse of resistivity looks linear [19]. This implies that the energy derivative of resistivity changes by magnetic field. The relationship still looks linear because it changes by small amount. Because the relaxation time of electrons is affected by s-d scattering probability,

the energy derivative of relaxation time would change with magnetic field. Furthermore, shift of Fermi level by magnetic field could change the energy derivative of density of states. In the case of Co nanowires, change in energy derivative of relaxation time and density of states seems to cancel each other and result in constant energy derivative of resistivity. On the other hand, in case of Ni nanowires, absolute value of the energy derivative of resistivity is increased with magnetic field.

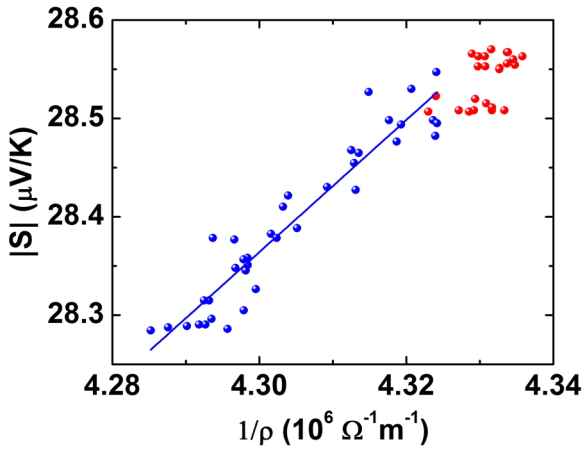

Figure 4-12. Relationship between Seebeck coefficient and inverse of resistivity of Co nanowire.

The Seebeck coefficient of Co nanowires shows a hysteresis with perpendicular magnetic field between −4 kOe and +4 kOe. Figure 4-13 shows a zoom in the region where the hysteresis occurs. Although it is less noticeable due to noise, similar hysteresis is seen in the resistivity plot as well as shown in Fig 4-11(a). The hysteresis loop originates from magnetization reversal. When the magnetic field is decreased from saturation field, the AMR and magneto-Seebeck coefficient show continuous curves corresponding to a reversible rotation of magnetization until magnetization reversal happens. At a field corresponding to magnetization reversal (± 4kOe), the curves change abruptly. The change of resistivity and Seebeck coefficient is relatively smooth in

our measurement because ramping rate of the field is not small enough. The abrupt change caused by magnetization reversal should not be observed in the magnetic field perpendicular to wire axis. However, as shown in oblique-view SEM image of Figure 4-9(b), there exists some amount of inclination between testbench and wire axis. Therefore, even if the magnetic field is applied perpendicular to the testbench, it is not perpendicular to the wire axis. We could not distinguish the hysteresis loop in the AMR with magnetic field parallel and 45 ° angled to the wire axis. It is thought to be because of the noise and the large ramping rate of magnetic field.

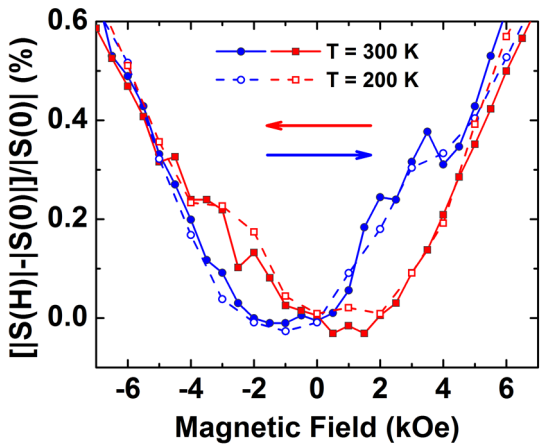

Figure 4-13. The hysteresis loop of magneto-Seebeck coefficient with a magnetic field perpendicular to the wire axis at T = 300 K and 200 K.

We also obtained the thermal conductivity as a function of magnetic field (Figure 4-14). And we compared it with the thermal conductivity calculated using measured electrical conductivity and Wiedemann-Franz law. Even though the measured thermal conductivity is noisy, the two data show similar tendency. In this measurement, we could not detect the change of Lorenz number by magnetic field which might or might not happen because the variation of Lorenz number is smaller than the noise level. However, we expect to have more clear data if we

use larger heating power because the noise originates from the small thermocouple voltage of opposite platform tip corresponding to small temperature rise (~5 mK).

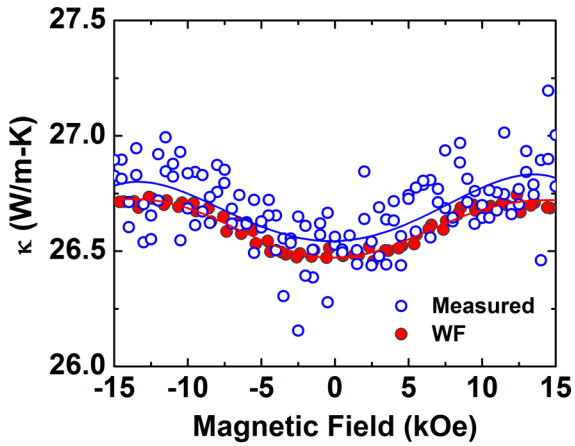

Figure 4-14. Thermal conductivity of Co nanowire measured using testbench and calculated via Wiedemann-Franz law. Solid lines are polynomial fitting curves.

4.4 Summary and Conclusion

Using the testbench, we have measured successfully the thermoelectric properties of GaAs/MnAs nanowires and Co nanowires at different temperatures and external magnetic fields. The thermal conductivity of GaAs/MnAs core/shell nanowires is 7.5 and 8.4 W/m-K at T = 300 K. It is smaller than the theoretically expected value because GaAs core has stacking faults perpendicular to the growth direction. The narrow wall thickness of MnAs shell suppresses the magnon-drag contribution to Seebeck coefficient, which results in linear temperature dependence of the Seebeck coefficient. Both resistivity and absolute value of Seebeck coefficient decrease with magnetic field perpendicular to the wire axis because the damping of spin waves caused by external magnetic field suppresses the electron-magnon scattering.

Co nanowire exhibits increasing absolute value of Seebeck coefficient and decreasing resistivity with the magnetic field perpendicular the wire axis. Based on the fact that the Seebeck coefficient and inverse of resistivity show linear relationship and have similar increase rate to each other (~ 1%) in non-saturated regime, it was found that the energy derivative of resistivity is independent of the magnetic field.

It was revealed that the magnetic field affects Seebeck coefficient of ferromagnetic materials by two factors: magnon population and s-d scattering. The magnon population is decreased with magnetic field and it leads to reduced absolute value of Seebeck coefficient due to suppressed magnon-drag contribution. And, according to Mott relation, the absolute value of Seebeck coefficient is increased with decreasing s-d scattering. This experiment confirmed that our testbench is usable for further investigation on magnetic field related thermal and thermoelectric properties, such as magneto-caloric and spin-Seebeck effect.

Reference

[1] L. Piraux, J. George, J. Despres, C. Leroy, E. Ferain, R. Legras, K. Ounadjela, and A. Fert, "Giant magnetoresistance in magnetic multilayered nanowires," *Applied Physics Letters,* vol. 65, pp. 2484-2486, 1994.

[2] J. Wegrowe, D. Kelly, A. Franck, S. Gilbert, and J.-P. Ansermet, "Magnetoresistance of ferromagnetic nanowires," *Physical review letters,* vol. 82, p. 3681, 1999.

[3] K. Uchida, S. Takahashi, K. Harii, J. Ieda, W. Koshibae, K. Ando, S. Maekawa, and E. Saitoh, "Observation of the spin Seebeck effect," *Nature,* vol. 455, pp. 778-781, 2008.

[4] E. C. Stoner, "Collective electron ferromagnetism," *Proceedings of the Royal Society of London. Series A, Mathematical and Physical Sciences,* pp. 372-414, 1938.

[5] N. Mott, "The resistance and thermoelectric properties of the transition metals," *Proceedings of the Royal Society of London. Series A-Mathematical and Physical Sciences,* vol. 156, pp. 368-382, 1936.

[6] T. Böhnert, "Magneto-thermopower and Magnetoresistance of Co-Ni Alloy and Co-Ni/Cu Multilayered Nanowires," 2014.

[7] J. De Boeck, R. Oesterholt, A. Van Esch, H. Bender, C. Bruynseraede, C. Van Hoof, and G. Borghs, "Nanometer-scale magnetic MnAs particles in GaAs grown by molecular beam epitaxy," *Applied Physics Letters,* vol. 68, pp. 2744-2746, 1996.

[8] J. De Boeck, T. Sands, J. Harbison, A. Scherer, H. Gilchrist, T. Cheeks, M. Tanaka, and V. Keramidas, "Non-volatile memory characteristics of submicrometre Hall structures fabricated in epitaxial ferromagnetic MnAl films on GaAs," *Electronics Letters,* vol. 29, pp. 421-423, 1993.

[9] N. Dellas, J. Liang, B. Cooley, N. Samarth, and S. Mohney, "Electron microscopy of GaAs/MnAs core/shell nanowires," *Applied Physics Letters,* vol. 97, pp. 072505-072505-3, 2010.

[10] P. N. Martin, Z. Aksamija, E. Pop, and U. Ravaioli, "Reduced thermal conductivity in nanoengineered rough ge and gaas nanowires," *Nano letters,* vol. 10, pp. 1120-1124, 2010.

[11] U. Neitzel and K. Barner, "The thermoelectric power of MnAs1-xPx compounds," *Journal of Physics C: Solid State Physics,* vol. 11, p. 4975, 1978.

[12] J. Liang, J. Wang, A. Paul, B. Cooley, D. Rench, N. Dellas, S. Mohney, R. Engel-Herbert, and N. Samarth, "Measurement and simulation of anisotropic magnetoresistance in single GaAs/MnAs core/shell nanowires," *Applied Physics Letters,* vol. 100, pp. 182402-182402-5, 2012.

[13] B. Raquet, M. Viret, E. Sondergard, O. Cespedes, and R. Mamy, "Electron-magnon scattering and magnetic resistivity in 3 d ferromagnets," *Physical Review B,* vol. 66, p. 024433, 2002.

[14] V. Nguyen, C. Naylor, L. Vila, A. Marty, P. Laczkowski, C. Beigne, L. Notin, Z. Ishaque, and J. Attane, "Magnon magnetoresistance of NiFe nanowires: Size dependence and domain wall detection," *Applied Physics Letters,* vol. 99, p. 262504, 2011.

[15] M. Tian, S. Xu, J. Wang, N. Kumar, E. Wertz, Q. Li, P. M. Campbell, M. H. Chan, and T. E. Mallouk, "Penetrating the oxide barrier in situ and separating freestanding porous anodic alumina films in one step," *Nano letters,* vol. 5, pp. 697-703, 2005.

[16] J. Wang, M. Singh, M. Tian, N. Kumar, B. Liu, C. Shi, J. Jain, N. Samarth, T. Mallouk, and M. Chan, "Interplay between superconductivity and ferromagnetism in crystalline nanowires," *Nature Physics,* vol. 6, pp. 389-394, 2010.

[17] M. Laubitz and T. Matsumura, "Transport properties of the ferromagnetic metals. I. Cobalt," *Canadian Journal of Physics,* vol. 51, pp. 1247-1256, 1973.

[18] A. Avery, M. Pufall, and B. Zink, "Determining the planar Nernst effect from magnetic-field-dependent thermopower and resistance in nickel and permalloy thin films," *Physical Review B,* vol. 86, p. 184408, 2012.

[19] T. Böhnert, V. Vega, A.-K. Michel, V. M. Prida, and K. Nielsch, "Magneto-thermopower and magnetoresistance of single Co-Ni alloy nanowires," *Applied Physics Letters,* vol. 103, p. 092407, 2013.

Chapter 5 Concluding Remarks

5.1 Conclusion

In this dissertation, the development of a microfabricated testbench for measuring thermal and thermoelectric properties of low-dimensional materials has been presented and thermoelectric efficiency of Bi_2Te_3 nanotubes and the effect of magnetic field on thermoelectric properties of ferromagnetic nanowires have been studied using testbench.

The testbench has been designed to measure thermal conductivity and Seebeck coefficient of low-dimensional materials in addition to electrical conductivity. It consists of 52 closely placed thermally isolated platform tips which are located in central area for enhancing a probability of landing a single test-material on two interlocking platform tips. Each platform has the integrated heater and thermocouple for heating and temperature sensing. The platinum pad is on top of platform in order to provide electrical connection to the test-material. It has been successfully fabricated and characterized electrically and thermally. And the polysilicon-gold thermocouple has been calibrated at temperatures ranging from 300 K to 15 K.

The thermoelectric efficiency of individual nanocrystalline Bi_2Te_3 nanotubes synthesized by solution phase method has been measured using the testbench and 3ω method and it has been observed that the nanotube has larger *ZT* than bulk Bi_2Te_3 near room temperature due to its nanocystalline nature and low-dimensionality. The Seebeck coefficient is enhanced by low-energy electrons filtered at crystalline domain boundary and the electron-surface scattering suppresses lattice thermal conductivity. This improvement in *ZT* originates from nanocrystalline nature and low-dimensionality of nanotube. This work demonstrated the possibility of achieving

enhancement in thermoelectric efficiency by combining nanocrystalline and low-dimensional systems.

Using the testbench, we have measured successfully the thermoelectric properties of GaAs/MnAs nanowires and Co nanowires at different temperatures and external magnetic fields. It has been revealed that the effect of magnetic field on Seebeck coefficient of ferromagnetic materials is determined by magnon population and s-d scattering. The decreased magnon population suppresses magnon-drag contribution and reduces the absolute value of Seebeck coefficient. And the decreased s-d scattering enhances the absolute value of Seebeck coefficient, which is explained by Mott relation. This experiment confirmed that our testbench is applicable for further investigation on magnetic field related thermal and thermoelectric properties, such as magneto-caloric and spin-Seebeck effect.

5.2 Future Work

5.2.1 Modification of Testbench

We have shown that the microfabricated testbench is successfully used to measure electrical conductivity, thermal conductivity, and Seebeck coefficient. However, the testbench still has two imperfections. 1) As shown in the measurement with GaAs/MnAs core/shell nanowires and Co nanowires, the electrical conductivity measured using testbench includes the contact resistance between nanowire and platinum pad. Although the contact resistance is negligibly small around room temperature, it could increase to the value that is larger than or comparable to the resistance of nanowire at low temperatures. 2) As explained in Chapter 2, the amount of heat transferred through substrate is equivalent to that through test-material having thermal conductance of 9.7×10^{-9} W/K. Therefore, if the thermal conductance of test-material is

comparable to or smaller than this value, the parasitic heat flow would reduce the accuracy of the measurement of the thermal conductivity in test-material. Because of this parasitic heat, in case of Bi_2Te_3 nanotubes, we had to measure the thermal conductivity with 3ω device and we could not measure all three properties in one specific nanotube. We can overcome these problems by redesigning the platinum pad as shown in Figure 5-1. It then results in four-probe configuration. The two platforms connected through test-material are used as current-feeding probes and the other two platforms are voltage-sensing probes. Therefore, we can measure four-probe resistance and also use 3ω method to measure thermal conductivity

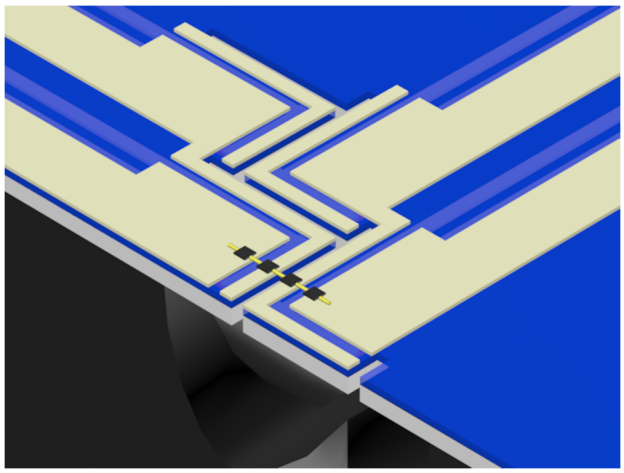

Figure 5-1. Proposed next generation of testbench.

5.2.2 Spin Caloritronics at Nanoscale

The interplay of spin, charge, and thermal transport in metals and semiconductors raises many unsolved fundamental puzzles, such as the role of magnon-drag in the thermoelectric properties of ferromagnetic metals [1] and the fundamental origins of the recently discovered spin-Seebeck effect [2-5]. Experimental work in this rapidly developing field of spin caloritronics [6] thus far has largely focused on thin films and bulk crystals. Using the testbench, spin

caloritronics can be explored in low-dimensional geometry, suspended nanowires and nanotubes, thus removing the influence of a substrate. Low-dimensional ferromagnets also simplify the domain structure, thus removing the complexities created by multiple domain walls in more macroscale samples.

5.2.3 Thermoelectric Measurements: A Tool to Probe Molecular Structures of Heterojunctions

The nature of nanowires promises improvements in the *ZT* values via multiple methods. While, most recent 1-D enhancement studies have focused on improving *ZT* by decreasing thermal conductivity through size reduction [7] or surface roughening [8], further opportunities to improve the *ZT* values in such systems have been recently observed by our group [9]. In particular, Seebeck coefficient measurements on free-standing, straight and "junctioned" gold nanowires using a micromachined thermoelectric testbench were made. Measurements on straight 70 nm diameter gold nanowires showed a Seebeck coefficient similar to that of bulk gold; however for "junctioned" gold nanowires we observed a hitherto unreported peak in the Seebeck coefficient near room temperature [9]. The observed enhancement was explained by approximating the "junctioned" nanowires as tunnel junctions in combination with Coulombic effect of the electrons crossing the junction. The electron transfer across the barrier can be expected to be stochastic in nature. In the presence of a temperature gradient across the junction, the time averaged fluctuation of the electrons across the junction is now offset by the tunnel junction thermoelectric effect. Most importantly, a fivefold enhancement in the Seebeck coefficient of "junctioned" nanowires was observed for the gold nanowires measured over several samples. In tunnel junctions a thermoelectric voltage arises due to the higher average energy of the electrons on the hot side in comparison to the cold side resulting in preferential tunneling of

electrons towards the cold side of the junction [10-12]. The Seebeck coefficient in ideal tunnel junctions is found to be insensitive to the barrier width and to image charges [12]. The calculated tunneling Seebeck coefficient is much larger than the value of diffusive Seebeck coefficient of bulk gold in the same temperature region and therefore dominates the observed behavior of the device.

However, in spite of this preliminary work, our understanding of the tunnel junction effect is not complete at this time. For example, we do not completely understand (i) how the observed enhancement depends on the junction interface, (ii) what role can molecules trapped in the tunnel junction region play in the eventual enhancement of the tunnel junction effect, and (iii) how the tunnel junction effect can be exploited further for the optimization of nanoscale thermoelectric materials.

In the case where the vacuum tunnel junction described above has been substituted with a tunnel junction with a specific molecule inserted at the interface, the physics of the device become even more interesting. It has been theoretically predicted that Seebeck coefficient measurements can uniquely distinguish whether transport is dominated by the highest occupied molecular orbital (HOMO) (if measured value is positive) or lowest unoccupied molecular orbital (LUMO) (if it is negative) level in the molecule in a heterojunction [13, 14]. For a molecule with Fermi energy of E_i connected to metal electrodes with Fermi energy of E_F, the transmission coefficient $\tau(E) \sim 1$ when the E_F aligns with either the HOMO or the LUMO levels and decreases rapidly in between. Thus, Seebeck coefficient measurements offer an alternative transport measurement that can characterize the dominant transport orbital and is independent of the number of molecules in the junction. This method can thus be used to explore the effect of chemical structure on the electronic structure and charge transport. Baheti et al. have experimentally interrogated 1,4-benzenedithiol (BDT) molecule which has been modified by the addition of electron-withdrawing or -donating groups such as fluorine, chlorine junctions, using a

modified scanning tunneling microscope break junction technique [15]. While high Seebeck coefficient values are obtained for aligned Fermi energies, to achieve high *ZT* values, it has been theoretically predicted that the molecular state through which charge is transported must be weakly coupled to the leads, and the energy level of the state must be of order k_BT away from the Fermi energy of the leads [16]. These requirements may be better satisfied by the [Co(tpy-$(CH_2)_5$-SH$)_2$] molecules studied for electronic transport by Park et al [17]. [Co(tpy-$(CH_2)_n$-SH$)_2$] are coordination complexes in which one Co ion is bonded within an approximately octahedral environment to two terpyridinyl linker molecules with thiol end groups, which allows for self-assembly onto gold electrode surfaces. The electronic transport in these systems is through a cobalt atom that sits at the center of the molecule; the alkyl chains separate the cobalt from the gold leads, creating a state localized away from the leads. It would be of great interest to confirm that the Wiedemann-Franz law is indeed violated in these molecules - which has not been experimentally done until now.

Reference

[1] M. V. Costache, G. Bridoux, I. Neumann, and S. O. Valenzuela, "Magnon-drag thermopile," *Nature Materials,* vol. 11, pp. 199-202, Mar 2012.

[2] K. Uchida, S. Takahashi, K. Harii, J. Ieda, W. Koshibae, K. Ando, S. Maekawa, and E. Saitoh, "Observation of the spin Seebeck effect," *Nature,* vol. 455, pp. 778-781, Oct 2008.

[3] C. M. Jaworski, J. Yang, S. Mack, D. D. Awschalom, J. P. Heremans, and R. C. Myers, "Observation of the spin-Seebeck effect in a ferromagnetic semiconductor," *Nature Materials,* vol. 9, pp. 898-903, Nov 2010.

[4] K. Uchida, J. Xiao, H. Adachi, J. Ohe, S. Takahashi, J. Ieda, T. Ota, Y. Kajiwara, H. Umezawa, H. Kawai, G. E. W. Bauer, S. Maekawa, and E. Saitoh, "Spin Seebeck insulator," *Nature Materials,* vol. 9, pp. 894-897, Nov 2010.

[5] C. M. Jaworski, R. C. Myers, E. Johnston-Halperin, and J. P. Heremans, "Giant spin Seebeck effect in a non-magnetic material," *Nature,* vol. 487, pp. 210-213, Jul 2012.

[6] G. E. W. Bauer, E. Saitoh, and B. J. van Wees, "Spin caloritronics," *Nature Materials,* vol. 11, pp. 391-399, May 2012.

[7] A. I. Boukai, Y. Bunimovich, J. Tahir-Kheli, J.-K. Yu, W. A. Goddard Iii, and J. R. Heath, "Silicon nanowires as efficient thermoelectric materials," *Nature,* vol. 451, p. 168, 2008.

[8] A. I. Hochbaum, R. Chen, R. D. Delgado, W. Liang, E. C. Garnett, M. Najarian, A. Majumdar, and P. Yang, "Enhanced thermoelectric performance of rough silicon nanowires," *Nature,* vol. 451, p. 163, 2008.

[9] N. B. Duarte, G. D. Mahan, and S. Tadigadapa, "Thermopower Enhancement in Nanowires via Junction Effects," *Nano Letters,* vol. 9, pp. 617-622, 2009.

[10] A. D. Smith, M. Tinkham, and W. J. Skocpol, "New thermoelectric effect in tunnel junctions," *Physical Review B,* vol. 22, p. 4346, 1980.

[11] C. R. Leavens and G. C. Aers, "Vacuum tunnelling thermopower: Normal metal electrodes," *Solid State Communications,* vol. 61, p. 289, 1987.

[12] J. Marschall and A. Majumdar, "Charge and energy transport by tunneling thermoelectric effect," *Journal of Applied Physics,* vol. 74, p. 4000, 1993.

[13] M. Paulsson and S. Datta, "Thermoelectric effect in molecular electronics," *Physical Review B,* vol. 67, p. 241403, 2003.

[14] S.-H. Ke, W. Yang, S. Curtarolo, and H. U. Baranger, "Thermopower of Molecular Junctions: An ab Initio Study," *Nano Letters,* vol. 9, pp. 1011-1014, 2009.

[15] K. Baheti, J. A. Malen, P. Doak, P. Reddy, S.-Y. Jang, T. D. Tilley, A. Majumdar, and R. A. Segalman, "Probing the Chemistry of Molecular Heterojunctions Using Thermoelectricity," *Nano Letters,* vol. 8, pp. 715-719, 2008.

[16] P. Murphy, S. Mukerjee, and J. Moore, "Optimal thermoelectric figure of merit of a molecular junction," *Physical Review B (Condensed Matter and Materials Physics),* vol. 78, pp. 161406-4, 2008.

[17] J. Park, A. N. Pasupathy, J. I. Goldsmith, C. Chang, Y. Yaish, J. R. Petta, M. Rinkoski, J. P. Sethna, H. D. Abruna, P. L. McEuen, and D. C. Ralph, "Coulomb blockade and the Kondo effect in single-atom transistors," *Nature,* vol. 417, pp. 722-725, 2002.

VITA

DukSoo Kim

DukSoo Kim was born in Seoul, South Korea on April 15, 1980. He received B.S. and M.S. in Electrical Engineering from Korea University, Seoul, South Korea in 2007 and 2009, respectively. Thereafter, he worked as an engineer at Samsung Electronics. In August 2010 he entered the Ph.D. program in Electrical Engineering at The Pennsylvania State University and joined the MEMS and nanoscale devices group headed by Dr. Srinivas Tadigadapa. His research interests are in microfabrication and electronic and thermoelectric transports in the nanoscale systems.